



Cite this: *Chem. Soc. Rev.*, 2016, 45, 412

# Simulations of inorganic–bioorganic interfaces to discover new materials: insights, comparisons to experiment, challenges, and opportunities

Hendrik Heinz<sup>\*ab</sup> and Hadi Ramezani-Dakheel<sup>bc</sup>

Natural and man-made materials often rely on functional interfaces between inorganic and organic compounds. Examples include skeletal tissues and biominerals, drug delivery systems, catalysts, sensors, separation media, energy conversion devices, and polymer nanocomposites. Current laboratory techniques are limited to monitor and manipulate assembly on the 1 to 100 nm scale, time-consuming, and costly. Computational methods have become increasingly reliable to understand materials assembly and performance. This review explores the merit of simulations in comparison to experiment at the 1 to 100 nm scale, including connections to smaller length scales of quantum mechanics and larger length scales of coarse-grain models. First, current simulation methods, advances in the understanding of chemical bonding, in the development of force fields, and in the development of chemically realistic models are described. Then, the recognition mechanisms of biomolecules on nanostructured metals, semimetals, oxides, phosphates, carbonates, sulfides, and other inorganic materials are explained, including extensive comparisons between modeling and laboratory measurements. Depending on the substrate, the role of soft epitaxial binding mechanisms, ion pairing, hydrogen bonds, hydrophobic interactions, and conformation effects is described. Applications of the knowledge from simulation to predict binding of ligands and drug molecules to the inorganic surfaces, crystal growth and shape development, catalyst performance, as well as electrical properties at interfaces are examined. The quality of estimates from molecular dynamics and Monte Carlo simulations is validated in comparison to measurements and design rules described where available. The review further describes applications of simulation methods to polymer composite materials, surface modification of nanofillers, and interfacial interactions in building materials. The complexity of functional multiphase materials creates opportunities to further develop accurate force fields, including reactive force fields, and chemically realistic surface models, to enable materials discovery at a million times lower computational cost compared to quantum mechanical methods. The impact of modeling and simulation could further be increased by the advancement of a uniform simulation platform for organic and inorganic compounds across the periodic table and new simulation methods to evaluate system performance *in silico*.

Received 2nd December 2015

DOI: 10.1039/c5cs00890e

[www.rsc.org/chemsocrev](http://www.rsc.org/chemsocrev)

## 1. Introduction

Materials containing functional biological, organic, and inorganic compounds are ubiquitous in nature and manmade materials. Examples of naturally occurring, hierarchically ordered inorganic–organic composite materials are the skeletons of diatoms, seashells, bone, and teeth. Opportunities in abiotic–biotic assembly have inspired drug delivery systems, catalysts, devices

for energy conversion, polymer nanocomposites for automotive and aerospace applications, consumer electronics, building materials, and commodities.<sup>1–9</sup> A common challenge consists in controlling the architecture from the nanometer scale to the macroscopic scale, *i.e.*, from nanometers to millimeters and beyond. Current computational methods to examine structural, chemical, and physical properties typically perform well for subsections of these length scales and can be combined or correlated with each other in multi-scale approaches (Fig. 1).<sup>10–15</sup> Access to a certain length scale in computational methods is accompanied with characteristic time scales. Common simulation approaches include quantum mechanical calculations, classical molecular dynamics and Monte Carlo methods, field-based and finite element simulations. The benefit of modeling and

<sup>a</sup> Department of Chemical and Biological Engineering, University of Colorado–Boulder, Boulder, CO 80309, USA. E-mail: [hendrik.heinz@colorado.edu](mailto:hendrik.heinz@colorado.edu)

<sup>b</sup> Department of Polymer Engineering, University of Akron, Akron, Ohio 44325, USA

<sup>c</sup> Institute for Molecular Engineering, University of Chicago, Chicago, Illinois 60637, USA

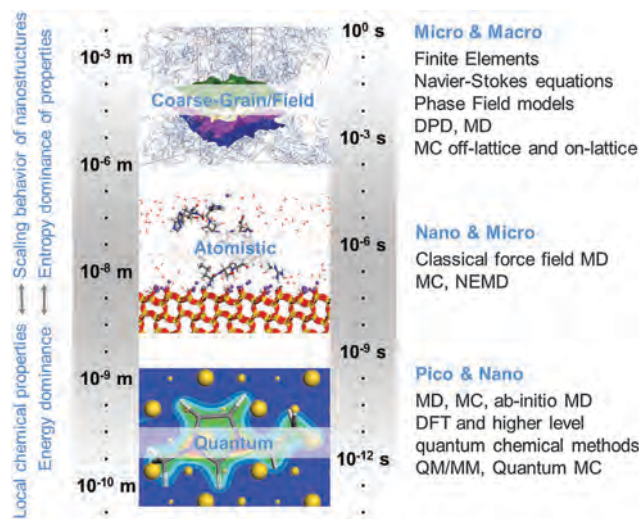


Fig. 1 Different time and length scales of common simulation methods. Reproduced with permission from ref. 11.

simulations is greatest when applied to interesting problems where experiments provide incomplete information, *i.e.*, in case that experiment is blind, costly, dangerous, or impossible.<sup>16</sup> These scenarios apply, for example, for difficulties in imaging at the 1 to 100 nm scale, in drug development, testing of explosives' chemistry, or in astrophysics. In chemical science of hard and soft matter, therefore, many simulations are concerned with properties on very small length scales of nanometers and on very short time scales of femtoseconds to microseconds to enable visualizations and estimates of thermodynamic and kinetic properties.

This review covers simulation approaches at the 1 to 100 nm scale, current understanding of selective recognition of biomolecules on metal and oxide nanostructures, as well as applications to surface modification, crystal growth, catalysis, polymer composites,

and building materials. In Section 2 it is described how simulation approaches are exploited to understand electronic structure and to implement of chemical knowledge into force fields to achieve predictive simulations at a scale far beyond molecules. Sections 3–5 review fundamental understanding of molecular recognition, growth, and performance of inorganic nanostructures using classical atomistic simulations, *ab initio* simulations, and laboratory measurements. First, molecular recognition of biomolecules on metallic and semimetallic substrates is described along with applications in catalysts and sensors (Section 3). Then, interfaces of biomolecules and organic ligands with oxide, phosphate, carbonate, sulfide, and other inorganic substrates are discussed, including applications to the formation of biominerals, drug delivery, and understanding solar devices (Section 4). The critical role of surface chemistry, pH, and ionic strength along with realistic implementation in molecular models is emphasized. In Section 5, the features of inorganic–organic interfaces in polymer composites and building materials will be discussed, including the role of surface modification, thermodynamic and kinetic processes. Challenges and opportunities are summarized in Section 6, and conclusions described at the end (Section 7). The focus is on computational insights in comparison to experimental measurements to illustrate common predictions, feasible accuracy, and applications in materials design.

## 2. Simulation approaches and performance

This section provides an overview of simulation methods, force fields, chemical concepts, and performance assessments for systems at the 1 to 100 nm scale with a focus on classical simulation methods far beyond the reach of quantum mechanical methods. Recent force field developments for inorganic compounds and inorganic–organic interfaces enable access to many inorganic



**Hendrik Heinz**

*Hendrik Heinz is an associate professor at the University of Colorado-Boulder. He received his PhD degree from ETH Zurich in 2003 and carried out postdoctoral work at the Air Force Research Laboratory in Dayton, Ohio. His research interests include the simulation of biological and nanostructured materials, metals, minerals, polymers, inorganic–organic interfaces, and multiscale computational methods. Recent honors include the Sandmeyer award of the Swiss Chemical Society, the Max Hey Medal of the Mineralogical Society, an NSF Career Award, as well as guest professorships at ETH Zurich and at the National Institute for Materials Science (NIMS) in Tsukuba, Japan.*



**Hadi Ramezani-Dakheel**

*Hadi Ramezani-Dakheel is currently a postdoctoral scholar at the University of Chicago. He obtained his PhD degree in 2015 from the University of Akron in the Heinz laboratory, and an MS degree from Amirkabir University. His research interests include the development and application of accurate force fields and advanced computational methods to solve fundamental problems in materials science. Current projects aim at understanding design principles of metal nanocrystals, catalysts, early-stage mineralization, liquid crystals, metallic and organic glasses. He was awarded the Eastman Chemical Company Fellowship, the Frank N. Kelley Graduate Student Award, and an UASIS Outstanding Graduate Student Research Award.*

materials and trillions of potential inorganic–organic interfaces that were previously difficult to study using molecular simulations.<sup>11,17–23</sup> It is discussed how the accuracy of computational predictions has improved by orders of magnitude over the last decade.

## 2.1. Overview of simulation methods

Quantum mechanical calculations enable the analysis of the geometry of molecules, conformers, and clusters of molecules with a focus on electron density, orbital geometry, chemical reactions, and transition states (Fig. 1).<sup>24–26</sup> Many-electron systems require simplifications of the Schrodinger equation to become computationally feasible.<sup>27–31</sup> Common coupled cluster and density functional theory (DFT) methods rely on approximate basis functions and basis sets. Density functionals reduce the compute expense from  $O(N^7)$  with full configuration interaction (CI) to  $O(N^3)$  to enable the simulation of systems up to thousands of atoms ( $N$ ) for picoseconds. The completion of one picosecond *ab initio* molecular dynamics of a peptide in 500 molecules of water using the GGA-PBE functional currently requires approximately 128 processor cores for one week.<sup>32</sup> Crystal structures of inorganic solids are typically predicted in very good agreement with experiment (<1% deviation) while surface energies often deviate ~30% from experimental measurements.<sup>27,29,33</sup> Cohesive energies of small organic molecules and electronic excitation energies show similar deviations from experiment.<sup>34,35</sup> The Hamiltonian in DFT performs generally well for isolated single molecules and reproduces structures but not energies for non-covalent assemblies of several atoms and molecules. Quantum mechanics is a key tool to investigate chemical reactivity and electronic properties at the scale of chemical bonds, including electron densities, energy levels, conductive properties, and magnetism.

Access to larger systems is possible on the basis of a classical Hamiltonian using molecular dynamics (MD) and Monte Carlo (MC) simulations (Fig. 1). The energy expression of classical force fields is computationally less costly and computing time scales as  $O(N \ln N)$  or  $O(N^2)$  with the number of atoms  $N$ , depending on the algorithm of the summation of pairwise interactions. Classical atomistic simulations tend to be a million times faster in comparison to DFT calculations for the same system size. Folding and self-organization of chain molecules in solution and at surfaces in all-atom resolution can be studied at realistic concentrations, pH, and ionic strength.<sup>36–41</sup> Longest recorded simulation times in all-atom resolution are in the range of milliseconds.<sup>42</sup> For example, the completion of 100 nanoseconds classical MD of a protein in 1000 molecules of water with high accuracy of Coulomb interactions currently requires approximately four processor cores for one week. Access to significant time scales and parallel simulations enable the exploration of complex configuration spaces at length scales of 1 to 100 nm. Interfacial assembly, thermal transitions, diffusion, optical switching, and time-dependent mechanical properties can be investigated.<sup>18,42–49</sup> A major limitation is the difficulty to simulate the dissociation and formation of chemical bonds during chemical reactions unless reactive potentials<sup>50–52</sup> or modifications of chemical bonding are applied.<sup>53</sup>

Simulations of the structure at length scales of 10 nm to 100  $\mu\text{m}$  and the dynamics at time scales of nanoseconds to seconds become accessible using molecular dynamics and Monte Carlo simulations with coarse-grain models (Fig. 1). Coarse-grain models involve fewer degrees of freedom compared to atomistic models as every bead represents multiple, tens, or hundreds of atoms according to the desired level of coarse-graining.<sup>54–56</sup> The energy expression is simplified and, for example, may only contain terms for bond stretching and van-der-Waals interactions.<sup>57,58</sup> The similarity of the energy expression to all-atoms models enables simulations in dual atomistic/coarse grain resolution.<sup>59</sup> Access to longer length and times scales allows the study of macromolecular assembly, polymer blends and composites, creep behavior, and viscosity of polymer solutions.<sup>60–65</sup> Dissipative Particle Dynamics with soft, interpenetrating particles<sup>66</sup> as well as field-based continuum approaches<sup>67</sup> similarly reach length scales of micrometers and beyond.

## 2.2. Atomistic force fields for the simulation of inorganic–organic interfaces

All-atom simulations at the 1 to 100 nm scale usually rely on an energy expression (classical Hamiltonian) that needs to reproduce structures and energetics of the chosen systems in agreement with experiment or high-level *ab initio* data. Classical energy expressions are available for different types of compounds, however, existing mathematical terms that constitute the expressions can be quite different and lead to low compatibility (Fig. 2). Simulations of interfaces between inorganic, organic, and biomolecular compounds had hence been a massive challenge. To enable the simulation of such inorganic–organic systems, and eventually of all compounds

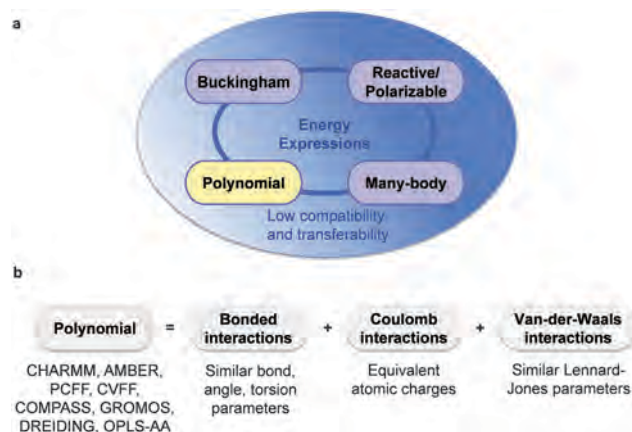


Fig. 2 Available energy expressions for atomistic simulations and the advantages of polynomial potentials. (a) Many energy expressions are mathematically incompatible with each other and serve specialized materials classes, for example, many body potentials for metals and alloys, Buckingham potentials for minerals, reactive potentials for hydrocarbons and covalent solids (Si, C). Polynomial potentials can be used for a general force field since the functional form is similar to a quantum mechanical Hamiltonian and can be applied to all types of materials, including metals, minerals, and soft matter. (b) Polynomial energy expressions consist of additive terms for bonded, Coulomb, and van-der-Waals interactions. Compatibility barriers among different polynomial force fields are comparatively low.

across the periodic table using a single common platform, it is thus beneficial to choose one and the same energy expression.<sup>17,18,23,68</sup>

Polynomial energy expressions have been emerging as a common denominator. Polynomial energy expressions use pairwise interactions for all key intermolecular forces (except angle and torsion constraints) with a sound quantum-mechanical justification. Reactive, bond order, and EAM potentials include many-body terms of a more empirical nature and have no thorough quantum-mechanical foundation. The performance of polynomial force fields is good for metals, minerals, polymers<sup>18,68,69</sup> and virtual sites for electrons can be added as needed.<sup>70,71</sup> Parameters for proteins and organic compounds such as in CVFF, CHARMM, OPLS-AA, AMBER, CFF, and COMPASS are well established<sup>72–77</sup> and accurate parameters for inorganic compounds have been introduced in the INTERFACE force field.<sup>11,68,69,78–80</sup> These additions allow to study trillions of new bioorganic interfaces with metals and minerals. It was shown that combination rules for nonbond parameters between the inorganic and organic compounds perform well so that no additional parameters are necessary to simulate interfacial interactions.<sup>43,68,78,80–86</sup> The use of such combination rules is possible when bond polarity and dispersion forces for inorganic compounds are treated just the same as for solvents, organic multipolar molecules, and biomacromolecules, which may contain similar ionic groups. Examples of such representations of inorganic–organic interactions in simulations include the hydration energy of metal and silica surfaces,<sup>58,78,87</sup> the binding energies of peptides to Au, Pt, and silica surfaces in water,<sup>37,43,82</sup> the assembly of surfactants and cleavage energies of organically modified clay minerals.<sup>84,88</sup> The agreement of simulations with experiment is better than 5%, given initial reproduction of bond polarity (atomic charges) and of the surface or cleavage energy of the inorganic solid in comparison to experimental reference data.<sup>11</sup> Combination rules can also be overwritten if necessary, although this is not needed in most cases.

The approach towards a uniform energy expression for inorganic and organic compounds is motivated by a series of computational studies by Sauer, Teppen, Kalinichev, Heinz, Cygan, and Parker, among others.<sup>17,18,20,23,68,89–91</sup> Heinz also recognized that not only the validation of structures but also of energies of solids was critical,<sup>68</sup> after Parker and de With tested the surface energy of spinel using Buckingham potentials and found significant deviations.<sup>92</sup> Since then, the first contributions to the INTERFACE force field were developed and subsequently expanded for further compounds, including clay minerals, silicates, metals, aluminates, phosphates, and sulfates (Fig. 3). The INTERFACE approach demands that the energy expression, *i.e.*, the classical “Hamiltonian”, reproduces the structure of a given compound as well as its energy in agreement with experiment. From there, all other properties such as interfacial, thermal, and mechanical (*i.e.* first and second derivatives of energy) follow in best possible agreement. This goal is achieved for a given compound by understanding the different atom types, chemical bonding and its quantitative representation *via* atomic charges as defined by Heinz,<sup>19</sup> validation of the structure, as well as of at least one surface property (surface tension,

cleavage energy, hydration energy, or contact angle).<sup>11</sup> It is also helpful to associate all parameters with a chemical rationale, allowing comparisons among chemically similar compounds across the periodic table. Details of the INTERFACE procedure to parameterize new compounds are described in ref. 11.

Alternative methods to parameterize interfacial interactions include the use of *ab initio* data to parameterize interactions between small molecules and then apply these parameters to extended surfaces such as silicates or aluminates.<sup>23,89</sup> A large scatter in possible atomic charges and a missing rationale for Lennard-Jones parameters, however, made the assignment of consistent nonbond parameters very difficult. These difficulties are similar to the challenge in parameterization of exchange and correlation terms in density functionals themselves.<sup>27</sup> As a result, typically fixed atoms were required to avoid structural collapse of silicates and aluminates during the simulation and errors in computed surface properties relative to experiment reached up to 500%.<sup>78,93,94</sup> This approach, without chemical rationale and comparison to experimental data as in the INTERFACE force field, does not lead to accurate force fields or quantitative insight into inorganic–organic interfaces. Recent approaches towards force fields for inorganic compounds along with similar *ab initio* concepts rely on DFT calculations for the adsorption of small molecules in the gas phase to a given solid surface, comparison with experimental adsorption data, and fitting of dedicated parameters for pairwise nonbonded interaction across the inorganic–organic interface (Fig. 4).<sup>95,96</sup> The procedure introduces a significant number of adjustable parameters as standard combination rules are not employed. The GoIP-CHARMM force field for metal–protein interactions, for example, adopts this procedure. The metal–organic interaction parameters from the training set of adsorbed molecules in the gas phase are then applied to simulate adsorption in the liquid (condensed) state at 100 to 1000 times higher density. The performance of GoIP parameters is similar to INTERFACE parameters in metal–organic simulations.<sup>38,97</sup> However, the experimentally supported concept of soft epitaxy has not been verified (see Section 3.1) and the accuracy tends to be lower. The DFT-derived Hamiltonian still cannot reproduce the structure and the energy of the inorganic component, *i.e.*, the metal or inorganic structure collapses when atom mobility is allowed and surface energies are not reproduced. Also, the assumption is made that, after fitting empirical parameters to reproduce gas phase adsorption properties (a two-component system), the same parameters will function in the liquid state (a three-component system at much higher density). This assumption is often not true as chemisorption is more likely in the gas phase and physisorption is more likely in the condensed phase due to higher coordination numbers. Experimental evidence indicates that binding sites of molecules often differ between gas phase and liquid phase.<sup>37,98–100</sup> Nevertheless, DFT-derived force fields for inorganic compounds<sup>97,101</sup> have also adopted integration into polynomial force fields such as CHARMM similar to the INTERFACE approach.

Studies of inorganic–organic binding have also been reported using the Rosetta program.<sup>102–104</sup> Rosetta was originally developed for docking studies of drug molecules onto proteins and

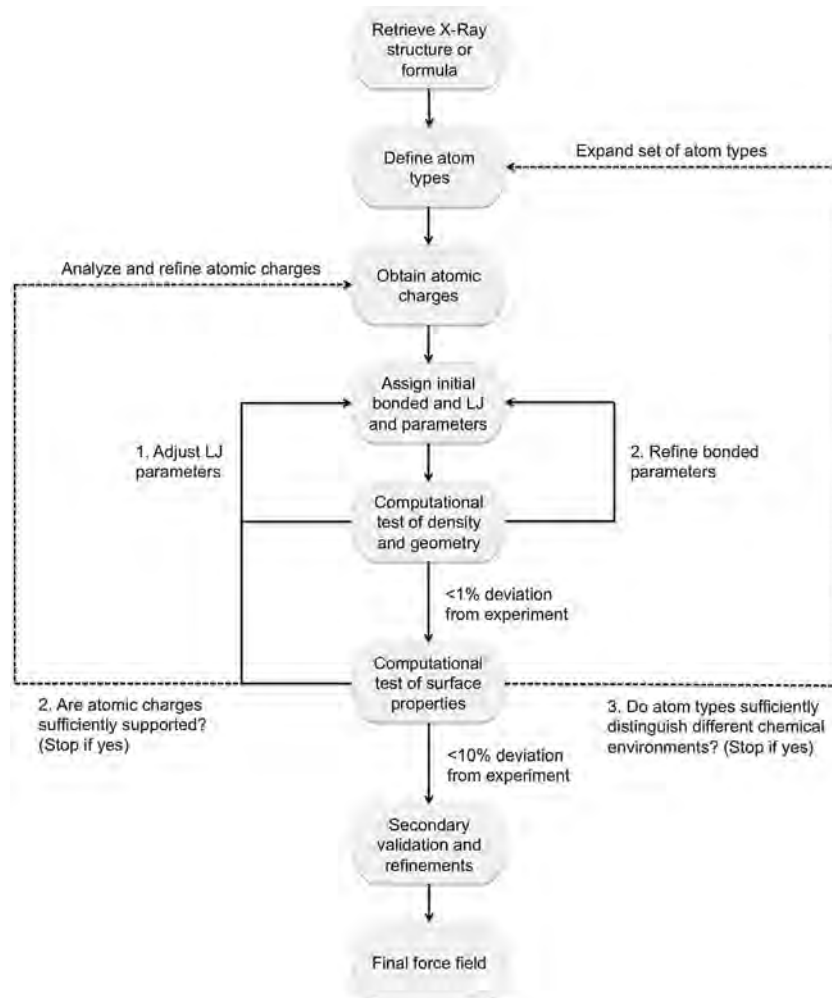


Fig. 3 Flow chart for the development of chemically and thermodynamically consistent force field parameters for new compounds in the INTERFACE force field. The procedure is valid for any compounds across the periodic table. Reproduced with permission from ref. 11.

protein–protein interactions.<sup>105,106</sup> The Rosetta program also depends on accurate force fields and surface models for the inorganic components to be able to function for inorganic–organic interfaces in high accuracy. The necessary parameters can be provided by external force fields such as CHARMM-INTERFACE<sup>11</sup> or individual parameterizations.<sup>20,68,69,78,101</sup>

In summary, understanding of the chemistry of the new compounds to be parameterized and a fully functional Hamiltonian for both inorganic and biomolecular components are essential to carry out reliable simulations of inorganic–bioorganic materials. For best results, force fields need to accurately represent chemical bonding *via* atomic charges (and possibly further details of electronic structure) and reproduce the structure as well as the surface energy of a given compound in comparison to experiment. The derivation of a classical Hamiltonian is possible following the INTERFACE approach and *ab initio* data are helpful in the validation of specific inorganic–organic interactions.

### 2.3. Why is it important to validate surface energies?

Experimental, computational, and theoretical evidence shows that nucleation and growth, assembly and disassembly of

inorganic–organic hybrid materials strongly correlates with the nature of the substrates and their surface chemistry. Certain metal nanoparticles (Pd, Pt, Rh) form well-defined nanocrystals at dimensions below 2 nm,<sup>107–111</sup> while oxide nanocrystals such as silica and titania grow into tens and hundreds of nanometer in size including porosity and other defects.<sup>82,112–115</sup> Polymers and proteins assemble into nanoparticles with even less structural order due to reversible self-assembly or cross-linking, respectively.

Structural definition and stability of nanostructures notably decreases from metals *via* minerals to soft macromolecules and correlates with the surface energy, or cleavage energy, of the material (Table 1).<sup>68,80,116–123</sup> The surface energy of a solid is defined most conveniently as the cleavage energy of the lowest energetic (*h k l*) plane to create two equal surfaces, or as a weighted average of the cleavage energy of all bounding (*h k l*) facets, respectively.<sup>69,84</sup> At 298 K, the surface energy is a suitable measure of the internal energy for most metals and minerals.<sup>69</sup> Alternatively, the cohesive energy (vaporization energy) has often been used,<sup>124</sup> however, vaporization may require temperatures of several thousands of Kelvin at which materials properties change and also force field parameters require adjustments

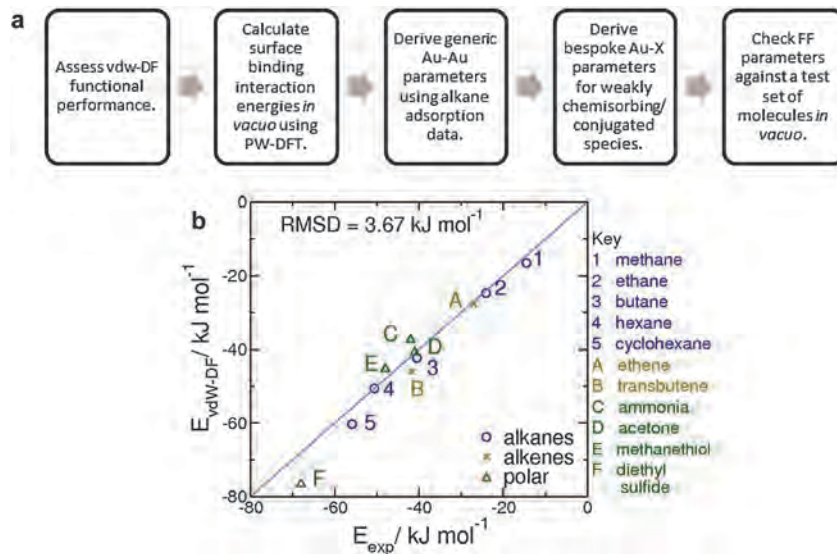


Fig. 4 Development of parameters for metal–protein interfaces in the GoIP force field. (a) Steps to parameterize the Au(111) and Au(100) surfaces using DFT in vacuum. (b) Correlation between experimental interaction energies for small molecules adsorbed onto the Au(111) surface and those calculated with vdW-DF in vacuum. The force field is then typically applied in the condensed phase and positions of metal atoms must be fixed to avoid structural collapse. Reproduced with permission from ref. 101.

relative to standard conditions. This problem is circumvented using surface energies at 298 K. For liquids, the free surface energy equals the surface tension and values are well known.<sup>125</sup> Distinctions between surface energy and surface free energy are not critical here because the quantities are very similar for solids (surface free energies are between 0 and 30 mJ m<sup>-2</sup> lower than surface energies due to small entropy gain upon cleavage).<sup>69</sup>

The surface energy, as a measure of internal cohesion at 298 K, is roughly proportional to the cohesive energy, melting point, and boiling point. It represents the cost to create bare surface area. Therefore, a higher surface energy corresponds to smaller critical size and better definition of nanoscale crystallites during nucleation and growth. A lower surface energy is equivalent to decreased definition and decreased regularity of nanostructures. In principle, it is thus feasible to produce a better-defined nanostructure when the corresponding surface energy is higher – within the existing range over more than two orders of magnitude (Table 1). These correlations suggest that it is critical for models to capture surface energies and associated interfacial properties in quantitative agreement with experiment.

Newer force fields such as the INTERFACE force field achieve such agreement with less than 5% error, essentially in the same accuracy as experiment.<sup>11</sup> Alternative force fields, however, deviate up to 500% due to erroneous assignments of atomic charges and missing validation of surface properties.<sup>23,90,126,127</sup> DFT methods also have notable limitations in the reliable computation of surface energies, for example, underestimates by 20% to 50% are common using GGA density functionals for metals.<sup>33,128</sup> This deviation is large enough, for example, to lose the distinction between surface properties of Au, Pd, and Al (Table 1).<sup>116</sup> Force fields with validated surface properties

Table 1 Surface free energy (cleavage free energy) of various materials classes in decreasing order (data from ref. 68, 80, 116–123, 134 and 135). Higher values correlate with smaller accessible size of nanocrystals and better controllable order

Compound	Cleavage energy of least energetic facet (mJ m <sup>-2</sup> )	Corresponding facet
Diamond	11 300	(111)
W	2990	(110)
Pt	2460	(111)
Pd	1980	(111)
Au	1540	(111)
Ag	1320	(111)
Tricalcium silicate	1300	(001), (040)
Muscovite mica	375	(001)
Sodium chloride	330	(100)
Graphite	190	(001)
Hydrated silica	70–250	NA
Nylon-4	49	NA
Polypeptides	35–50	NA
Polyethylene	30–37	NA
Polydimethylsiloxane	20–23	NA
Gases (H <sub>2</sub> , He, O <sub>2</sub> , N <sub>2</sub> )	< 0.1	NA

therefore offer high accuracy at low computational cost, and satisfy the condition that a model Hamiltonian should reproduce both structures and energies in agreement with experiment.

#### 2.4. Impact of the surface energy on stability, order, and growth of nanostructures

The surface energy is thus directly related to the stability, order, and growth of nanostructures. The following examples illustrate this relation and aid in understanding the discussion of molecular recognition and crystal growth in Sections 3 to 5.

At the top of the scale, the cleavage energy of 11300 mJ m<sup>-2</sup> of diamond correlates with the dissociation energy of covalent C–C bonds which need to be broken to create surface area.<sup>118</sup>

The extraordinary bond strength lets expect the feasibility of very small, stable diamond nanostructures in a size range of 1 to 3 nm.<sup>129,130</sup> The practical size limit of nanodiamonds by detonation synthesis is currently 4 to 5 nm due to poorly controllable conditions with this method and graphitic overlayers.<sup>130</sup>

High surface energies over  $2000 \text{ mJ m}^{-2}$  are also found among transition metals such as W, Pt, and Pd,<sup>71,88,99</sup> which can be synthesized *via* reduction of soluble precursors in solution. The metal nanostructures achieve a high degree of crystallinity related to the high surface energy. Platinum, for example, can form small octahedra, cuboctahedra, and tetrahedra of 2 to 5 nm size using short peptide ligands to arrest crystal growth.<sup>85,109,110,131</sup> Gold with a lower surface energy of  $1540 \text{ mJ m}^{-2}$  forms larger nanoparticles of 11 to 14 nm size under comparable conditions and peptide ligands of similar size.<sup>132</sup>

Minerals show yet lower surface energies in the range of 1300 to  $200 \text{ mJ m}^{-2}$ , for example,  $375 \text{ mJ m}^{-2}$  for muscovite mica, owed to a combination of ionic and covalent bonding (Table 1). Weaker surface forces, including higher surface reactivity and pH-dependent surface chemistry, make it difficult to synthesize specimens with nanometer-scale control.<sup>82,112–115</sup> The propensity towards irregular surface structures, porosity, and defects is much increased.

Polymers, proteins, DNA, and other soft molecules exhibit surface energies on the order of  $20$  to  $70 \text{ mJ m}^{-2}$ ,<sup>121,133</sup> owed to yet weaker self-assembly forces. At a surface energy nearly two orders lower than that for metals and oxides, crystallization is typically difficult to achieve. Defects, and polymorphism are well known. The range of surface and interfacial interactions is widely tunable depending on pH, ionic strength, solvent, temperature, and residue-specific recognition. The contribution of entropy to structural assembly often becomes significant due to low enthalpic driving forces. Perfect order and nanometer-scale control can be extraordinarily difficult to achieve.

Gases reach the limit of zero surface energy and highest disorder at the bottom of the scale of surface energies, and are thus often described as ideal gases without intermolecular interactions in statistical thermodynamics.<sup>25</sup> These considerations show that the scale of surface energies and associated interfacial energies over more than four orders of magnitude ( $10^4$  to  $<10^0$ ) offers a pathway to rationalize material behavior on the nanoscale such as molecular assembly and crystal growth for different types of compounds. When such understanding or prediction shall be derived from molecular simulations, the necessity for truthful implementation of surface energies and surface chemistry in molecular models becomes clear.

## 2.5. Relative strength of interatomic interactions

Observed cohesive and surface energies thus correlate with mechanisms of molecular recognition, interfacial assembly, and crystallization. Down to the atomic scale, cohesive, surface, and interfacial interactions are determined by interatomic interactions. The force field parameters in a given energy expression encode these interactions and determine the outcome of simulations. Understanding interatomic interactions and translating the knowledge into the Hamiltonian is therefore

at the root of modeling and simulation. The types of bonding and their connection to surface and interfacial properties is briefly described in the following.

Common types of bonds include covalent bonds, metallic bonds, ionic bonds, and “nonbond” intermolecular interactions (dipolar, hydrogen bond, van-der-Waals interactions). The present types of bonding in a given system determine thermodynamic as well as kinetic properties. Covalent bonds such as C–C and H–H bonds are typically associated with bond energies on the order of  $100 \text{ kcal mol}^{-1}$  and explain, for example, the high surface energy of diamond (Table 1).<sup>125</sup> Weaker covalent bonds with somewhat longer bond lengths than usual or multi-site coordination are also found, such as Au–S bonds in thiol-modified gold nanostructures.<sup>136,137</sup> The energy of weak covalent bonding is in a similar range as the cohesive energy in noble metals, on the order of  $30$  to  $50 \text{ kcal mol}^{-1}$ .<sup>125</sup>

In contrast, however, metal bonding in elemental metals involves high coordination numbers (8 to 12) and is delocalized across the atoms in the lattice. The strong cohesion can be represented by a combination of intense van-der-Waals and local Coulomb interactions, taking into account the density of valence electrons.<sup>69,71</sup> The implementation of these interactions in force fields reproduces densely packed structures with long range order, high surface energies, and high elastic moduli in simulations. Surface reconstruction,<sup>138,139</sup> reversible removal of single metal atoms in catalytic reactions,<sup>81,140</sup> and etching mechanisms are known.<sup>141,142</sup> The simulation of such processes by computer models on the 1 to 100 nm scale is possible and partly still a challenge.

The strength of partially ionic and partially covalent bonds found in minerals ranges from  $30$  to  $150 \text{ kcal mol}^{-1}$  per pairwise bond. Contrary to earlier beliefs, it has been shown that a majority of minerals is predominantly covalent, many are predominantly ionic, and only few are more than 95% ionic.<sup>19</sup> Aluminates, silicates, and many transition metal oxides are examples of primarily covalent compounds while, at the other end of the spectrum, several alkali halides and  $\text{CaF}_2$  are fully ionic.<sup>143–146</sup> The actual balance between covalent *versus* ionic contributions determines the physical and chemical properties. An accurate representation of chemical bonding by atomic charges, or a more detailed depiction of the electronic structure,<sup>70,71</sup> is essential to ensure the quality of force fields and molecular models. For example, NaCl is well described with a Na charge of  $+1.0e$ , but RbI rather features a Rb charge of  $+0.8 \pm 0.1e$ ,  $\text{BeF}_2$  a Be charge of  $+1.0 \pm 0.1e$ , and  $\text{SiO}_2$  a Si charge of  $+1.1 \pm 0.1e$ .<sup>19,68,78,80,145,147</sup> Charges in complex anions are much lower than formal charges, too, for example,  $\text{SO}_4^{2-}$  is described by a S charge of  $+0.4 \pm 0.2e$  and O charges of  $-0.5$  to  $-0.6$ , depending on the present cation.<sup>11,19</sup> The representation of bond polarity along with van-der-Waals interactions is essential to reproduce multipolar interactions and surface energies of minerals in molecular simulations. Chemically realistic, convergent charges for classical simulations can be derived from experimentally reported electron deformation densities, dipole moments, an extended Born model, chemical reactivity in heterolytic reactions, trends in melting points and solubility in common solvents,

as well as *ab initio* methods.<sup>19,125</sup> Predictive simulations also depend on the consideration of appropriate surface chemistry that can be altered by hydration or protonation reactions.<sup>82,148</sup>

Nonbonded-only interactions are significantly weaker than covalent or ionic interactions and account for surface energies at the lower end of the spectrum. Examples are the interactions between entire organic macromolecules and solvents (assuming unbreakable covalent bonds within). Ion-ion and ion-dipole nonbonded interactions still contribute significantly up to tens of kcal mol<sup>-1</sup>, similar to weak covalent bonds. Hydrogen bonds have a strength of 1 to 5 kcal mol<sup>-1</sup>.<sup>149</sup> Van-der-Waals interactions are the weakest nonbond forces and result from pairwise interactions that individually contribute 0.02–0.2 kcal mol<sup>-1</sup> per pair of atoms (H···H, C···H, O···O, etc.).<sup>68,150</sup>

The foregoing discussion shows that, ultimately, the different types of interactions determine different mechanisms of molecular recognition, assembly, nanostructure growth, and material performance in multiphase systems. These processes can be observed in experiment and in simulations, given reliable force field parameters, and will be reviewed in the following sections.

### 3. Recognition of biomolecules on metal and semimetal surfaces and nanostructures

Metal nanoparticles of different size and shape find applications in therapeutics,<sup>151–153</sup> sensors,<sup>154,155</sup> nanoelectronic devices,<sup>141,156</sup> and catalysts.<sup>140,157</sup> The mechanisms of molecular recognition by organic ligands, especially non-thiols, have recently been explained with the help of molecular simulations.<sup>32,37,38,43,58,81,83,85,87</sup> Knowledge of driving forces for molecular recognition, crystal growth, and shape development can guide in materials design and performance predictions.

#### 3.1. Molecular mechanisms

Molecular simulations of different peptides on extended gold, palladium, and platinum surfaces in aqueous solution using the CVFF-INTERFACE and CHARMM-INTERFACE force field have shown differences in the attraction to (111) and (100) facets.<sup>58</sup> The differences in binding energy are relatively independent of the actual peptide sequence, whether chosen as a random control sequence such as Gly<sub>10</sub> and Pro<sub>10</sub> (Fig. 5) or identified as a strong binder by phage display (A3, S7-2) (Fig. 6). All peptides are strongly attracted to (111) surfaces, up to –50 kcal mol<sup>-1</sup> for a 12-mer peptide on Au(111), and much less attracted to (100) surfaces, typically with small negative or near-zero adsorption energies of 0 ± 5 kcal mol<sup>-1</sup>. While the trend is universal, the precise affinity to each surface and the binding differential between (111) and (100) surfaces somewhat varies depending on the peptide. The trend of strong attraction to (111) facets *versus* weak interaction with (100) facets is also observed on several different fcc metals such as Ag, Au, Pd, and Pt. The magnitude of attraction of the same peptide to (111) facets of different metals is roughly proportional to their surface energy, *e.g.*, the strength of binding decreases in the order

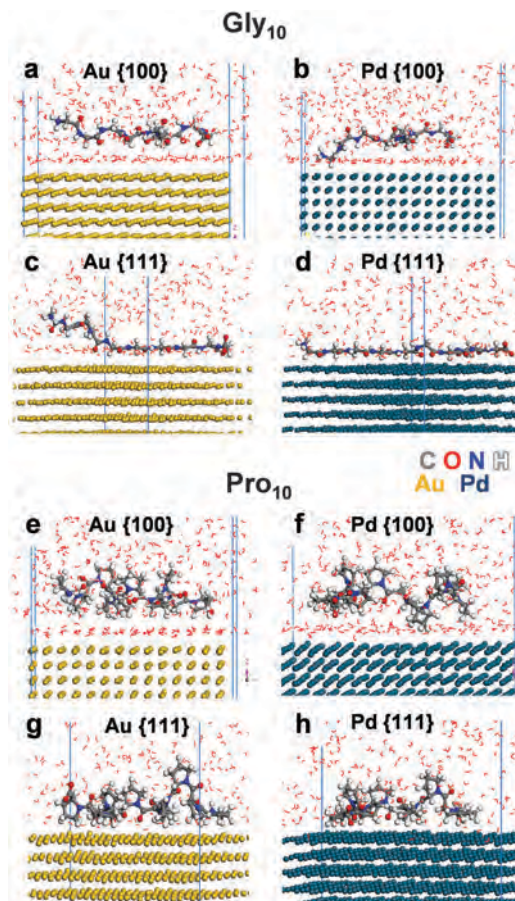
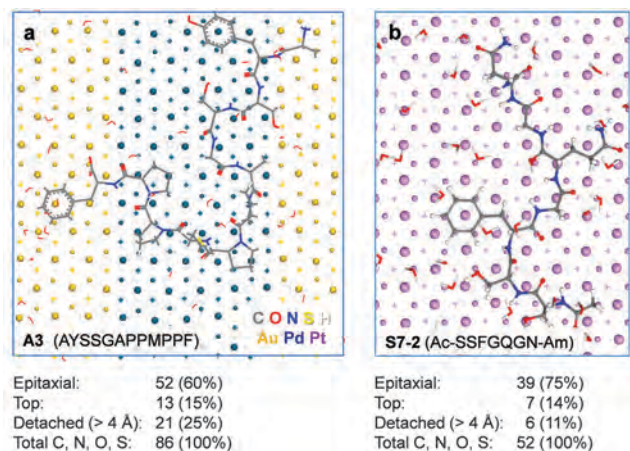


Fig. 5 Snapshots of glycine and proline decapeptides in contact with (100) and (111) surfaces of gold and palladium in aqueous solution. Direct contact with the (111) surface is seen, resulting in stronger adsorption and adaptation of the proline helix. A water interlayer remains on the (100) surface where adsorption is about an order of magnitude weaker. Reproduced with permission from ref. 58.

Pt > Pd > Au > Ag (Table 1). It has also been observed that residues such as F, R, Y, W, H, as well as D spend more time in close contact with (111) surfaces than others while generally most residues are in direct contact with the (111) surface.<sup>37,38,43,58,81,85,157–160</sup> In contrast, a water interlayer is maintained between most residues and the (100) surface, thus resulting in lower adsorption energy (Fig. 5).

The observations in atomic resolution and the trends in computed binding energies are consistent with a number of experimental observations. Peptides were repeatedly reported to bind to extended (111) facets in various studies by phage display while no significant binding was reported to extended (100) facets.<sup>11,37,38,58,83,85,87,140,157,161–165</sup> Apparently stronger binding of “gold binding peptides” (*i.e.* peptides combinatorially selected as binding to gold) to palladium and platinum as well as considerable binding of the same peptides to silver were found experimentally as well.<sup>85,108,132,162,166</sup> The mechanism of adsorption based on these simulation results and experimental data was thus concluded to involve soft epitaxial adsorption, which is characterized by the coordination of polarizable atoms (C, N, O) in the peptides with epitaxial (fcc, hcp) sites on the



**Fig. 6** Representative snapshots of the adsorption of peptides on even metal surfaces in aqueous solution show preferential coordination of epitaxial sites, illustrated for (111) surfaces of gold–palladium and platinum metal. The peptides A3 and S7-2 were identified by phage display and tested in experiment for specific binding. The average number of close contacts of polarizable atoms (C, N, O, S) in each peptide with epitaxial sites, top sites, and of surface detachments (> 4 Å distance from the top layer atoms) is given. (a) A 4 : 1 preference for epitaxial sites over top sites is seen on an Au–Pd surface using the CVFF-INTERFACE force field (from ref. 58). (b) An approximate 5 : 1 preference for epitaxial sites *versus* top sites was found on a Pt surface using the CHARMM-INTERFACE force field, related to higher surface energy of Pt and stronger adsorption (from ref. 85). Metal atoms are shown as large spheres, small spheres, and crosses to distinguish top layer atoms from atoms in subjacent layers that constitute epitaxial sites. Adapted with permission from ref. 58 and 85.

metal surface (Fig. 6 and 7). This concept offers a unique explanation as common  $sp^2$  and  $sp^3$  hybridized groups in peptides exhibit a very good geometric fit to (111) metal surfaces (Fig. 7a), independent of the type of metal present (Fig. 7b). In particular, the phenyl ring of hexagonal symmetry can best coordinate (111) surfaces in contrast to (100) and (110) surfaces. On (110) surfaces, linear molecules have better probability to coordinate epitaxial sites.<sup>83,164</sup> The strength of adsorption is finally a result of competition between the solute molecules and water molecules, which tend to be more mobile and adjust to any type of (*hkl*) surface. Therefore,  $sp^2$  and  $sp^3$  groups cannot effectively compete with water molecules for epitaxial sites on (100) surfaces, leading to a water interlayer and smaller adsorption energies (*i.e.* closer to zero). The phenyl ring, for example, typically assumes tilted conformations relative to the (100) surface plane whereas a flat-on parallel conformation is observed on (111) surfaces.<sup>58,85</sup> Of particular interest is also the characteristic lattice spacing L1, L2, L3 of individual metal surfaces, which provides a measure of the “degree-of-fit” to adsorbing molecules and a tool to rationally design new molecules for binding to a given metal surface (Fig. 7). It is also notable that the area density of epitaxial metal interaction centers on the (111) facet is higher than that on (100) facets, which contributes to stronger attraction of the adsorbates.

The optimum coordination of epitaxial sites on (111) surfaces can be nicely seen in detail for arginine (Fig. 8). Polarizable atoms avoid proximity to metal atoms in the top layer, and molecular

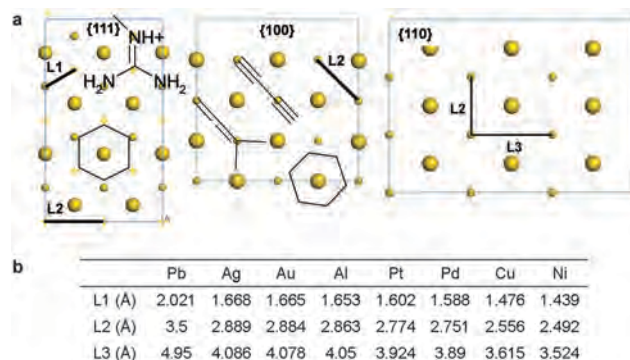


**Fig. 7** Concept of soft molecular epitaxy. (a) The hexagonal symmetry of the (111) surface provides epitaxial sites (fcc and hcp) that match the common geometry of  $sp^2$  and  $sp^3$  hybridized molecules such as benzene and guanidinium groups. (100) surfaces exhibit a square geometry of 2.88 Å spacing that is incommensurate with typical chain molecules (yet suitable for allenes and polyynes). The competition between solvent (water) and solutes is then in favor of water and no significant attraction of the organic molecule is achieved. (110) surfaces possess small and wide grooves that can be further enlarged by surface reconstruction. Due to the larger L3 spacing, adsorption on (110) surfaces is less molecule-specific. (b) The similarity in characteristic spacing of epitaxial sites (L1, L2, L3) leads to similar attraction of molecules and polymers to different noble metals. Differences in attraction, however, arise from unique surface energies and non-identical characteristic spacing. Matching molecules can be designed according to the surface pattern of epitaxial sites, aided by simulation to quantify binding strengths. Reproduced with permission from ref. 83.

dynamics computations have quantified the affinity of all 20 amino acids as well as some surfactants (single molecules) to the Au(111) surface in aqueous solution (Fig. 9).<sup>83,160</sup> Using the same thermodynamically consistent Lennard-Jones parameters for the fcc metals,<sup>69</sup> the trend depends somewhat on the force field parameters for the amino acids. Results with CHARMM-INTERFACE are somewhat preferred over CVFF-INTERFACE, since CVFF is somewhat less validated for biopolymers and overestimates the attraction of aromatic molecules. In experiment,

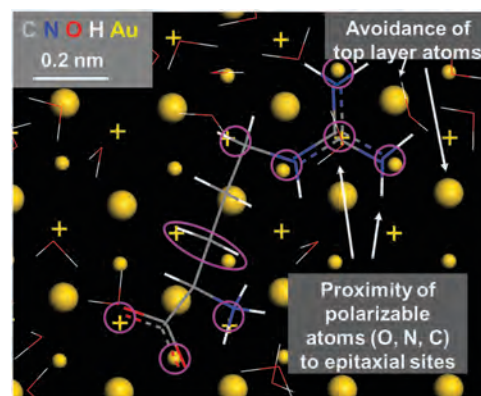


**Fig. 8** Illustration of soft epitaxial adsorption of arginine in aqueous solution on a gold(111) surface according to molecular dynamics simulation. Several epitaxial contacts are highlighted by pink circles. The molecule moves laterally on the surface by a hopping mechanism to other surface sites with similarly good epitaxial coordination in intervals on the order of 100 ps at room temperature. Reproduced with permission from ref. 83.

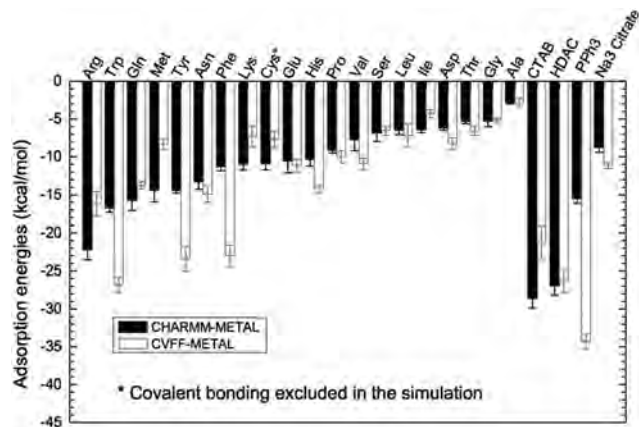
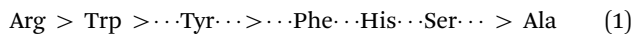


Fig. 9 Computed adsorption energies of the natural amino acids and selected surfactants on gold(111) surfaces in solution. Results of the CHARMM-INTERFACE and the CVFF-INTERFACE force field are shown. The data refer to single molecules in the limit of high dilution. Note that binding of cysteine is the strongest of all due to the formation of covalent bonds ( $+50 \text{ kcal mol}^{-1}$ ), which is unique for this amino acid and was excluded in this tabulation. Reproduced with permission from ref. 83.

the approximate relative strength of adsorption inferred from the abundance of amino acids in gold-binding peptides identified by phage display and from other metal-binding peptides is:<sup>108,132,162,163,167,168</sup>



The simulation results show the same order of attraction to gold(111) surfaces as computed with the CHARMM-INTERFACE force field (Fig. 9). Further supporting evidence includes the attraction of metal binding peptides such as A3 and GBPs in experiment to Ag(111), Au(111), and Pd(111) surfaces, which is explicable by the similar L1 spacing (Fig. 7b). Studies by several research teams have also shown that only peptides containing strongly binding amino acids, or such amino acids alone, could stabilize and control the shape of nanoparticles synthesized reductively from solutions of metal salts.<sup>169,170</sup> An interesting discovery of amino acid sub-lattices on copper surfaces was made over 30 years ago by Low Energy Electron Diffraction (LEED) measurements (Fig. 10).<sup>98</sup> The likely arrangement of polarizable atoms due to the orientation of the sub-lattice indicates a preference for epitaxial contacts and the avoidance of top layer atoms. Further adsorption data of alkane monolayers on Pt(111) surfaces also strongly support soft epitaxial order.<sup>99</sup>

A secondary contribution to peptide binding also arises from attractive polarization of the metal surface by induced charges. This contribution gains relevance in the presence of ionic groups and can become dominant for the adsorption of ionic liquids.<sup>38,87,164,171</sup> Induced charges typically play a subordinate role in the first molecular layer of contact when epitaxial binding is strong, such as for peptides on (111) surfaces.<sup>87</sup> Induced charges can become primary contributions to adsorption of charged molecules and ions on epitaxially less attractive surfaces, however, such as highly ionic peptides on (100) surfaces.

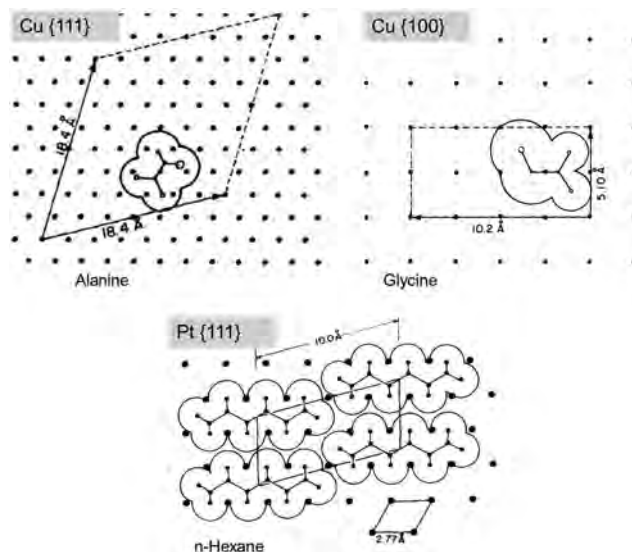
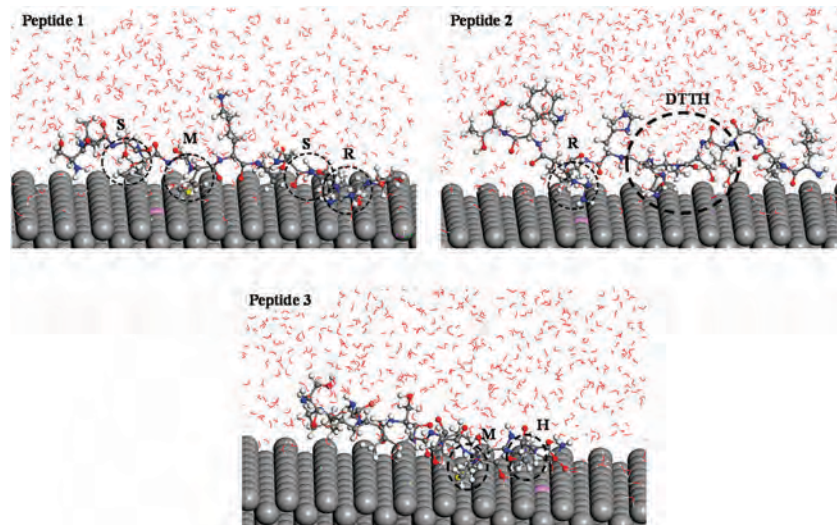


Fig. 10 Packing of amino acid and alkane monolayers on metal surfaces according to data from Low Energy Electron Diffraction (LEED). The observations provide evidence for preferential binding of polarizable atoms to epitaxial sites rather than top sites in the condensed phase, consistent with close packing. Experimental and computational data explain and support this view (ref. 37, 58, 83, 85, 87, 157 and 164 and references cited therein). Adapted with permission from ref. 98 and 99.

The overall attraction due to induced charges increases with the magnitude of charges and the distance between corresponding positive and negative charges in a surface-adsorbed molecule, *e.g.*, between charges on the backbone and the position of counter ions in solution. Contributions by induced charges diminish facet selectivity. Additional contributions to adsorption of organic molecules to metal surfaces in solution may also arise from weak covalent bonding.<sup>21,101,172</sup>

The understanding of molecular adsorption on various metal surfaces has also been aided by simulations using density functional theory and tight binding methods.<sup>32,96,173–176</sup> However, such studies have mostly been carried out in vacuum and cover very short time scales due to limitations in system size. Conclusions about the properties of aqueous interfaces therefore remain unclear. An added complication with DFT and tight binding methods is also the large deviation of computed surface and interfacial energies of metals from experimental measurements of up to 50%.<sup>33,128</sup> The CHARMM-INTERFACE force field, in comparison, reproduces surface energies with less than  $<5\%$  deviation from experiment. In addition, computed cell parameters of the metals, interfacial tensions with water, and binding constants are clearly in better agreement with experiment.<sup>11,43,69</sup> Alternative force fields also include the GolP and GolP-CHARMM force fields which require fixed metal atoms and incorporate rod-like dipoles to account for polarizability.<sup>21,101</sup> The models collapse when metal atoms are allowed flexibility and are mainly applicable to idealized surfaces.

Specific binding of peptides selected by phage display has also been computationally studied on semimetals such as silicon<sup>177</sup> and graphene.<sup>178–181</sup> On the  $n^+$  silicon (100) surface, three peptides identified by phage display were found to be attracted with binding energies of  $-12$ ,  $-15$ , and  $-7 \text{ kcal mol}^{-1}$  (Fig. 11).



**Fig. 11** Molecular dynamics snapshots (side views) of peptides P1, P2, and P3 adsorbed on the n+ Si(100) surface in explicit solvent with buffering ions (137 mM PBS, pH 7). SVSMGMKPSRP (P1) was computed to bind with an energy of  $-11.5$  kcal mol $^{-1}$ , LLADTTHRPWT (P2) with  $-14.5$  kcal mol $^{-1}$ , and SPGLSLVSHMQT (P3) with  $-7.0$  kcal mol $^{-1}$ . All three peptides were experimentally identified by phage display and binding residues are highlighted. Reproduced with permission from ref. 177.

Within the sequences, methionine and tryptophane were found to increase attraction, as well as D, T, H, S, and R. The diamond cubic (100) silicon surface exhibits long range corrugation without a highly specific epitaxial pattern to match specific amino acid residues. The overall attraction of peptides was then found to be dependent on both sequence and molecular architecture.<sup>177</sup>

In contrast to silicon, graphite and graphene are lower energy surfaces. The cleavage energy is only 190 mJ m $^{-2}$  for graphite and lower for graphene, whereby graphite can be considered a 5+ layer graphene.<sup>134,135,182–184</sup> Therefore, strong epitaxial interactions are not expected and rather the possibility of pi-stacking interactions contributes to moderate adsorption of aromatic molecules (Fig. 12).<sup>178–181,185</sup> Graphite and graphene mainly behave as hydrophobic surfaces and binding energies of amino acids, peptides, and surfactants are somewhat negative in aqueous solution. Common residues with higher affinity include H, Y, W, and F, as well as amide groups in Q and N (Fig. 12). Some of the adsorption is related to depletion interactions, *i.e.*, the hydrogen bonded network in water is less disrupted by adsorption of the molecules onto the graphitic surface, unless many ionic groups are present and favor dissolution in the aqueous phase.

### 3.2. Application of simulation tools to understand crystal growth

An interesting application of the soft epitaxial concept on metal surfaces is the selective stabilization of crystal facets during nanoparticle growth from seed crystals. The stabilizing effect of phenyl rings towards (111) facets predicted from simulation could be applied in the laboratory synthesis of platinum nanocrystals from seed crystals upon reduction of hexachloroplatinic acid in the presence of ascorbic acid as a mild reducing agent (Fig. 13).<sup>85</sup> Different phenylalanine containing peptides were employed as shape-directing templates. About twenty

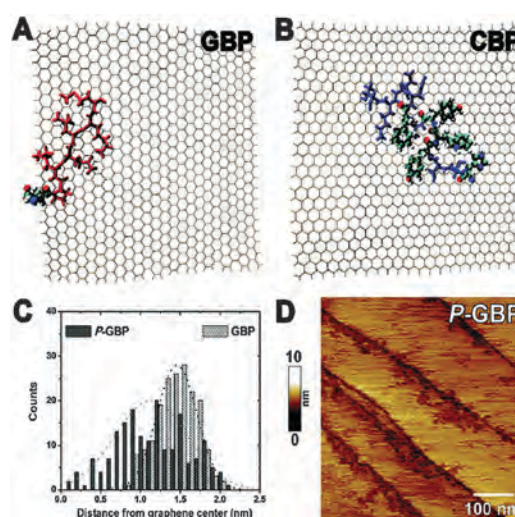


**Fig. 12** Adsorption of a graphene-binding peptide EPLQLKM (GBP) and a carbon nanotube binding peptide HSSYWAFNNKT (CBP) to graphene. (A and B) Lowest-energy conformations of GBP and CBP obtained from MD simulations started from various positions on the surface and on the edge on a 5 nm by 5 nm model surface of graphene. (C) Changes in position of GBP from the center of mass of the graphene layer in deprotonated (GBP) and protonated state at pH  $\sim 3$  (P-GBP). Protonation shifts the position away from the edge toward the center. (D) AFM topography for P-GBP assembled on graphene/graphite at pH 3 shows extensive surface coverage. Reproduced with permission from ref. 179.

neutral, end-protected peptide sequences with and without F showed that the presence of the phenyl ring anywhere in the peptide sequence is sufficient as a molecular switch to convert cuboctahedral or cubic nanocrystals into tetrahedra during growth from seed crystals. Resulting tetrahedra are bounded exclusively by (111) facets, stabilized and slowed down from further growth by the phenylalanine-containing ligands. This synthesis approach

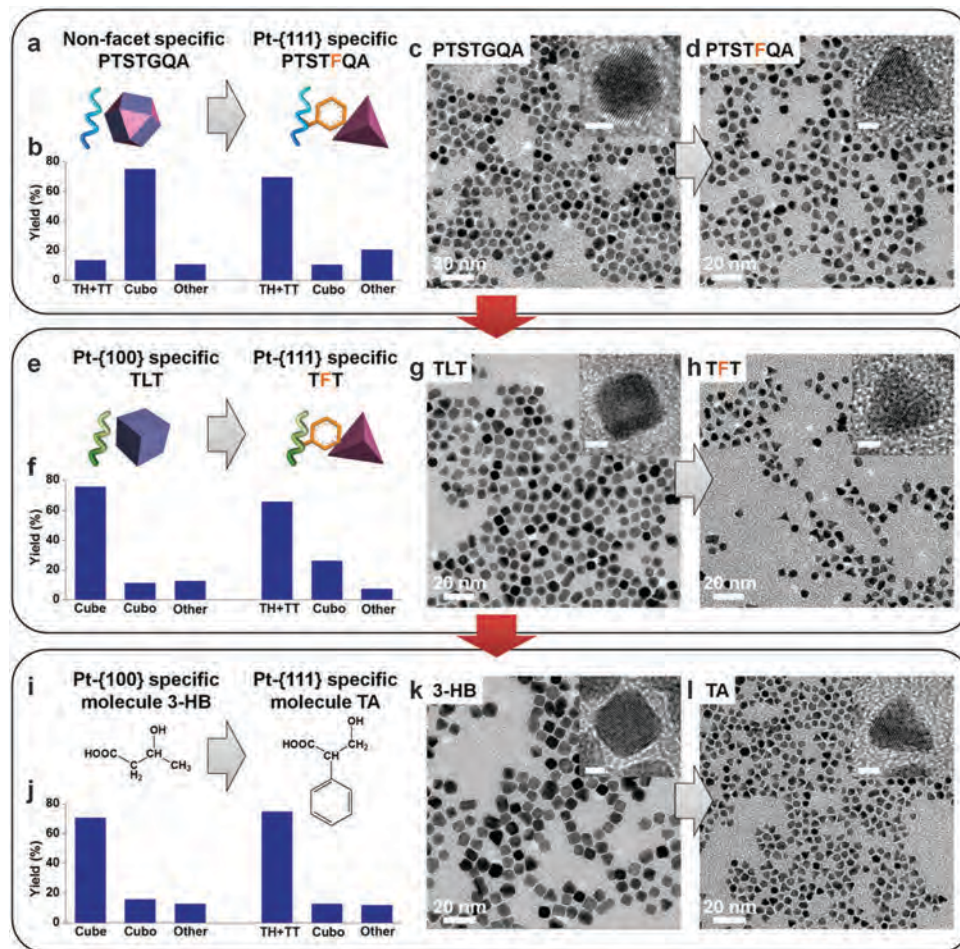


Fig. 13 Application of epitaxial recognition of the phenyl ring by (111) facets in the shape-selective synthesis of Pt tetrahedra. (a–d) A cubooctahedron forming peptide sequence produces Pt tetrahedra upon substitution of one amino acid by phenylalanine. (e–h) A cube forming peptide sequence yields tetrahedra upon substitution of L by F. (i–l) A synthetic ligand is analogously transformed from cube-directing to tetrahedron-directing. High resolution TEM micrographs (c, d, g, h, k, l) indicate shape changes. Adapted and reproduced with permission from ref. 85.

also functions with other ligands such as 2-phenyl-3-hydroxybutyric acid, and with other metals of high surface energy such as Rh nanocrystals.<sup>85</sup>

The main driving force for shape control according to simulation is the binding differential of the peptide to (111) versus (100) surfaces rather than the absolute binding strength to a specific facet (Fig. 14). The binding energy of all peptides, with or without F, is about equal on (111) facets and shows no correlation with tetrahedra yield.<sup>85</sup> However, the binding energy of the peptides to (100) facets correlates with the yield of tetrahedra, whereby F-containing peptides show positive adsorption energy (S7 *etc.*) and F-free peptides negative, attractive adsorption energy (S7-G, PQPN, S7-Y, SSY). Thus, the F-containing peptides leave the (100) facets more accessible to atom deposition and completion of (111) facets. On the contrary, the F-free peptides are slightly attracted to (100) surfaces (Fig. 14) and then protect these facets leading to growth of both (100) and (111) facets.

The elucidation of mechanisms of shape control is also possible for other nanocrystal shapes such as cubes and twins.<sup>43,110</sup>

Nanoparticle shape has a significant influence on adsorption of solvents and solutes (Fig. 15).<sup>37</sup> Overall geometric factors as well as factors related to the pattern of epitaxial sites can be distinguished. Extended surfaces provide many metal atoms in the vicinity of a molecule or polymer to interact with and support strong epitaxial adsorption. Stepped surfaces contain inner edges and outer edges. Inner edges exhibit the highest number of metal atoms to interact with and lead to strongest adsorption, which is reflected in a strongly negative surface potential. These sites are easily accessible by small solvent molecules, however, they may not be sterically accessible by larger molecules. Outer edges are least attractive sites for both peptides and solvent molecules. These differences in local dynamics determine the outcome of the competition between solvent and solute molecules for adsorption, for example, faster solvent motion near the corners of nanocubes can enhance adsorption of less mobile peptides (Fig. 16). Therefore, adsorption is not only a facet-specific process but also depends on the local position of the solute on a finite-size facet. Finally, small nanoparticles with near-spherical geometry exhibit diminished

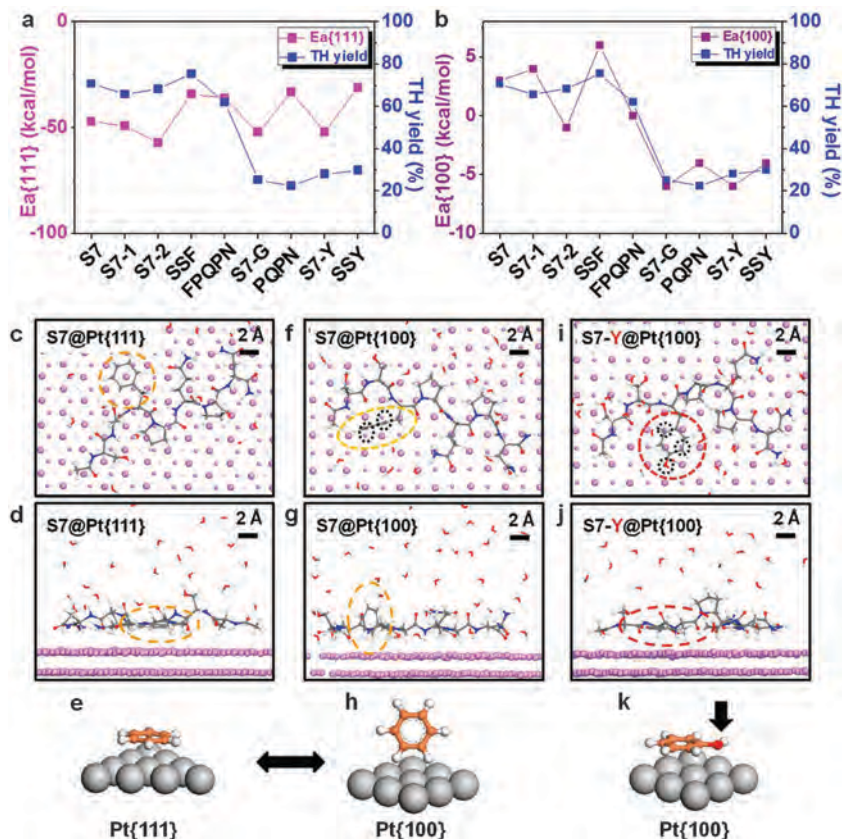


**Fig. 14** The origin of Pt(111) specificity. (a and b) Correlation of tetrahedra yields with computed peptide adsorption energies to Pt(111) and (100) surfaces in solution ( $E_a(111)$  and  $E_a(100)$ ), respectively. TH represents tetrahedra and uncertainties are  $<5\%$  for all data points. (c–e, f–h) Binding configurations of S7 on Pt(111) and (100) surfaces (top view and side view). Configurations of the phenyl ring are highlighted in dashed yellow circles and also schematically illustrated in (e) and (h). (i–k) Binding configurations of S7-Y on Pt(100) surface (top view and side view). Configurations of the phenol ring are highlighted in dashed red circles and schematically illustrated in (k). Black circles in (f) and (i) indicate the differences in epitaxial contacts between phenyl and phenol rings on Pt(100) surfaces, which account for the difference in their binding energy  $E_a(100)$ . Most water molecules are omitted for visual clarity. Reproduced with permission from ref. 85.

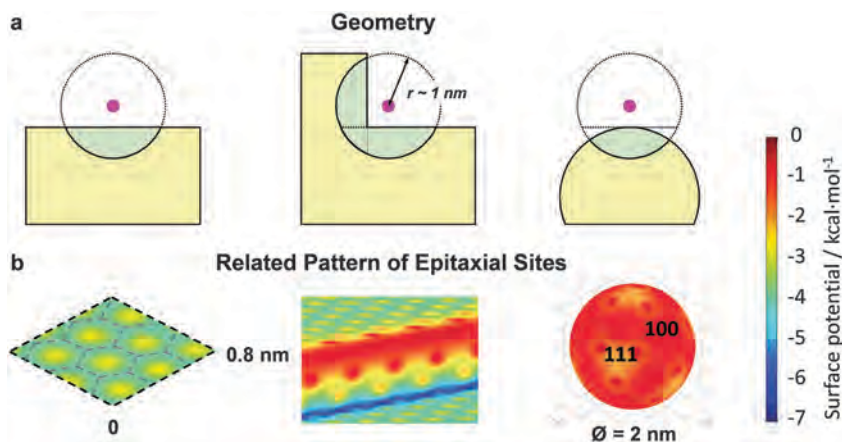


**Fig. 15** Dependence of the adsorption of atoms and molecules on the shape of a metal nanostructure. The strength of adsorption of both solvents and solutes depends significantly on the local surface topology. (a) An atom (pink sphere) or a molecule as a collection of atoms is more attracted to even surfaces and inner edges, and less attracted to small near-spherical surfaces. (b) The surface potential (=attraction of a carbon atom at  $3 \text{ \AA}$  distance) quantifies these preferences and adds in details according to the pattern of epitaxial sites. Strength of adsorption and ligand selectivity are weakest for small nanoparticles. Reproduced with permission from ref. 37.

adsorption of solvent and peptides, including less binding contrast among different peptides, as well as a reduced surface

potential (Fig. 15). Specific data have been reported by simulation<sup>37</sup> and experiment<sup>161,165</sup> in support of these observations.

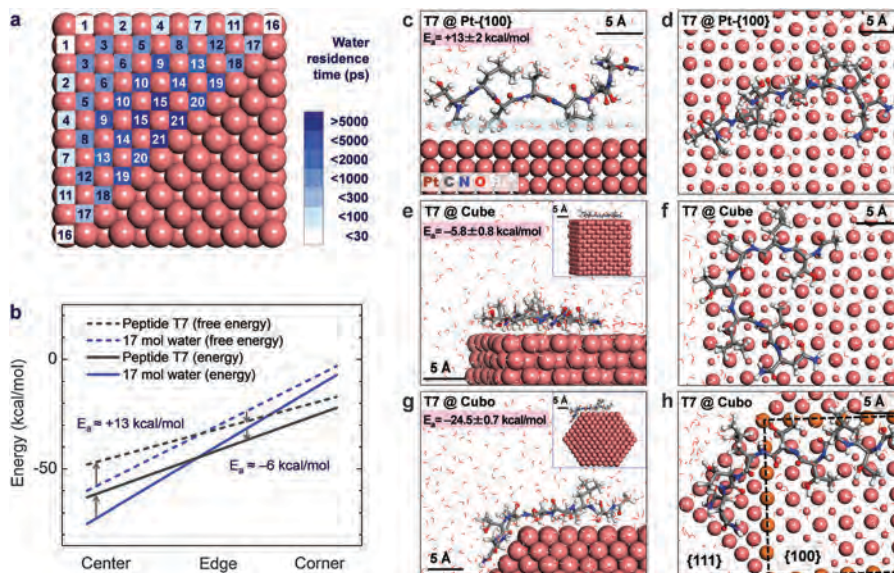


**Fig. 16** Local differences in the adsorption strength and mobility of water molecules on a cubic platinum nanocrystal of 2.35 nm side length and implications for the adsorption of peptide T7. (a) Chemically distinct surface sites are identified by numerical labels. The average residence time describes how strongly a water molecule is adsorbed and how frequently it moves to a neighbor site or away into solution. Average residence times are more than two orders of magnitude higher at the center sites than at the corner sites. Adsorption to extended (100) surfaces is comparable to center portions of (100) facets. (b) Schematic diagram of the spatially resolved binding energy and binding free energy for a fully extended peptide T7 and for 17 water molecules that compete for adsorption. The peptide is weaker bound compared to water in the center, resulting in desorption, and stronger bound than water near the edges and corners, resulting in adsorption at high dilution (energies are approximate). (c–h) Differences in average binding conformation of a single peptide T7 on extended Pt(100) surfaces, cubes, and cuboctahedra according to molecular dynamics simulation. (c and d) The peptide is not attracted to extended surfaces. (e and f) The peptide adsorbs near the edges of a cube where water molecules are more mobile and shows an exceptional fit to epitaxial sites. (g and h) Attraction increases on a cuboctahedron due to the presence of both (111) and (100) facets. The facet boundary is indicated by a dashed black line. (Reproduced with permission from ref. 43).

A well-studied example is the adsorption of peptide T7 (acyl-TLTLTLN-amide) on platinum nanocubes. This peptide was initially selected as a strong binder to cubic nanocrystals by phage display (Fig. 16).<sup>109</sup> Simulations show that peptide T7 significantly adsorbs to the cubic nanocrystals near the edges even though it is not attracted to extended (100) surfaces.<sup>43</sup> The reason for such specific, spatially localized binding preferences is the spatially differential attraction of both water molecules and peptide that compete with each other (Fig. 16a and b). Water molecules are tighter bound at the center of the crystal facets than at the edges, resulting in preferential peptide binding near the edges, supported by conformational matching of polarizable atoms in the peptide to (100) epitaxial sites (Fig. 16e and f). It is not possible, however, for the peptide to displace flexible water molecules at the center of the facets or on extended facets (Fig. 16c and d).

Changes in peptide concentration also have profound impact on attraction *versus* repulsion on the surface. Typically, several peptides cover the metal surfaces in experiment and reported adsorption energies are on the order of  $-5$  to  $-10$  kcal mol<sup>-1</sup> near monolayer coverage.<sup>81,157,186</sup> Computed adsorption energies in simulations are found in the same range at comparable surface coverage.<sup>43</sup> The selective synthesis of Pt cubes in the presence of peptide T7 and analysis by high-resolution transmission electron microscopy (HRTEM) further demonstrated that only intermediate T7 concentration at about 50% surface coverage lead to a high yield of nanocubes. Large-scale MD simulations have monitored

associated changes in facet coverage and adsorption energies of T7 peptides on cuboctahedral seed crystals, which are consistent with concentration-dependent changes in shape, yield, and size of the nanocrystals (Fig. 17). The growth mechanism is thus consistent with adatom deposition, whereby preferential coverage of (100) facets over (111) facets at intermediate concentration promotes the formation of cubes through faster growth and disappearance of (111) facets.

MD simulations have also provided insight into the growth mechanism of metal nanorods in the presence of surfactants such as cetyltrimethylammonium bromide (CTAB) (Fig. 18).<sup>86</sup> CTAB was found to be attracted to (111), (100), and (110) facets of gold and to form ion channels on all surfaces. Thereby, the ion channels on the (111) facets are wider and enable transport of more precursor AuCl<sub>2</sub><sup>-</sup> ions to the gold surface. These differences correlate with the preferred growth of nanorods in the (111) direction by adatom deposition as observed in experiment.<sup>187</sup>

When the solvent is changed to imidazolium based ionic liquids without any added surfactants, the binding strength of the solvent to different facets was found to be nearly the same.<sup>164</sup> Facet preferences of gold precursors during growth are then lost and lead to isotropic growth by adatom deposition, supported by experiment.<sup>188</sup> Facet-specific gradients in adsorption can be introduced by the addition of shape directing agents such as Ag<sup>+</sup> ions during synthesis that were shown to deposit as Ag metal preferentially to (110) and (100) facets according to simulation and underpotential deposition.<sup>164</sup> This process explains

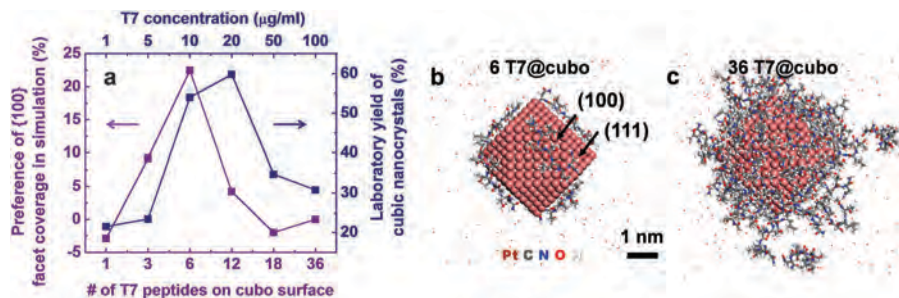


**Fig. 17** Correlation of the yield of cubic nanocrystals as a function of T7 concentration in experiment with the binding preference toward (100) facets as a function of surface coverage in simulation. (a) The preference in (100) facet coverage correlates with the observed laboratory yield of nanocubes. (b and c) Representative snapshots show the binding configuration and relative coverage of (100) and (111) facets on cuboctahedral seed crystals for intermediate and high concentration of peptide T7. Adapted from ref. 43 with permission.

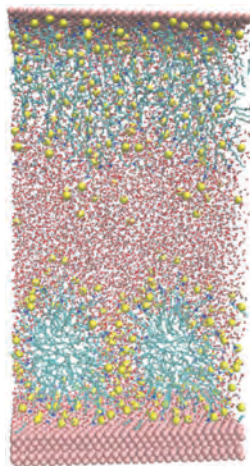


**Fig. 18** Snapshot from an MD simulation of an Au(111) surface with CTAB in water periodic in the horizontal  $x$  direction. A water-ion channel between the micelles allows access of  $\text{AuCl}_2^-$  ions to the surface. The inter-micelle channels are smaller on the (100) and (110) surfaces and explain the preferred growth of gold nanorods in the (111) direction. Reproduced with permission from ref. 86.

anisotropic growth in the (111) direction by adatom deposition as observed in experiment.<sup>189</sup>

Growth mechanisms can also involve cluster attachment to form twin crystals rather than single crystals (Fig. 19).<sup>110,190</sup> This pathway may be kinetically favored when the supply of adatoms is short. The preferred pathway depends on the

reaction kinetics that is influenced by the chosen concentration of ligands, precursors, as well as their interactions. Simulation of the kinetics in full chemical detail remains a challenge due to the long time scales involved in experiments. However, it is feasible to probe precursor–ligand interactions and nanocluster–ligand interactions at any stage along the growth process to estimate activation energies, facet coverage, growth directions, and approximate yield.<sup>110</sup>

### 3.3. Applications to catalysis and sensors

Metallic and alloy nanostructures have great promise as catalysts in electrode materials, biomass conversion, and other chemical reactions.<sup>157,191–195</sup> Noble metal nanoparticles can thereby take on different sizes and shapes. Simulations have shown that near-spherical nanoparticles are characterized by the presence of different facets, including (111), (100), and (110) (Fig. 20).<sup>81,111,140,157</sup> Thermodynamically stable nanoparticles in the size range of 1.5 to 4 nm display these facets in a ratio of about 60:20:20 whereby the amount of (100) *versus* (110) facets varies somewhat as a function of particle size.<sup>140</sup>

Obtaining insight into the exact atomic structure of nanoparticles is experimentally challenging. Equally sloped electron tomography<sup>71,196–198</sup> or high energy X-ray diffraction<sup>81,199</sup> can provide detailed information to build realistic molecular models. Electron tomography directly supplies most atomic positions while data from high energy X-ray diffraction and corresponding pair distribution functions (PDFs) require further processing. Knowing the PDF and total number of atoms in the particle,



**Fig. 19** Growth pathways for metal nanocrystals mediated by peptides: cluster attachment (Path 1) or adatom growth (Path 2). Cluster attachment is more likely when the precursor–ligand complex is specifically stabilized, such as by interactions between histidine and  $\text{Pt}^{2+}$  ions, that lead to an increase in activation barrier, smaller clusters, and twin crystal formation (Path 1). Adatom deposition is faster in the absence of significant precursor stabilization, which leads to larger clusters, and single crystal formation (Path 2). Reproduced with permission from ref. 110.

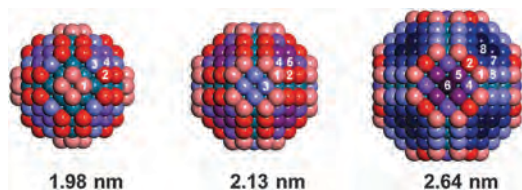


Fig. 20 Models of stable, near-spherical Pd nanoparticles as a function of particle size. Numerical labels and increasingly darker color on the atoms indicate higher atom abstraction energies that play a role in surface reconstruction and surface reactivity. Reproduced with permission from ref. 140.

it is then possible to propose hypothetical nanoparticle structures and test the degree of fit of the computed PDF with the PDF from experiment. Reverse Monte Carlo simulations can identify atomistic models with the best fit, followed by relaxation of the structure by MD simulation.<sup>81</sup> The atomic configurations can serve as a basis to compute reaction rates in comparison to experimental measurements of the turnover frequency (TOF), which is briefly illustrated for a series of peptide-covered Pd nanoparticles in Stille carbon-carbon coupling reactions (Fig. 21).<sup>200–202</sup>

In this reaction, experiment and quantum mechanical data uncover that the rate determining step is the abstraction of Pd surface atoms by an aryl halide (Ar-X) from the peptide-modified surface (Fig. 21a and b).<sup>140,202–204</sup> Reactive molecular dynamics simulations with CHARMM-INTERFACE then allow the quantitative analysis of the activation energies of all available surface atoms, which are proportional to the abstraction energy (Fig. 21c and d). The relative reaction rate of peptide-modified nanoparticles in solution was thus calculated as a Boltzmann-weighted average over the computed abstraction energies of all surface atoms for each nanoparticle (Fig. 21d). The computed reaction rates are in good agreement with TOF measurements

for the individual nanoparticles and enable rate predictions for other hypothetical particle shapes to guide experiment.<sup>81</sup> While catalysts for Stille coupling reactions are used in the synthesis of conjugated polymers for displays, similar computational-experimental approaches can be developed to understand the activity of nanometal and nanoalloy catalysts for other reactions. The combination of experiment, *ab initio* methods, and reactive MD allows to reach the necessary length scale of 1 to 100 nm under realistic solution conditions.

The possibility to modulate electrical conductivity of metal nanostructures and graphene upon specific binding of biological molecules and analytes allows interesting applications in bio-sensors, which operate in the form of small transistors.<sup>205–207</sup> A combination of molecular dynamics and DFT methods can be employed to estimate analyte-induced changes in band structure and electrical conductivity.<sup>207</sup> The reliability is currently still low, however, the prospects of valuable predictions could advance methods development to reach higher accuracy. Sensors have also been developed on the basis of surface plasmon resonance (SPR) and surface enhanced Raman spectroscopy (SERS) of metal nanostructures for high throughput detection of a wide range of biological molecules and human performance analytes.<sup>208</sup> Specifically decorated metal nanoparticles have also been developed and tested for cell targeting, imaging, and therapeutic purposes.<sup>209–211</sup> A range of challenges remain to be overcome in the assembly of metal and semimetal electronic circuits in nanometer precision.<sup>167,212</sup> The examples illustrate a range of applications where understanding and prediction of interfacial recognition on metal and semimetal nanostructures aided by molecular simulation could improve materials performance.

Table 2 summarizes current simulation capabilities to design ligands and nanoparticle shape at the 1 to 100 nm scale

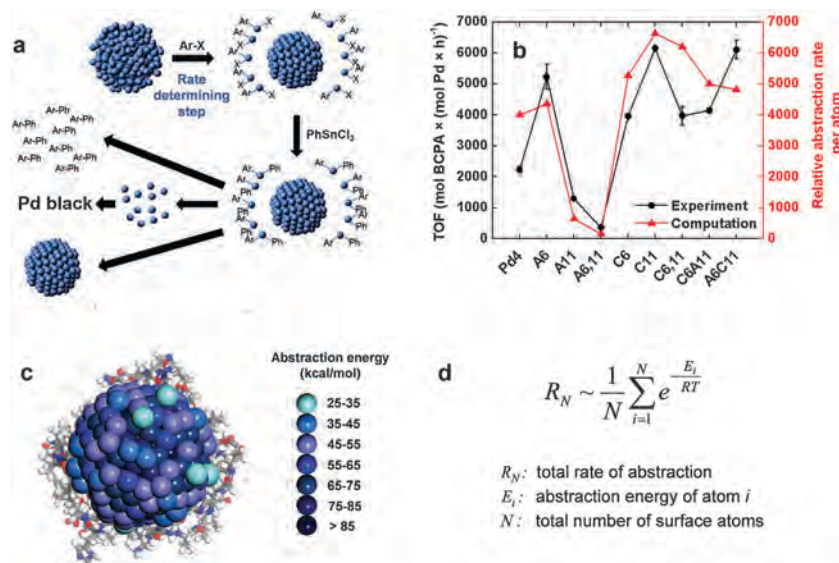


Fig. 21 Catalytic performance of peptide-derived Pd nanoparticles in C–C Stille coupling reactions in experiment and in reactive MD simulation. (a) Reaction mechanism. (b) For nanoparticles derived using the peptides Pd4, A6, A11, etc., the turnover frequency in experiment (TOF) correlates with the computed atom abstraction rate. (c) Illustration of the abstraction energies of individual atoms of the Pd4 nanoparticle (peptide only shown on the outside for clarity). Pd atoms of lowest abstraction energy and high activity are shown in lighter color. (d) Calculation of the relative reaction rate from computed atom abstraction energies. Adapted with permission from ref. 81 and 202.

**Table 2** Emerging capabilities of atomistic simulations to predict ligand binding to metal nanocrystals, rationalize growth preferences in aqueous solution, reactivity, and conductivity at the 1 nm to 100 nm scale (ref. 11, 37, 58, 69, 81, 83, 87, 111, 140, 157, 164 and 207). Adapted with permission from ref. 43

Calculated property	Relation to experiment
Selectivity of peptides to extended and finite-size nanocrystal ( <i>h k l</i> ) facets	Identification of facet specific peptides using phage display
Facet coverage and preferences in facet coverage on nanocrystals	Shape and yield of nanocrystals (HRTEM)
Binding free energies of peptides	Binding constants and size of nanocrystals
Spatial location of peptides on ( <i>h k l</i> ) facets and average distance of residues from the surface	Atomic-level information, EXAFS, IR/Raman spectroscopy
Above properties as a function of the number of peptides on the surface	Above properties as a function of peptide concentration and surface coverage
Spatially and temporally resolved trends in peptide assembly on nanocrystal surfaces	Atomic-level information, QCM, <i>in situ</i> measurements
Reaction rate in rate-determining step (coverage of active sites, atom abstraction, <i>etc.</i> )	Catalyst turnover frequency
Estimates of band structure and conductivity using combined QM/MD approaches	Conductivity measurements, sensor response to analytes

for various applications. Atomistic molecular simulations can accomplish (1) the analysis of ligand selectivity to various (*h k l*) facets and full-size nanoparticles, (2) the analysis of preferences in coverage of facets and of the spatial location of ligands, (3) the computation of binding free energies, (4) the analysis of the concentration dependence of the above properties, (5) dynamic monitoring of ligand assembly on nanoparticle surfaces, (6) predictions of catalytic reactivity with appropriate reactive extensions, and (7) the analysis of changes in conductivity using QM/MD approaches. The accuracy is often quantitative and comparisons to a range of laboratory observations can be made, including phage display, nanocrystal shape and yield in HRTEM, nanocrystal size and ligand binding constants, EXAFS data on coordination numbers, monitoring of molecular assembly using quartz crystal microbalances (QCM), *in situ* techniques, HE-XRD, measurements of turnover frequencies, and electrical conductivity.

## 4. Recognition of biomolecules and ligands on oxide, phosphate, carbonate, sulfide, and other inorganic surfaces

The following section focuses on insight into biological interfaces of silica, phosphates (apatites), carbonates, sulfides, and other heteroatomic inorganic nanostructures. Among these materials are abundant biominerals such as silica, apatite, and calcite that are produced in marine organisms and humans.<sup>10,112,213–218</sup> Silica is one of the most abundant oxides on earth and finds wide application as a drug carrier,<sup>7,219–221</sup> catalyst support,<sup>222–226</sup> filler, and rheology modifier in polymer composites and hydrogels.<sup>227–229</sup> Apatite-collagen matrices

constitute bone and teeth,<sup>215,230–235</sup> and carbonate nanocrystals form the “bricks” in nacre.<sup>236–240</sup> Many other oxides such as ZnO, TiO<sub>2</sub>, and quantum dots have been employed in functional materials, and organic–inorganic recognition is an important factor in the performance.<sup>241–245</sup>

### 4.1. Molecular mechanisms

Adsorption on oxide surfaces such as silica or apatites is governed by a different mechanism in comparison to metals.<sup>36</sup> The surface energy is almost an order of magnitude lower (Table 1) and the surface structure, for the example of silica, is dominated by a locally uneven pattern of silanol groups ( $\equiv\text{Si-OH}$ ) and ionized siloxide groups ( $\equiv\text{Si-O}^- \text{Na}^+$ ). As a consequence, soft epitaxy is an unlikely recognition mechanism. Silica and many other oxide minerals are furthermore insulators rather than conductors and possess no polarizable electron gas of valence electrons as found in metals. Therefore, induced charges do not occur and make no contribution to adsorption.

The reduced surface energy in comparison to metallic substrates leads to much weaker adsorption of the first molecular layer. For example, individual 12-mer peptides binding specifically to silica surfaces in solution possess binding energies of 0 to  $-10 \text{ kcal mol}^{-1}$  while 12-mer peptides binding specifically to noble metal surfaces possess binding energies of 0 to  $-100 \text{ kcal mol}^{-1}$  according to adsorption isotherms and calculations.<sup>36,37,58,217,246</sup> Oxide surfaces are also more polar, reactive, and pH sensitive. As a result, attraction of peptides and synthetic polymers is strongly dependent on conditions such as surface chemistry, pH, ionic strength, and particle surface features including porosity.

Silica surfaces are a representative example for the variety in surface chemistry and the broad range of oxide chemistry in general (Fig. 22).<sup>247</sup> Phage display techniques from one laboratory to another have shown less than 20% in sequence similarity among peptides identified as strong binders under comparable pH conditions, owed to the differences in Q<sup>2</sup>, Q<sup>3</sup>, and Q<sup>4</sup> environments as well as in porosity of the silica surfaces as a function of particle size and synthesis method.<sup>36,248</sup> Thereby, Q<sup>2</sup> surfaces correspond to surface termination with two silanol groups per Si atom  $[(\text{Si-O})_2\text{Si}(\text{-OH})_2]$ , Q<sup>3</sup> surfaces correspond to surface termination with one silanol group per Si atom  $[(\text{Si-O})_3\text{Si}(\text{-OH})]$ , and Q<sup>4</sup> surfaces correspond to surface termination with zero silanol groups per Si atom  $[(\text{Si-O})_4\text{Si}]$  (Fig. 23).<sup>120</sup> The total density of SiO(H,M) groups per nm<sup>2</sup> (M = Na, K, ...) varies between 0 and 9.4 per nm<sup>2</sup>, depending on cleavage plane, synthesis method, and thermal treatment.<sup>120,249–252</sup> Q<sup>3</sup> silica surfaces with 4.7 SiO(H,M) groups per nm<sup>2</sup> are most common in glasses and nanoparticles at room temperature. At the same time, the amount of ionized sodium siloxide groups at pH 7.5 may still vary between 0.2 and 1.0 per nm<sup>2</sup>. The variation of the density of ionic groups across all conditions of surface chemistry and pH is as much as between 0.0 and 2.0 per nm<sup>2</sup> (Fig. 22).<sup>78</sup> The variability by multiples causes different types of interactions to govern specific adhesion of surfactants and biomolecules, as can be seen also from a top view onto representative silica surfaces (Fig. 23). Simulations have only recently begun to take surface ionization into account while prior models typically assumed

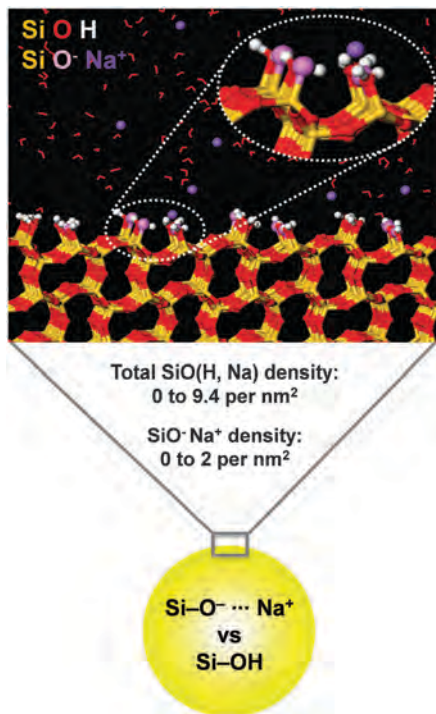


Fig. 22 Schematic of the surface structure of silica nanoparticles that includes silanol groups (SiOH) and a fraction of ionized groups such as sodium siloxide (SiONa). The presence of cations that can partly dissociate from the surface accounts for the observation of zeta potentials in the range of 0 to  $-40$  mV. The typical area density of silanol groups and ionized groups per unit area is indicated. Adapted and reproduced with permission from ref. 36.

neutral, or even non-stoichiometric silica surfaces covered by SiOH groups.<sup>22,45,89,93,94,127,253–261</sup> These models have limited applicability, and the inclusion of realistic surface chemistry opens up new opportunities for reliable computational predictions. A substantial amount of experimental literature since the 1950s has described the amount of ionized groups as a function of surface type, pH, ionic strength, and type of cation (M) using potentiometric titration and zeta potential measurements,<sup>120,249–252,262–268</sup> providing valuable resources for quantitative modeling and simulation.<sup>36,78</sup>

The adsorption of peptides is accordingly determined by ion pairing, hydrogen bonds, hydrophobic interaction, and changes in conformation (Fig. 24 and 25). These contributions to binding were identified by molecular simulation and comparisons to zeta potential measurements, IR and NMR spectroscopy, as well as adsorption isotherms for a series of different peptides.<sup>36,78,82,148</sup> The strongest adsorbing amino acids on negatively charged silica surfaces are protonated N termini, lysine (K), and arginine (R) residues, which neutralize (or even reverse) the zeta potential (Fig. 24a and 25a). Molecular simulations with the PCFF-INTERFACE and CHARMM-INTERFACE force field demonstrated that ammonium groups closely approach the silica surface and computed adsorption energies reach maximum negative values of  $-7$  kcal mol<sup>-1</sup> for 7-mer peptides and 12-mer peptides containing K and R.<sup>82</sup> Ion pairing is the dominant mechanism when the surface charge of silica is significant, *i.e.*, at pH ranges near seven and above.

At the same time, interfacial hydrogen bonds are possible. These involve oxygen and hydrogen atoms in silanol groups,

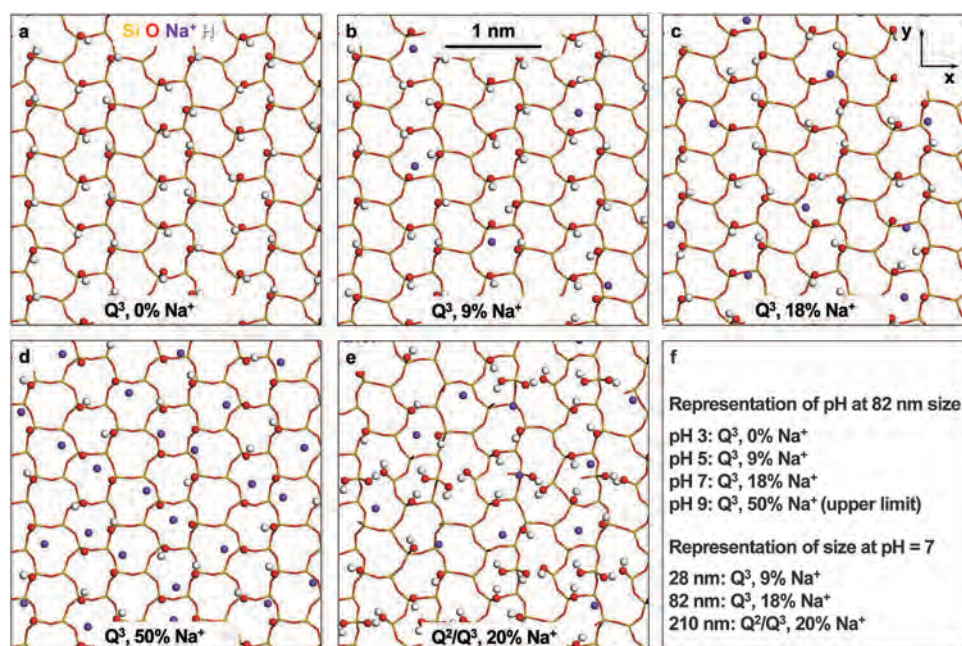
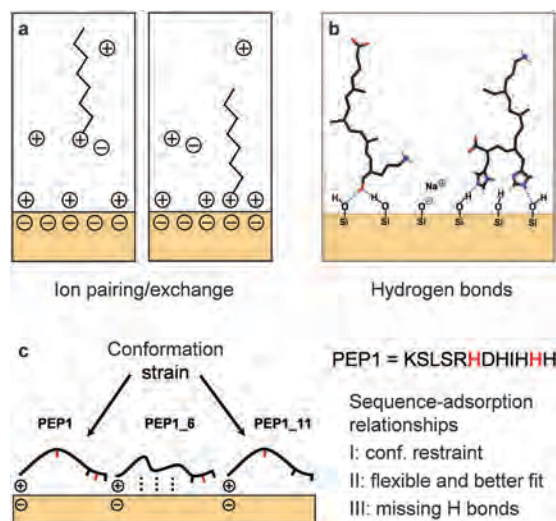


Fig. 23 Silica model surfaces for common surface chemistry as a function of pH and particle size in top view. Accordingly, water, organic, and biological molecules encounter different cation densities and surface environments leading to highly tunable adsorption. (a–d) Q<sup>3</sup> silica surfaces with 4.7 SiO(H,Na) groups per nm<sup>2</sup> represent typical silica glasses and particles of 50–100 nm size from Stober synthesis. Different amounts of SiO<sup>-</sup>Na<sup>+</sup> groups represent pH values of 3, 5, 7, and 9. (e) A Q<sup>2</sup>/Q<sup>3</sup> silica surface with 6.5 SiO(H,Na) groups per nm<sup>2</sup> and 20% ionization represents larger silica nanoparticles >100 nm size at pH 7. High area density of both SiOH and of SiO<sup>-</sup>Na<sup>+</sup> groups results in stronger adsorption of most peptides by ion pairing and hydrogen bonds. (f) Approximate correspondence of the models to pH and particle size near physiological ionic strength according to details in ref. 78 and in ref. 82. Reproduced with permission from ref. 82.



**Fig. 24** Main contributions to adsorption of peptides on silica surfaces. (a) Ion pairing and ion exchange, (b) hydrogen bonds, (c) conformation effects. Conformation analysis for three mutant 12-peptides of the native peptide Pep1 on silica surfaces in molecular simulation shows that individual residues such as H6 may cause conformation strain that is relieved upon mutation to A6 in Pep1<sub>6</sub>. Other residues such as H11 can be essential for binding through protonation and hydrogen bonds, which is diminished upon mutation to A11 in Pep1<sub>11</sub>. Attraction of hydrophobic groups to the surface also contributes to adsorption at low surface ionization by fostering a continuous water structure. Adapted and reproduced with permission from ref. 36.

siloxide ions, and lattice oxygen atoms on the silica surface in contact with alcohol groups (T,S), backbone amide groups, and aromatic heterocycles (H,W) in peptides (Fig. 24b). Hydrogen bonds play a dominant role near the point of zero charge of silica ( $\sim$ pH 3) for all peptides. Peptides that contain suitable groups and possess no cationic groups can be primarily attracted to the silica surface through hydrogen bonds at any pH. In addition, it has been observed in simulations and in adsorption isotherms that peptides containing hydrophobic groups are also attracted to silica. Residues such as F, W, L, I, V can be effectively attracted to silica surfaces at lower pH, as well as to silica surfaces of lower area density of silanol groups ( $Q^3/Q^4$ ). These hydrophobic interactions are the result of depletion forces, *i.e.*, adsorption on the surface prevents the disruption of hydrogen bonds in the aqueous phase that would occur when the hydrophobic residues remain immersed.<sup>82,248</sup> Thus, there is no intrinsic attraction of these groups to silica, and the driving force is rather the exclusion from water on less ionized silica surfaces.<sup>82</sup> On increasingly ionized silica substrates, hydrophobic groups do not approach the surface because they would disrupt the hydration shells of siloxide ions and of cations close to the surface.

Another contribution to adsorption arises from conformation preferences of the peptides (Fig. 24c and 25a).<sup>36</sup> Conformation effects are particularly important for longer chain molecules and play a role on all surfaces, metals or oxides alike. Yet, conformation effects play a proportionally bigger role on oxide surfaces compared to metals as binding energies tend to be of smaller negative values (less attractive), giving more importance to entropic contributions. Simulation results have indicated the

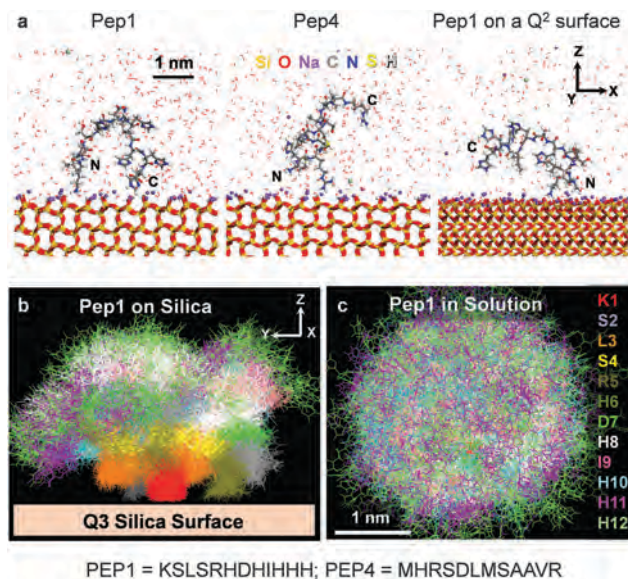


**Fig. 25** Representative snapshots and superposition of peptides adsorbed on silica surfaces and in solution. (a) Peptides pep1 and pep4 adsorbed on  $Q^3$  silica surfaces ( $4.7 \text{ SiO}$ , Na groups per  $\text{nm}^2$ ) as well as on a  $Q^2$  silica surface [ $9.4 \text{ Si}(\text{O},\text{Na})$  groups per  $\text{nm}^2$ ] with high ionization. The position of N and C termini is indicated. (b) Superposition of over 10 000 peptide conformations during 20 ns simulation time in equilibrium on the  $Q^3$  silica surface. The color code indicates the spatial distribution of amino acid residues, translated laterally to the same coordinate of K1. (c) Superposition of peptide structures in solution showing the isotropic orientation. Adapted from ref. 36.

dynamic nature of the interfaces in which the peptides move on and off the silica surface, effectively spending a certain fraction of time in close contact with the surface ( $< 3 \text{ \AA}$ ). In case of ion pair formation, the time in close contact can be over 90% although it may only involve the N terminus or the lysine side chain. Other parts of the peptide are often quite detached from the surface for most of the time. A dynamic average that represents the superposition of many thousand equilibrium structures is shown in Fig. 25b for the peptide Pep1, which binds to particles of 82 nm size from Stober synthesis in experiment.<sup>36</sup> In the absence of ion pairing, the time in close contact with the surface by hydrogen bonds is only in the range 30–70% and may often involve hydrophobic interactions as well. Residue-specific metrics can be derived from molecular simulation and the difference to isotropic orientation of the peptides in solution can be clearly seen (Fig. 25b).<sup>36,82</sup>

Specific mutations in a peptide can also cause significant changes in conformation and binding. Such effects were investigated in detail for the mutation of H to A in the 6 and 11 positions in Pep1 (KLSLRHDHIIHH).<sup>36</sup> The native peptide exhibits a bent conformation related to a certain stiffness in the middle of the backbone. In the mutation Pep1<sub>6</sub>, in which H6 is replaced by A6, the stiffness is reduced and the binding strength increases in simulation and in adsorption isotherms due to more hydrogen bonds with the surface throughout the backbone (Fig. 24c). In the mutation Pep1<sub>11</sub>, by replacement of H11 by A11, the higher stiffness of Pep1 is retained and the possibility of hydrogen

bonding of H11 to the silica surface is eliminated, as well as the opportunity of H11 to accept protons and to form ion pairs with siloxide groups. Binding of Pep1\_11 is then weaker according to both measurement and molecular dynamics simulation.

Using pH resolved surface models for silica on the basis of available experimental data (Fig. 23),<sup>78</sup> it has become possible to predict peptide adsorption very specifically as a function of surface structure, peptide sequence, and pH value (Fig. 26).<sup>82</sup> Quantitative predictions of binding constants for silica–organic interfaces hold tremendous promise for the rational design of new catalyst supports, drug delivery vehicles, porous glasses for gas separations, biomarkers, mineralization studies, organic coatings, and nanocomposites with tailored properties.

*Ab initio* studies have also been employed to study the binding of drug molecules to silica surfaces, although yet without solvent (Fig. 27).<sup>253,269</sup> Density functional theory (DFT) methods are often limited to studies in vacuum and mostly suited to explore reactive processes on a local scale (see Section 2). The inclusion of realistic surface geometries and solution conditions for routine computational screening of binding and release of surface bound molecules is difficult and computationally very expensive. Problems to reproduce London dispersion forces have also been noted.<sup>253</sup> The INTERFACE force field overcomes such limitations through reproduction of surface and interfacial energies in <5% deviation from experiment, down from common errors exceeding 50% in DFT methods and in incompletely validated force fields.<sup>78</sup>

Titania surfaces exhibit ionization of superficial Ti–OH groups similar to silica and have shown closely related mechanisms of molecular recognition and binding.<sup>45,270–273</sup> Steered MD simulations indicated binding free energies of the peptide RKLPGA on a negatively charged titania surface (pH ~ 7) to be on the order of  $-40 \text{ kJ mol}^{-1}$  ( $-9.5 \text{ kcal mol}^{-1}$ ) (Fig. 28).<sup>45</sup> The titania surface model assumes effectively 0.76 negatively charged  $\text{TiO}^-$  groups per  $\text{nm}^2$  ( $-0.123 \text{ C m}^{-2}$ ) and the dominant binding mechanism is then ion pairing of the  $\text{TiO}^-$  groups with the positively charged R and K residues in the peptide (Fig. 24a). The importance of the cationic R and K residues in the RKLPGA

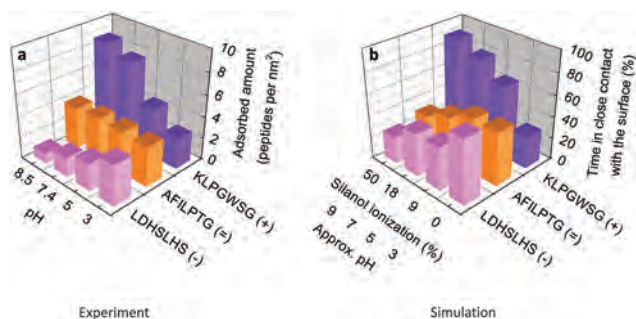


Fig. 26 Peptide adsorption on silica nanoparticles of average diameter 82 nm with 4.7 silanol groups per  $\text{nm}^2$  as a function of pH by measurement and simulation. (a) Adsorbed amount of three peptides of different charge as a function of pH at 1 mM initial concentration (from ref. 248). (b) Percentage of time the same peptides spend in close contact with  $\text{Q}^3$  silica surfaces of different ionization according to simulation ( $< 3 \text{ \AA}$ ). Different pH states of the surface are embodied in the model by differences in silanol ionization. Reproduced with permission from ref. 82.

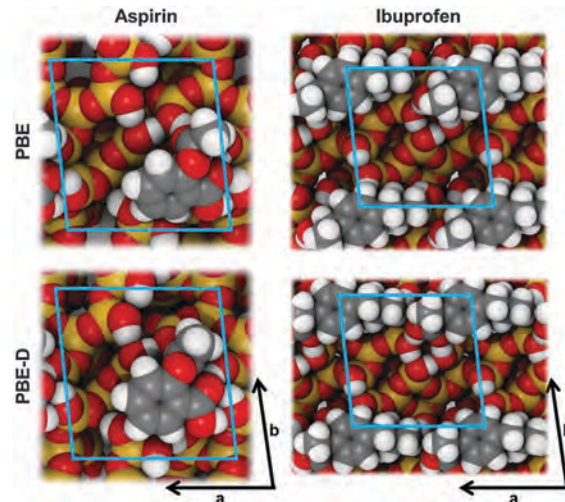


Fig. 27 3D top views of space filling models of the adsorption geometries of aspirin and ibuprofen on the 4.5 OH per  $\text{nm}^2$  silica surface ( $\text{Q}^3$  surface without ionization) using DFT calculations with PBE and PBE-D functionals in vacuum. Borders of the unit cell are shown in light blue. Reproduced with permission from ref. 253.

peptide for strong binding was also shown *via* AFM measurements in comparison to weaker binding of RKLPGA peptide mutants where these residues were replaced by other amino acids.<sup>274,275</sup> The binding free energy of peptide RKLPGA to titania is similar to that of comparable silica-binding cationic peptides at pH ~ 7, for example, a binding free energy of  $-6 \text{ kcal mol}^{-1}$  was reported for KPLGWSG on silica (Fig. 26).<sup>82</sup> The point of zero charge is pH ~ 5.5 for titania compared to pH ~ 3 for silica, rendering the titania surface somewhat less acidic than typical  $\text{Q}^3$  silica surfaces. Comprehensive pH resolved surface models for titania surfaces have not yet become available.

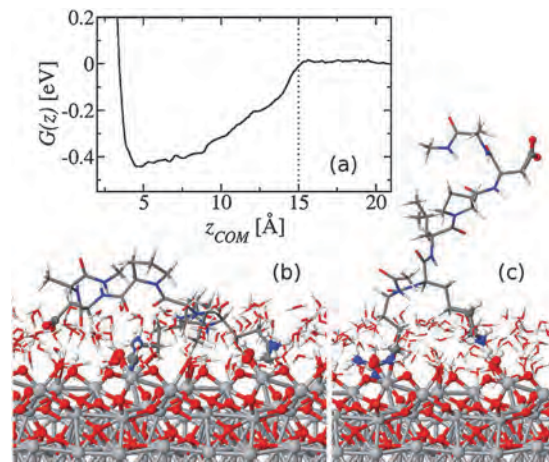


Fig. 28 Interactions of the peptide RKLPGA with a titania surface terminated by Ti–OH groups and  $\text{Ti–O}^-$  groups near pH 7 in molecular dynamics simulations. (a) Free energy profile of the RKLPGA peptide on an oxidized titanium surface obtained by metadynamics and replica exchange with solution tempering (REST). (b and c) Typical adsorbed peptide structures include flat as well as upright conformation with R and K residues bound to the surface. Reproduced with permission from ref. 45.

Apatite minerals, common in bone and teeth, have similarly adaptive surface properties.<sup>6,218,276</sup> The surface is pH sensitive and superficial phosphate ions are protonated between mono-hydrogen phosphate and dihydrogen phosphate under physiological conditions (Fig. 29).<sup>277</sup> These important aspects have only been recently taken into account in molecular simulations so that reliable simulations of specific binding of peptides and polymers are just about to emerge.<sup>11,148,277</sup> Prior simulation studies often assume bare phosphate surfaces corresponding to pH values above 14 that lead to immediate cell death.<sup>278–280</sup> Carefully designed surface models and validated force fields allow specific and accurate analyses of the interfacial properties of apatites as a function of pH, including the reproduction of hydration energies and peptide specificity. The INTERFACE force field includes a surface model database with pH resolved surface models that can be used and further customized for predictive simulations.<sup>11</sup> The game-changing impact of solution conditions and their representation in models towards computed surface energies, hydration energies, and specific peptide recognition is illustrated in Fig. 30.<sup>277</sup> The CHARMM-INTERFACE

force field and the PCFF-INTERFACE force field reproduce the cleavage energy of neat hydroxyapatite, which is approximately  $1100 \text{ mJ m}^{-2}$  for the common prismatic (010) crystal plane.<sup>122</sup> Upon protonation, the agglomeration energy decreases to 640 and  $320 \text{ mJ m}^{-2}$  at pH 10 and pH 5, respectively, related to leaching of calcium hydroxide and a resulting lower cation density on the hydrogenphosphate and dihydrogen phosphate terminated surface.<sup>281–285</sup> Similarly, the immersion energy in water depends strongly on pH. Neat apatite surfaces react immediately with water, and the hydration energies at pH 10 and pH 5 are about 800 and  $620 \text{ mJ m}^{-2}$ , respectively (Fig. 30). The values agree with hydration energies measured in experiment in the range of 600 to  $700 \text{ mJ m}^{-2}$ .<sup>286,287</sup> First studies of the binding of peptides found adsorption responses that are similarly sensitive to the surface environment as seen for silica. The peptide SVSVGGK, selected by phage display,<sup>232</sup> adsorbs mainly through ionic groups at higher pH and *via* different, less ionic groups (S,V) at lower pH (Fig. 30). The computed binding energy of  $-5$  and  $-9 \text{ kcal mol}^{-1}$ , respectively, is in very good agreement with the experimental binding free energy of  $-6 \text{ kcal mol}^{-1}$  ( $K_D = 5.4 \times 10^{-5} \text{ M}$ ) on a polycrystalline HAP substrate.<sup>232</sup> Simulations using appropriate surface models, which may eventually be integrated into databases, and force fields facilitate quantitative predictions and easy access to length scales up to 100 nm at a million times lower cost than *ab initio* and DFT approaches. Future applications of such techniques include the analysis of bone and dentin mineralization in extracellular environments, of the action of drug molecules against osteoporosis, and of the formation of atherosclerotic deposits in comparison with laboratory and clinical tests. Arterial deposits also include calcium oxalates which can be modeled using similar approaches.<sup>103,237,288</sup>

Several computational and experimental studies have been dedicated to calcium carbonate in aqueous solution,<sup>289,290</sup>

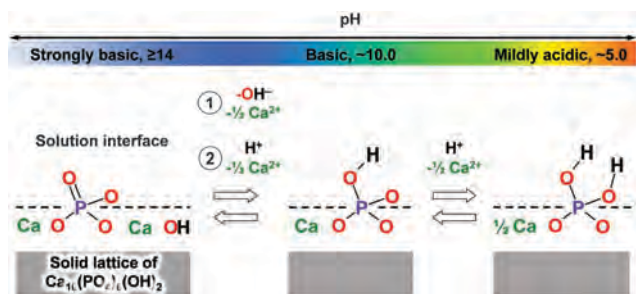


Fig. 29 Termination of hydroxyapatite surfaces at different pH values (adapted with permission from ref. 277).

pH	15	10	5
Cleavage energy	(010) comp 1080 $\text{mJ/m}^2$ expt 1000-1200	640 $\text{mJ/m}^2$ 350-500	320 $\text{mJ/m}^2$
Immersion energy in water	(010) reactive	$E_{\text{imm}} \sim 800 \text{ mJ/m}^2$ 600-700	$E_{\text{imm}} \sim 620 \text{ mJ/m}^2$
Adsorption of peptide SVSVGGK	• $\text{NH}_3^+$ at K7 • C-term. $E_b \sim -4.7 \text{ kcal/mol}$	(010) • S1, S3 • V2, V4 $E_b \sim -9.0 \text{ kcal/mol}$	(010)

Fig. 30 Major differences in surface properties of hydroxyapatite as a function of pH according to simulation with the CHARMM-INTERFACE force field (numbers in black) and experiment (numbers in blue). The cleavage energy is drastically reduced towards lower pH values, and also the immersion energy in water decreases. Simulations also show a reversal in binding mechanism of peptides to apatite surfaces. At pH 10, adsorption of the peptide SVSVGGK on the (010) prismatic plane is mediated by ionic groups and comparatively weak. At pH 5, the polar and hydrophobic motif SVSV is more attracted and the peptide binds notably stronger.

interactions with organic molecules,<sup>104</sup> self-assembled monolayers,<sup>238,291,292</sup> as well as polyelectrolytes.<sup>237</sup> The  $pK$  values of carbonic acid are  $pK_1 = 6.35$  and  $pK_2 = 10.33$ <sup>125</sup> and indicate that, under mineralization conditions of pH 8 to 10, the majority of carbonic species in solution are hydrogen carbonate ions ( $\text{HCO}_3^-$ ) and only small amounts of carbonate ions ( $\text{CO}_3^{2-}$ ).<sup>293</sup> However, similar to simulation studies of apatites, prior computations have almost exclusively focused on carbonate terminated surfaces ( $\text{CO}_3^{2-}$ )<sup>104,294,295</sup> which are only likely to be present at pH values higher than 11. Suitable pH resolved atomistic surface models for calcite still need to be developed and validated to achieve mechanistic understanding and predictions of biological assembly in consistency with experiment. At typical pH values between 8 and 10 near the point of zero charge, the surfaces of the  $\text{CaCO}_3$  polymorphs calcite, aragonite, and vaterite are likely covered with hydrogen carbonate while the interior mineral core consists of calcium carbonate. Realistic surface models may involve, for example, 90/10 termination by  $\text{HCO}_3^-$  and  $\text{CO}_3^{2-}$  at pH  $\sim 9$ , 50/50 termination by  $\text{HCO}_3^-$  and  $\text{CO}_3^{2-}$  at pH  $\sim 10.5$ , and 10/90 termination with  $\text{HCO}_3^-$  and  $\text{CO}_3^{2-}$  at pH  $\sim 11.5$ . Mineralization near pH 9 likely involves the crystallization of hydrogen carbonate into carbonate under consumption of hydroxide ions and formation of water; or disproportionation of  $\text{HCO}_3^-$  ions into  $\text{CO}_3^{2-}$  and  $\text{H}_2\text{CO}_3$ . Extensive experimental studies have described calcite nucleation and growth<sup>41,236,293,296–298</sup> and provide valuable input for realistic simulations.

Adsorption of organic molecules has also been studied on several other nanostructures using quantum mechanical methods, including energy minimization and *ab initio* MD. An example is the adsorption of catechol (*o*-dihydroxybenzene) on SiC, GaN, ZnO, CdS, and CdSe surfaces (Fig. 31).<sup>242,299</sup> Validated force fields are not yet available for many of these compounds so that quantum mechanical calculations of adsorption in the gas phase have been reported as a first approximation. Further force field developments will eventually allow insight into assembly at length scales up to 100 nm under realistic solution conditions.

#### 4.2. Applications to understand the formation of biominerals, drug delivery, and processes in solar devices

The formation of silica, phosphates, carbonates, and other minerals from soluble precursors is a complex process that involves specific chemistry, protonation–deprotonation equilibria, and hydration–dehydration equilibria. The examples of mineralization in nature such as diatoms, mollusks, nacre, bone, teeth, and marine calcite skeletons are fascinating and still incompletely understood today.<sup>112,114,217,236,300,301</sup> Therefore, modifications of the mechanisms to customize such materials is also a major challenge. To-date, template approaches for mineral synthesis starting with pre-assembled surfactants have been successfully used in laboratory synthesis.<sup>302–305</sup> A selection of promising experimental findings and first computational studies related to mineral formation are presented in the following to illustrate opportunities for computational studies to elucidate mechanistic understanding and accelerate the development of functional materials.

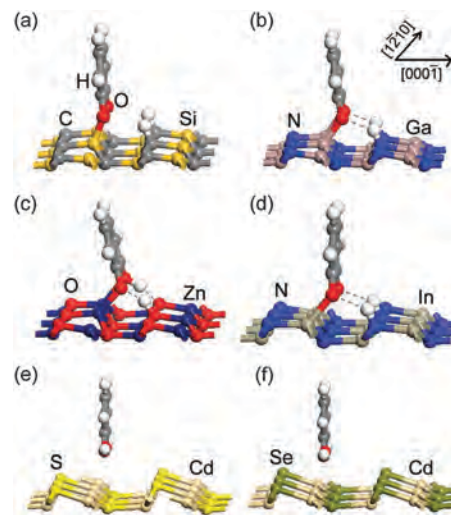


Fig. 31 Adsorption configurations of catechol molecules on wurtzite ( $10\bar{1}0$ ) surfaces in vacuum by DFT (PBE-GGA): (a) SiC, (b) GaN, (c) ZnO, (d) InN, (e) CdS, and (f) CdSe. Dashed lines identify molecule–substrate H bonds. Reproduced with permission from ref. 299.

Computational studies of interactions between ionic apatite precursors and bone sialoprotein have been reported (Fig. 32).<sup>47</sup> Bone sialoprotein is a highly phosphorylated, acidic, noncollagenous protein in the bone matrix and considered to be a nucleator of hydroxyapatite (Fig. 29 and 30). The interaction of a phosphorylated, acidic, 10 amino-acid model peptide sequence with  $\text{Ca}^{2+}$  ions and hydrogenphosphate ions was investigated by molecular dynamics simulation to understand the distribution and development of potential crystal nuclei in solution. The results show that the  $\alpha$ -helical and random coil conformations of the peptide support the formation of a  $\text{Ca}^{2+}$  equilateral triangle around the surface of the peptide, which resembles the distribution of calcium ions on the (001) face of hydroxyapatite crystals. However, the formation of a stable nucleating template could not be consistently observed. The bone sialoprotein nucleating motif may therefore be more likely to help nucleate an amorphous calcium phosphate cluster, which ultimately converts to crystalline hydroxyapatite. Mineralization mechanisms may be investigated in more detail using models of nanocrystals and phosphate species at specific pH conditions and variable concentration of peptides.

*In situ* experimental measurements by liquid phase *in situ* transmission electron microscopy (TEM) and AFM have recently suggested a mechanism for the nucleation of calcium carbonate in a matrix of polystyrene sulfonate (PSS) in solution (Fig. 33).<sup>236</sup> The developing mineral interacts with the matrix-immobilized acidic macromolecules, and time-resolved data have been able to track the mechanism in a resolution close to one nanometer. The binding of calcium ions to form Ca–PSS globules was identified as a key step in the formation of metastable amorphous calcium carbonate (ACC) that has been identified as an important precursor phase in many biomineralization systems.<sup>234,238,240,292,296</sup> The findings demonstrate that ion binding can play a significant role in directing nucleation, independently of any control over

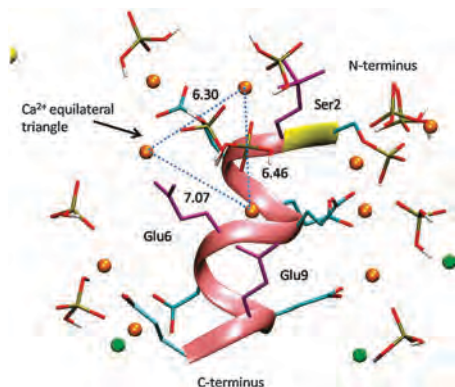


Fig. 32 A snapshot illustrates the interactions among  $\text{Ca}^{2+}$  ions, hydroxophosphate ions, and the glutamic-acid rich peptide domains in molecular dynamics simulations (SpSpEEEEEEEE). Distances are indicated in Angstroms. Reproduced with permission from ref. 47.

the free-energy barrier to nucleation. The *in situ* techniques provide detailed insight that could be further resolved and tested using simulations in atomic resolution. The mechanism is similar to adatom deposition (path 2, Fig. 19), with ions rather than atoms.

*In situ* experimental observations also provided footage of a cluster attachment process for iron oxide hydroxide nanoparticles of the approximate composition  $5\text{Fe}_2\text{O}_3 \cdot 9\text{H}_2\text{O}$  (Fig. 34). This process is similar to cluster attachment of metal nuclei (path 1, Fig. 19). Twin formation occurs once small clusters attach in various orientation to another particle and find a favorable fit (Fig. 34a–g).<sup>190</sup> High-resolution transmission electron microscopy using a fluid cell showed that finally a sudden jump over less than 1 nanometer fused the clusters together, followed by lateral atom-by-atom addition initiated at the contact point. Interface elimination was observed at a rate consistent with the curvature dependence of the Gibbs free energy. The observations are also consistent with the typical range of Coulomb and van der Waals interaction of overall electroneutral mineral surfaces that has been identified by molecular simulations on silicate, aluminate, and clay minerals.<sup>79,80,84</sup> Over 95% of surface attraction is typically lost after more than 1 nm separation and strong surface interactions require  $<0.5$  nm distance, relatively independent of specific surface chemistry.

In Section 4.1, we have shown that binding constants of peptides onto silica and apatite surfaces can be predicted in quantitative agreement with experiment.<sup>82,148,253</sup> These methods can be applied to computational screening of the binding of drug molecules to inorganic surfaces and their release from nanostructures under realistic solution conditions. For example, the loading of drugs to and release from porous silica nanoparticles may be investigated as a function of particle surface chemistry, pH, and temperature to explain experimental data and make predictions for specific systems.<sup>7</sup> Also, the binding of bisphosphonate osteoporosis drugs to apatite nanocrystals is not well understood in experiment and would benefit from simulations.<sup>277,306–308</sup> Prior force-field based computational screening studies suffered from unrealistic apatite surface models (pH  $> 14$ )<sup>309,310</sup> and the absence of solvents due to limitations of

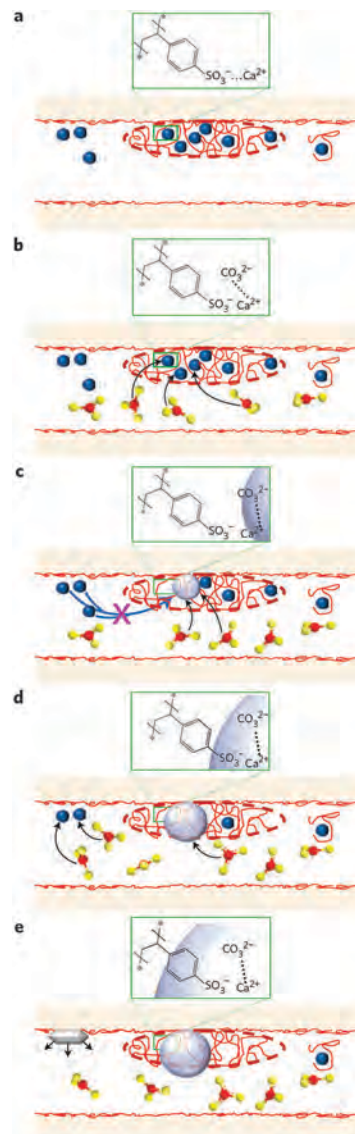
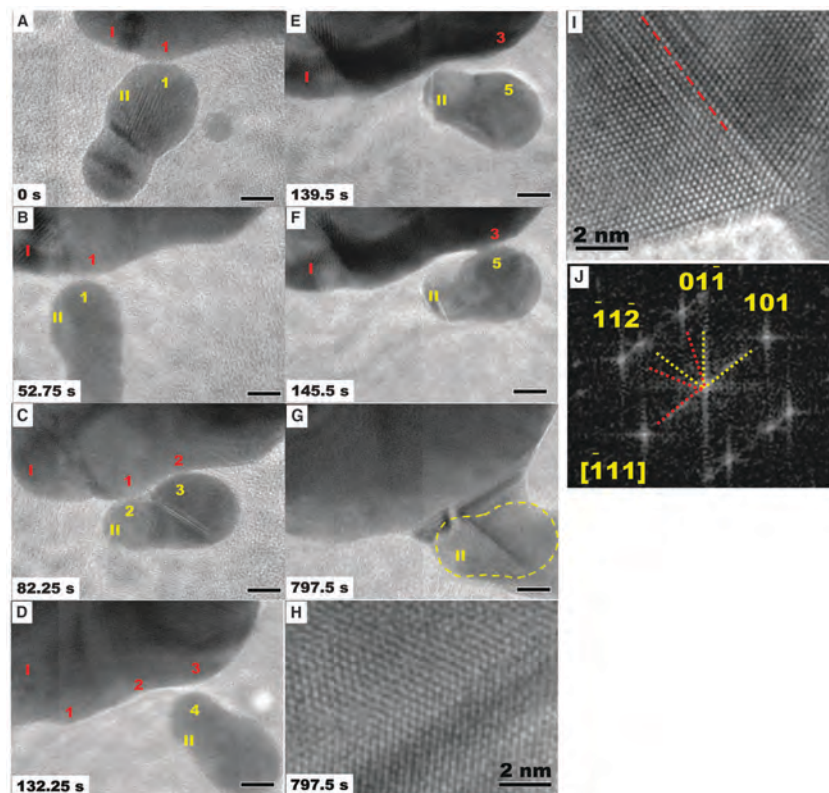


Fig. 33 Mechanism of  $\text{CaCO}_3$  mineral formation in a biomimetic polystyrene sulfonate matrix (PSS) according to liquid phase *in situ* TEM (ref. 236). (a) Initially,  $\text{Ca}^{2+}$  ions (blue dots) bind with the  $\text{SO}_3^-$  group of the PSS (red), as indicated in molecular detail in the green box, leading to a locally high  $\text{Ca}^{2+}$  concentration in the Ca–PSS globules deposited on the surface of a  $\text{Si}_3\text{N}_4$  substrate (orange) and to low free  $\text{Ca}^{2+}$  concentration in the surrounding solution, where it binds to dissolved PSS. (b)  $\text{CO}_3^{2-}$  (or  $\text{HCO}_3^-$ ) ions (red and yellow dots) from an ammonium carbonate source then diffuse into the globules (black arrows), where they bind with  $\text{Ca}^{2+}$  ions, replacing the weaker  $\text{SO}_3^-/\text{Ca}^{2+}$  interaction and creating a supersaturated state. (c) At a critical value of supersaturation (after  $\sim 20$  min), amorphous calcium carbonate nuclei (light blue sphere) appear and grow as a result of the continued generation of  $\text{CO}_3^{2-}$  (or  $\text{HCO}_3^-$ ) ions. However, free  $\text{Ca}^{2+}$  ions do not diffuse into the globules (blue arrows with pink cross) owing to the low  $\text{Ca}^{2+}$  concentration in solution compared with that in the globules, which is fixed by the solubility of amorphous calcium carbonate (ACC). (d) The growth of ACC stops when the supply of excess  $\text{Ca}^{2+}$  ions in the globules is depleted, but the continuous generation of  $\text{CO}_3^{2-}$  (or  $\text{HCO}_3^-$ ) ions eventually raises the supersaturation of the solution to the level required for vaterite nucleation on the  $\text{Si}_3\text{N}_4$  substrate. (e) Vaterite continues to grow until the remaining free  $\text{Ca}^{2+}$  ions are depleted. (Reproduced with permission from ref. 236).



**Fig. 34** Oriented attachment of iron oxide hydroxide nanoparticles in solution. (a–g) Sequence of TEM images showing the typical dynamics of oriented attachment. The surfaces of particles I and II made transient contact at many points and orientations (points 1–1, 1–2, 2–3, and 3–4) before finally attaching and growing together (points 3–5). (h) High-resolution image of interface in (g) showing twin structure (an inclined twin plane). The yellow dashed line in (g) shows the original boundary of the attached particle. (i and j) High-resolution *in situ* TEM image (i) and fast Fourier transform (FFT) (j) of an interface from another oriented attachment event demonstrating formation of a (101) twin interface after attachment. The grain boundary is delineated by a dashed line in (i). Scale bars are 5 nm for (a) to (g). Adapted and reproduced with permission from ref. 190.

DFT computational methods.<sup>279,280</sup> The use of chemically realistic force fields and surface models will make simulations much more useful (Fig. 29 and 30). Drug delivery has also been suggested using clay minerals such as montmorillonite as a carrier material.<sup>311</sup> Adsorption/desorption equilibria can then be monitored using the CHARMM-INTERFACE force field<sup>11</sup> or CLAYFF.<sup>90</sup>

Mineral–organic interfaces also play a major role in solar devices.<sup>312–316</sup> The interface between oxides or quantum dots with conductive polymers determines polaron dynamics, charge transfer, and ultimately affects the power conversion efficiency.<sup>317</sup> Molecular dynamics simulations can help visualize the morphology development beyond the 10 nm scale. Charge separation and exciton dynamics can subsequently be followed locally from first principles simulations (Fig. 35).<sup>318</sup> It is believed that the charge transfer excitons (CT1, CT2, CT3) rather than the intramolecular excitons (M1, M2, M3) play crucial roles in the photovoltaic performance as both photocurrent and open circuit voltage depend on them. For the poly-3-hexylthiophene/zinc oxide junction, the averaged energy of the three possible charge transfer excitons after *ab initio* molecular dynamics simulation is 1.7, 2.0, and 2.3 eV. These values are in good agreement with measurements from photoinduced absorption spectroscopy of 1.9 to 2.5 eV.<sup>318</sup>

Often the band structure is important to decide upon suitability of a quantum dot for a photovoltaic device, luminescent device, or

electronic sensor. Understanding the interaction of nanoparticles with stabilizing surfactants can then be critical. NMR spectroscopy and IR spectroscopy are helpful to probe the composition and surface chemistry, as shown for the example of an indium phosphide quantum dot (Fig. 36).<sup>319</sup> The combination of techniques allowed the identification of binding modes of carboxylate surfactants to an InP surface. Molecular simulations, once appropriate force fields are derived, can then determine equilibrium conformations, binding energies, and electronic properties in combination with *ab initio* methods. Oxide and mineral surfaces are often also catalytically active, which provides opportunities for multiscale simulations to predict both charge transfer and reactivity under given conditions.<sup>320,321</sup> Thin films of biological or organic molecules on oxide surfaces also find applications in bioadhesives.<sup>322</sup>

## 5. Inorganic–organic interfaces in polymer composites and building materials

The performance of polymer nanocomposites, hydrogels, and building materials also depends on specific inorganic–organic interactions.<sup>228,242,323–330</sup> The presence of clay, silica, cement minerals,

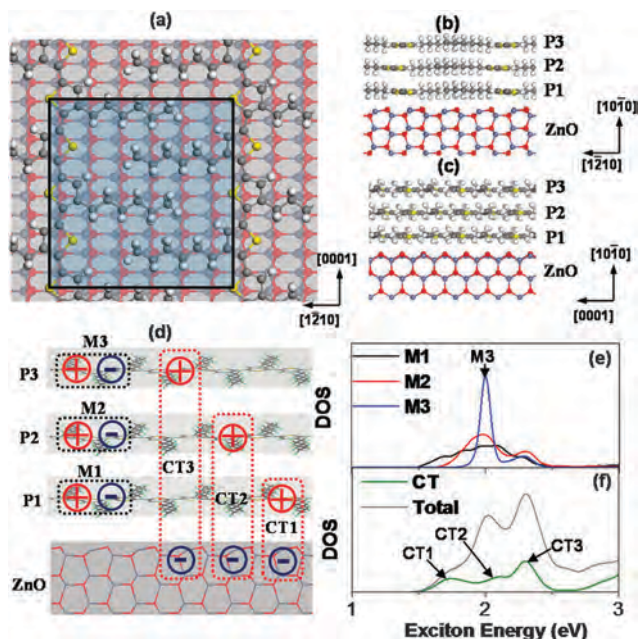


Fig. 35 (a) Top and (b and c) side view of a poly-3-hexylthiophene (P3HT)/ZnO interfacial atomic structure. (d) Schematics of excitons studied including intramolecular (M1, M2, M3) and charge transfer (CT1, CT2, CT3) excitons. (e and f) The exciton density of states (DOS) of P3HT/ZnO with the ground state energy set to 0. The blue, red, gray, yellow, and white spheres in panels a–c represent Zn, O, C, S, and H atoms, respectively. Reproduced with permission from ref. 318.

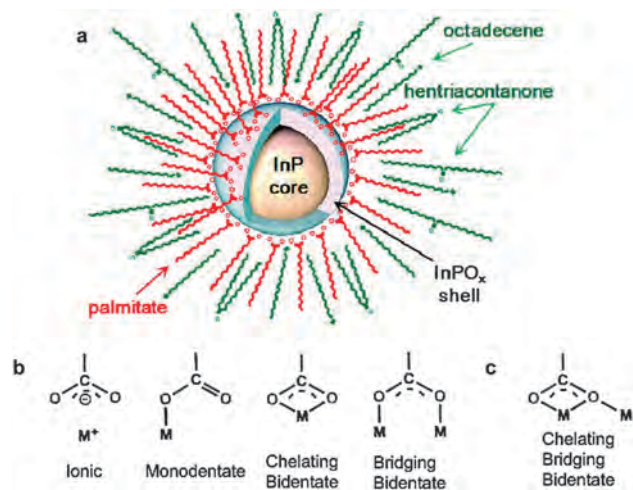


Fig. 36 (a) Graphical schematic representation of InP quantum dots isolated using synthesis and purification. (b) Basic carboxylate binding modes and (c) additional carboxylate binding mode observed in indium carboxylate complexes according to multidimensional NMR and IR studies. Reproduced with permission from ref. 319.

or graphitic nanostructures within a polymer matrix introduces changes in morphology and material properties related to the presence of ionic surfaces, interfacial interactions, and interfacial reconstruction.<sup>80,326,331,332</sup> Polymer–inorganic nanocomposites, for example, find applications in structural materials, capacitors, batteries, and sensors.<sup>333</sup> Property predictions have

been aided by simulations and this section describes modeling of inorganic–organic interfaces in such nanocomposites, organically modified clay minerals, and cement materials in comparison to measurements.

### 5.1. Polymer nanocomposites and modified clay minerals

A major challenge for performance improvements of composite materials is often the uniform dispersion of filler materials such as clay platelets, carbon nanotubes, silica nanoparticles, or metal flakes.<sup>334–336</sup> Computer simulations using atomistic and coarse-grained models recently allow following the kinetics of exfoliation of clay layers in a polymer matrix (Fig. 37). For polymer melts, blending, compounding, and extrusion are typically necessary to overcome barriers towards polymer intercalation into mineral layers and exfoliation/dispersion of the filler platelets, tubes, or particles, which is severely hindered at long chain lengths ( $>10^3$  monomers) due to folding and long relaxation times. Other factors that affect the exfoliation of nanofillers are also the interactions between the layers or particles themselves (Fig. 38). In order to exfoliate the layers of a filler material such as graphene or clay, the interactions between the layers must be overcome, void spaces in the polymer matrix for the new positions of the individual layers must be created, and then the two materials regain some of the required free energy by forming the mineral–polymer interface (MP) (Fig. 38a).<sup>88</sup> The process requires many conformational transitions of the polymer. Unless it occurs in solution with easy relaxation in a good solvent, it may never complete even during extrusion at high temperatures for extended periods of time.<sup>228</sup> However, if the cohesion between the mineral layers is very strong, such as between layers of unmodified clay minerals, it may be impossible to ever complete. Organic surface modification can reverse the strong surface polarity of clay minerals and lead to a range of tunable cleavage energies (Fig. 38b).

Typical clay minerals like montmorillonite, veegum, as well as muscovite mica contain variable amounts of dissociable cations on the surfaces of the nanometer-thick layers, for example, sodium ions in a typical montmorillonite  $\text{Na}_{0.33}[\text{Si}_4\text{O}_{10}][\text{Al}_{1.67}\text{Mg}_{0.33}\text{O}_2(\text{OH})_2]$  with a cation exchange capacity of  $\sim 90$  meq/100 g.<sup>68,331</sup> The extended basal (001) surfaces are not subject to protonation–deprotonation equilibria, pore formation, and dissolution in contrast to silica and apatites. Therefore, layered silicates often serve as model substrates to study surface forces and self-assembly processes. Systematic experimental and computational studies have shown the influence of the area density of cations and of the type of cations on swelling, ion exchange, adsorption of organic molecules, and assembly of surface-grafted surfactants.<sup>18,337–341</sup> Ion exchange of surface cations by alkylammonium and alkylphosphonium surfactants reverses the polarity from hydrophilic to hydrophobic and enables better miscibility with nonpolar solvents and polymer matrices in packaging materials, automotive and aerospace parts, commodity plastics, and coatings (Fig. 39).<sup>18</sup> The exchange of surface cations such as sodium or lithium for alkylammonium ions may occur spontaneously or require prior exfoliation of the nanometer-thick clay mineral layers at high temperature in

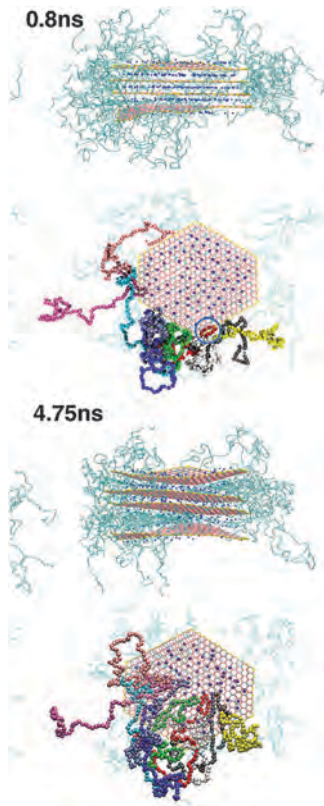


**Fig. 37** Intercalation of “long” polyvinylalcohol (PVA) chains into a selected clay tactoid using coarse-grain representations of clay layers and polymer. The side and top views of the tactoid are shown for simulation times of 0.8 ns and 4.75 ns. For each timeframe, the side view illustrates the bending that the lowermost clay sheet undergoes to accommodate the intercalating PVA polymer molecules. In the top view, the polymers that intercalate into the spacing between the lowermost sheets are colored according to their molecule number, such that they can be differentiated during visualization. It is observed that the polymer initially intercalates as short loops (an example is circled in blue at the 0.8 ns snapshot), and then progresses further into the interlayer to form a relatively linear chain on the clay surface. Reproduced with permission from ref. 334.

solution.<sup>342</sup> The surfactants enter the galleries and arrange as homogeneous molecular layers or as islands, depending on the chain length, packing density, and stoichiometric amount (Fig. 39).<sup>332</sup> The intercalated amount can be often determined by an increase in the gallery spacing  $d$  using X-ray measurements and in comparison to results from molecular simulation.

At stoichiometric ion exchange, the arrangement of surfactants on the individual even surfaces depends on the packing density  $\lambda_0$ , which is defined as the ratio of the cross-sectional area of a surfactant chain  $A_{C,0}$  to the available surface area per cationic site  $A_S$ :<sup>137</sup>

$$\lambda_0 = \frac{A_{C,0}}{A_S}. \quad (2)$$

The packing density also equals the cosine of the segmental tilt angle of the grafted surfactants and determines the occurrence of reversible melting transitions of flexible surfactants, *e.g.* alkyl chains, upon heating (Fig. 40). The surface-attached alkyl

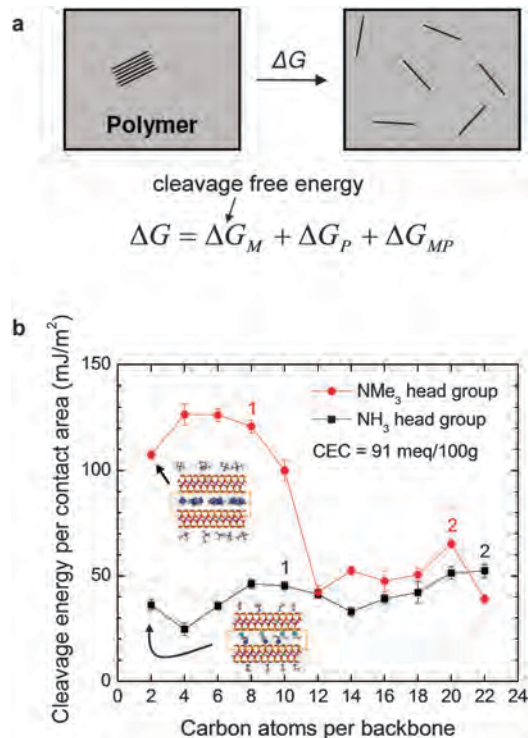


**Fig. 38** Thermodynamic model for exfoliation of fillers in polymer matrices and computed cleavage energy of organically modified montmorillonite. (a) A thermodynamic model for the free energy of exfoliation  $\Delta G$  of mineral layers in a polymer matrix. The cleavage energy of the filler lamellae is easier to adjust by choice of specific surfactants than changing the host polymer and its cleavage energy ( $\Delta G_P$ ), or the interfacial forces ( $\Delta G_{MP}$ ). Dispersion in polymer matrices is achieved for lowest  $\Delta G$ . (b) The cleavage energy of montmorillonite (CEC = 91 meq/100 g) modified with alkylammonium surfactants of different chain length and head groups exhibits maxima and minima depending on completion of alkyl monolayers and bilayers (indicated by numbers). Residual strong Coulomb forces upon cleavage of quaternary ammonium surfactants at short chain length are found due to incomplete partition of the charged head groups between the two layers until a thickness of a partial bilayer is reached. Reproduced with permission from ref. 88.

chains undergo order–disorder transitions as a function of temperature that have been extensively studied by differential scanning calorimetry, IR spectroscopy, SFG, NMR spectroscopy, sum-frequency generation, and computer simulation. Significant thermal transitions occur at intermediate packing density  $\lambda_0$  between 0.20 and 0.75, whereby up to two reversible transitions have been identified (Fig. 41).<sup>18</sup> These transitions correspond to the partial melting of the alkyl backbones, given a sufficient chain length  $> \sim C_{10}$ , as well as to lateral rearrangements of the head groups on the clay mineral surface that are often not immediately reversible upon cooling.<sup>341,343</sup> The second type of transition is common for quaternary ammonium head groups that have a lower barrier for rearrangement on the surface, whereas primary ammonium head groups do not exhibit the second type of thermal transition due to additional hydrogen bonds with the surface.<sup>68,88,344,345</sup>

The alkyl chains confined between such mineral layers are in a quasi-liquid state.<sup>68,345</sup> The variety of conformations

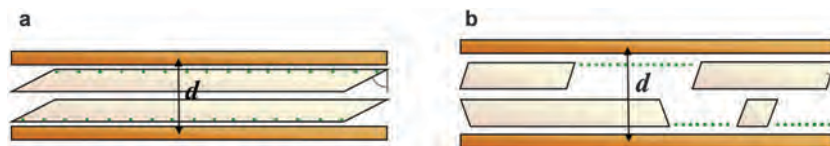


Fig. 39 Schematic of clay mineral layers (brown) containing mixtures of superficial alkali cations (green dots) and alkylammonium surfactants (tilted light brown areas). Partial ion exchange may lead to either (a) homogeneous structures containing surfactants and remaining alkali cations or (b) phase segregated structures containing islands of surfactants and portions of non-exchanged cations. Adapted from ref. 18 and 332.

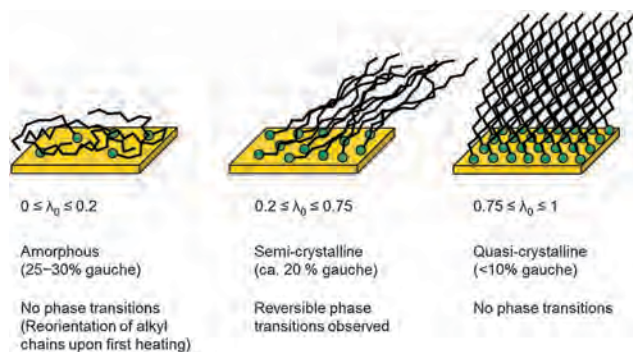


Fig. 40 Structure of homogeneous alkyl monolayers (chain length  $\geq C_{10}$ ) on flat substrates as a function of the packing density  $\lambda_0$ . Significant reversible thermal transitions are found at packing densities between 0.20 and 0.75. Reproduced with permission from ref. 137.

between solid-like with less gauche conformations and liquid-like with more gauche conformations could be observed in molecular models as a function of chain length and packing in the interlayer space. On substrates with low cation exchange capacity (CEC) and single-arm surfactants, the packing density is 0.1 to 0.2 and the backbones are oriented near-parallel to the surface (Fig. 40 and 42). The degree of conformational disorder is high and no reversible melting transitions are observed. On substrates with higher CEC, or in the presence of multi-arm surfactants, *e.g.* trioctadecylmethylammonium ions, the packing density is higher (*e.g.* 0.4) and the alkyl chains assume a regular tilt angle relative to the surface. In these systems, reversible melting transitions occur (Fig. 41a). For very high packing density  $> 0.75$ , quasi-crystalline order leads to over 90% anti conformations and allows no reversible melting transitions (Fig. 40). High packing densities over 0.80 are also found for thiol surfactants on Ag, Au, and Cu.<sup>137</sup> The case of low packing density leads to significant variation in interlayer packing. As the chain length of the surfactants increases, flat-on monolayers, bilayers, and multilayers are formed, as represented by stepwise increases in basal plane spacing as observed in X-ray diffraction (Fig. 42).

The successive filling of organic layers leads to maxima and minima in interlayer density as well as in the cohesive energy between the layers (Fig. 38). The fluctuations in interlayer density cause changes in the cleavage energy between 45 and 30  $\text{mJ m}^{-2}$ , in the percentage of gauche conformations between 30% and 15%, and in the interlayer density between 800 and 600  $\text{kg m}^{-3}$ .<sup>88</sup> The variation of cleavage energies is particularly interesting as a contribution to barriers for exfoliation of layered silicates in polymer and solvent matrices. The organic material

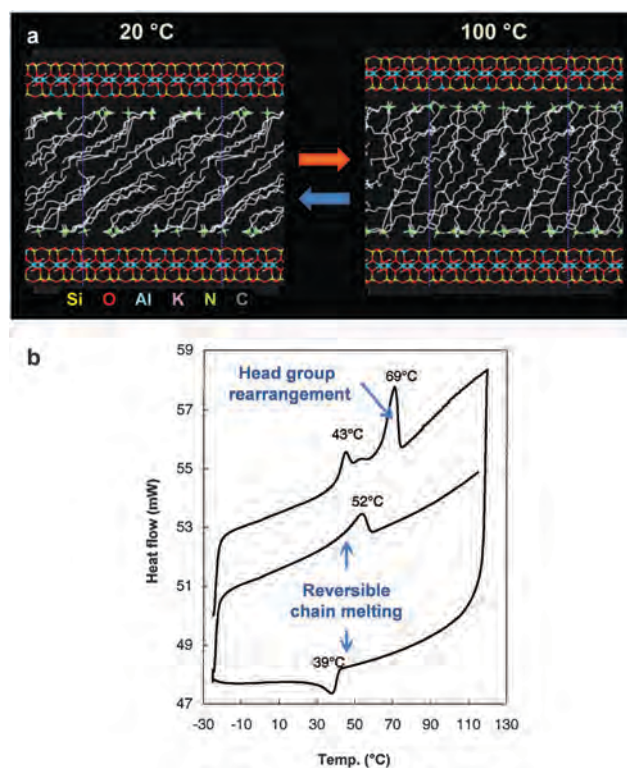


Fig. 41 Reversible thermal transitions according to simulation and differential scanning calorimetry (DSC). The packing density  $\lambda_0$  is 0.40. (a) A transition of semi-ordered octadecyltrimethylammonium chains to random orientation on mica upon heating in molecular dynamics simulation. Order-disorder transitions of the backbone as well as lateral rearrangements of the quaternary ammonium head groups occur. (b) DSC data indicate two corresponding transitions, of which the rearrangement of head groups is not immediately reversible. Reproduced with permission from ref. 18 and 341.

acts as a separator of interlayer Coulomb attraction that amounts to several hundred  $\text{mJ m}^{-2}$  if not mitigated by organic surfactants. Some Coulomb attraction remains at monolayer thickness depending on the choice of the head group (Fig. 38b). For monolayer and bilayer coverage, the alternation in cleavage energies between high and low values can be seen. Interlayer properties such as gallery spacing, interlayer density, the percentage of anti and gauche conformations, associated changes in vibration spectra, as well as cleavage energies can be computed in near-quantitative agreement with measurements. The current upper size limit to monitor the motion of atoms in predictive quality using classical molecular dynamics simulation is between 10 and 100 nm.

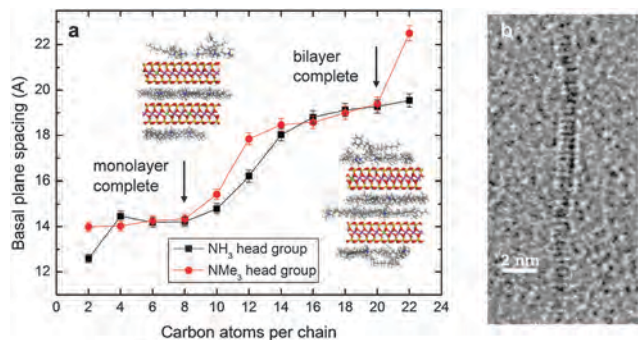


Fig. 42 Gallery spacing and visualization of alkylammonium montmorillonites as a function of chain length. (a) Basal plane spacing of alkyl ammonium chains grafted to montmorillonite of low CEC (91 meq/100 g) as a function of head group and chain length at stoichiometric ion exchange. The successive formation of monolayers and bilayers is shown using atomistic models, and the computed basal plane spacing agrees better than 5% with X-ray data. (b) TEM micrograph of an organically modified montmorillonite lamella embedded in an epoxy polymer matrix (upright orientation). The visualization of the layered silicate is possible similar to the simulation, however, the location of surfactant chains or of polymer cannot be traced. Reproduced with permission from ref. 345 and 346.

## 5.2. Cement minerals and concrete

Cement minerals share some of the properties of clay minerals although they are typically exposed to hydration reactions and exhibit many possible nano and micromorphologies that contribute to the stability and durability of building structures.<sup>327,347,348</sup>

Important cement minerals include tricalcium silicate, dicalcium silicate, tricalcium aluminate, gypsum, ettringite, double layer hydroxides (LDH) such as monosulfate (hydrocalumite), other Afm phases, tobermorites 9, 11, and 14 Å that may represent hydrated phases, as well as calcium silicate hydrate (CSH) gel with various calcium-to-silica-to-water (C/S/H) ratios.<sup>326,349</sup> The quantitative simulation of structural and surface properties of these phases is feasible with the PCFF-INTERFACE force field, including quantitative insight into aqueous properties and polymer-stabilized phases.<sup>11</sup> These recent tools can answer open questions in the understanding of the interfaces, reactions, and structure formation on the nanometer scale, helping to overcome limitations in experimental techniques.<sup>327,349–353</sup> In combination with quantum and continuum methods, multi-scale simulations are expected to play a significant role in gaining further fundamental understanding of grinding and hydration processes in cement due to growing pressure to reduce the global CO<sub>2</sub> footprint upon cement production, to increase the lifetime of building structures, and rationalize the setting properties of alternative cement formulations.<sup>351</sup>

An example for a strongly ionic and reactive surface is that of tricalcium silicate, Ca<sub>3</sub>SiO<sub>5</sub>, the main component of Portland cement (also called C<sub>3</sub>S). The mineral is composed of individual silicate tetrahedra, calcium ions, and oxide ions. The anisotropy of the arrangement of ions is comparatively low and cleavage energies of various crystal planes are similar (Fig. 43).<sup>80</sup> Cohesion is caused to over 95% by internal Coulomb interactions and is very strong; the cleavage energy of 1340 mJ m<sup>-2</sup> is comparable to precious metals (Table 1). Unhydrated portions of cement particles

consist mainly of C<sub>3</sub>S and the strength of C<sub>3</sub>S, including a bulk modulus of 105 GPa, contributes to the mechanical stability of concrete. It is hereby notable that tricalcium silicate is nevertheless only partially ionic and partially a covalent compound, as the atomic charges are *ca.* +1.0e for Si, -1.0e for silicate oxygen, +1.5e for calcium ions and -1.5e for oxide ions, respectively (see Section 2). The balance between covalent and ionic bonding is also innately connected to the reactivity of the surfaces with water. In the first step of the hydration reaction, oxide ions are instantly hydrated to hydroxide ions, and silicate tetrahedra experience hydration to superficial silanol groups. The process of subsequent deposition of calcium hydroxide and dissolution of individual silicate species leads to condensation and formation of oligomeric silicates (C-S-H gels).<sup>327</sup> Ongoing investigations by spectroscopy, imaging, and simulation aim at better understanding of such nanoscale processes to control the complex interactions between multiple inorganic and added organic phases, both thermodynamically and kinetically.

The cation density on the surface and interactions with organic molecules can be conveniently analyzed using models

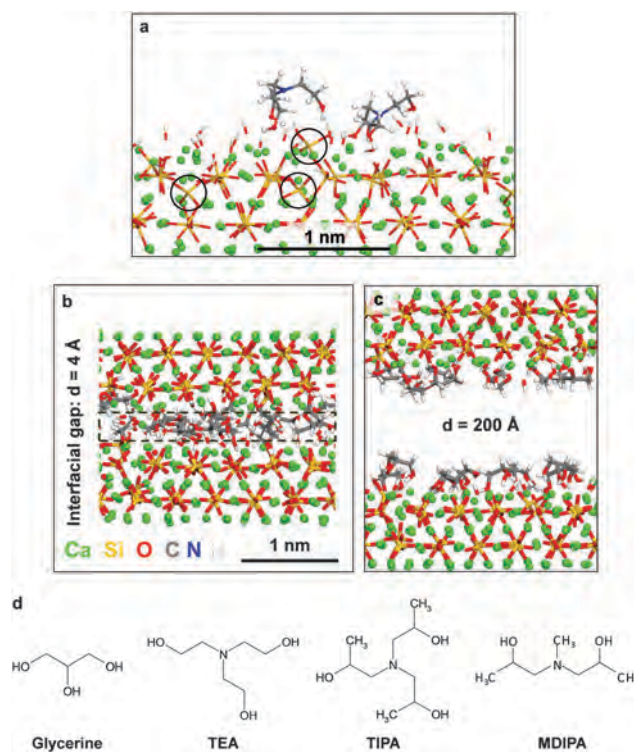


Fig. 43 The surface of tricalcium silicate, Ca<sub>3</sub>SiO<sub>5</sub>, and its interaction with organic alcohols used as grinding aids. (a) Adsorption on the representative (040) surface involves complexation of Ca<sup>2+</sup> ions and hydrogen bonds between hydroxyl groups of the alcohols with hydroxide and silicate groups on the mineral surface (shown for TEA at 383 K). Some disorder of the superficial silicate tetrahedra can be seen. (b and c) Origin of the reduction of agglomeration forces by multiple molecules above monolayer coverage in the agglomerated and separated state (shown for glycerine). The agglomeration energy corresponds to the difference in energy between state (c) and (b). (d) Common alcohols and amines used as grinding aids in cement production. Reproduced with permission from ref. 80.

and molecular dynamics simulation (Fig. 43). Alcohols and amines of low molecular weight such as glycerine and triethanolamine are commonly used to prevent agglomeration of cement particles upon grinding to achieve energy savings in a ball mill (Fig. 43d). Computer simulations helped explain the effect of such modifiers in molecular detail.<sup>80</sup> The analysis of adsorption energies on representative low energy (040) surfaces showed that adsorption can be rather strong on initially hydrated as well as on non-hydrated surfaces, on the order of  $-20$  to  $-50$  kcal mol<sup>-1</sup>. The origin of adhesion are the complexation of superficial Ca ions by hydroxyl groups in the alcohols as well as hydrogen bonds between superficial hydroxide groups of C<sub>3</sub>S and amine or hydroxyl groups of the alcohols (Fig. 43a). The area density of calcium ions on the surface is very high, including 3.2Ca<sup>2+</sup> per nm<sup>2</sup> on the immediate outer surface layer and 2.6Ca<sup>2+</sup> per nm<sup>2</sup> in the upper plane of silicon atoms, totaling 5.8Ca<sup>2+</sup> ions per nm<sup>2</sup>. Due to the high charge of calcium and the high area density on the surface, the cations do not easily dissolve or swell. However, they induce very strong adsorption. At the same time, an organic layer of more than monolayer thickness reduces the strong Coulomb forces between cleaved surfaces very effectively (Fig. 43b and c). The adsorbed molecules thus function as a spacer, and the agglomeration energy can be computed as the energy difference between the separated (Fig. 43c) and unified surfaces (Fig. 43b) in equilibrium. It was also found that the effectiveness as a spacer, which reduces the agglomeration energy between cleaved mineral surfaces, does not correlate with the trend in adsorption strength. Flexible, surface adaptive, and strongly adsorbing molecules such as glycerine do not effectively keep the surface apart; rather some alkyl groups are required to act as a potent spacer and grinding aid. The reduction in agglomeration energy can be quantified in first approximation by assuming idealized even surfaces, and the computed trend among a number of candidate molecules agrees with observations in energy savings in the ball mill (Fig. 44).<sup>80</sup> Just one monolayer of organic molecules of about 0.5 nm thickness reduces the agglomeration energy over 95% compared to the original cleavage energy of 1340 mJ m<sup>-2</sup>, and by about 80% compared to the agglomeration energy of 250 mJ m<sup>-2</sup> of initially hydrated tricalcium silicate surfaces. The high efficiency is due to the spacer effect and the minimization of local dipole moments by molecule-specific complexation of surface ions.

## 6. Challenges and opportunities

The diverse examples illustrate a range of systems where computational insight into inorganic-biological and inorganic-organic interfaces contributes to better understanding of binding mechanisms, nanostructure growth, chemical reactions, and other property predictions to help improve devices and other products. Major challenges associated with the mentioned simulation methods are (1) the interpretation of computational results in the context of a broad spectrum of length and time scales, (2) the need for reliable and perhaps electronic-structure enhanced force fields for a broader range of compounds, (3) the question

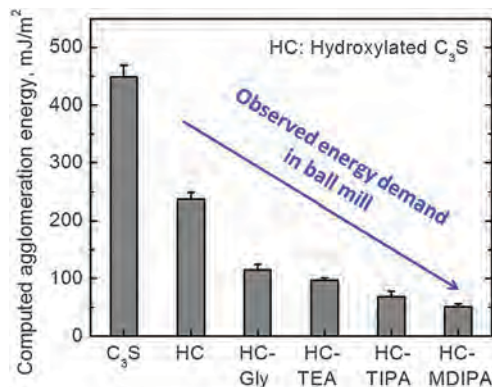


Fig. 44 Computed agglomeration energy of C<sub>3</sub>S, initially hydrated C<sub>3</sub>S, and organically modified surfaces slightly below monolayer coverage in the separated state (0.20 mg m<sup>-2</sup>). The trend correlates with the observed energy demand in ball mills. Reproduced with permission from ref. 80.

to which extent chemical knowledge and automation shall be used to derive new parameters, as well as (4) the choice of problems for computer simulations of societal relevance where the broader impacts are high.

A common challenge is often how to interpret the simulation data, for example at a length scale of 10 nm and a time scale of 100 ns, in the context of a device or a product that is macroscopic, performs over the duration of seconds, and involves nanoscale self-assembly as well as electrical conductivity. In a biosensor, as an example, the function of the device is inherently multi-scale, and pertinent information can be obtained from a range of experimental measurements, DFT calculations, MD calculations, and coarse-grain/continuum models. Complex problems such as this are common, and it is then important to break down and relate the overall performance to sub-problems that can be answered using individual experimental and computational techniques for relevant time and length scales (Fig. 1). The most effective combination of approaches, such as the translation of atomistic information into coarse-grain models and *vice versa*, to obtain comprehensive predictions, can be a determinant for the level of success *versus* failure.

Another challenge is the development of validated force fields for a broader range of compounds, especially for inorganic compounds, and eventually the inclusion of electronic structure features such as the arrangement of  $\pi$  electrons in graphitic materials, d electrons in transition metals, *etc.*<sup>71</sup> The procedure for such developments, where the Hamiltonian reproduces structures and energies, has been laid out (Fig. 3). Some classes of promising compounds that may benefit from further parameter developments include graphitic materials, organic (polymeric) semiconductors, quantum dots, layered materials such as (Mo,W)(S,Se)<sub>2</sub>, metals of different crystal structure, alloys, oxides, and mixed oxides. Ultimately, it would be desirable to cover most (or all) compounds across the periodic table in high accuracy in a uniform simulation platform. A continuing challenge is that breaking or forming covalent bonds in simulations require adjustments in bond connectivity, reactive force fields, local QM calculations, or QM/MM approaches.<sup>50,354-358</sup>

Such development efforts also raise the question to which extent chemical knowledge and understanding of the models should be the basis of force field development, or automated fitting approaches should be employed.<sup>73,76,77,359</sup> Opinions are divided on this point, nevertheless, experience shows that force fields and models based on chemical knowledge and careful interpretation of all parameters outperform automated assignments by a margin. It is helpful to recall that models are always a copy of the real thing, *i.e.*, they will never be as good as real. Therefore, a choice needs to be made between the best attempt involving current chemical knowledge and interpretation, or to leave the parameter derivation to fitting algorithms which by themselves may involve additional assumptions and not match up in validity. The benefit of automated parameters derivation is access to a broader range of compounds and the commercial potential of broadly usable simulation platforms. In this regard, automation can be very beneficial to the scientific community provided procedures are simple and sensibly chosen. On the other hand, careful compound-per-compound chemical analysis, including analogy considerations to similar compounds and parameter validation against experiments, appear to be necessary at least for key compounds to provide supportive benchmarks for automated approaches. The INTERFACE force field, or similar approaches that take into account chemical knowledge and understanding, send a clear message that force fields based on this approach can outperform DFT methods in (non-electronic) properties. Then, the accuracy of classical force fields exceeds that of quantum methods at a million times lower computational cost.

A major challenge is also the choice of problems for simulations. While simulations tend to be less involved than experiments, a certain entrance barrier is present, especially if model development and validation efforts must precede actual mechanistic analyses and property predictions in comparison to measurements. It is therefore advisable to choose modeling problems carefully with respect to anticipated impacts, specific societal or corporate product needs, and feasibility to solve the stated problem. The choice of computational methods can also be guided by the type of experimental data that is available or anticipated to become available for comparison and verification of predictions.

## 7. Conclusion

In conclusion, methods for the simulation of inorganic–organic interfaces and applications to materials design have been reviewed. The emphasis was placed on the 1 to 100 nm scale, classical atomistic methods, and a feedback loop between refined understanding of chemical bonding, translation into accurate force fields, chemically realistic simulations, and interpretation of the computational results in the context of experimental characterization and performance measurements. Specifically, surface properties of metallic and nonmetallic solids at the nanometer scale and governing principles of the selective adsorption of molecules, surfactants, and biopolymers were explained and illustrated by examples. Clear distinctions

emerge between precious metal surfaces, polar pH responsive surfaces such as silica, and densely ionic mineral surfaces such as calcium apatites. Whereas precious metal surfaces are rather simple chemically and exhibit strong attraction, many polar surfaces are prone to protonation/deprotonation equilibria and surface reactivity. The differences in surface chemistry determine available options to control the assembly of surfactants, polymers, and biomacromolecules, and to grow defined nanomaterials from available precursors. A wide variety of chemically different surfaces may often be encountered that originate from the ‘same’ principal material such as silica, apatite, or calcium carbonate. We explained, from the perspective of accurate atomistic models, simulation, and from available experimental results, the mechanisms of selective binding of ligands and polymers to these different materials classes as they are currently known. Applications to estimate binding affinities to nanoparticles, to understand crystal growth, to design catalysts, and to predict agglomeration forces have been shown. The examples also demonstrate that the accuracy of force fields, supported by the interpretation of the parameters and comparison with experiment, can exceed that of density functionals at a fraction of the computational cost.

The different types of substrates possess unique surface characteristics. High surface energy on metal surfaces leads to soft epitaxial adsorption and associated growth preferences. Cation dissociation and hydrogen bonding on silica surfaces depends strongly on pH and leads to binding of highly different peptide sequences. A fixed area density of cations on clay minerals, which results from defect substitution sites, allows grafting of surfactants layers with controllable definition by ion exchange. Strongly ionic surfaces on apatites and tricalcium silicate are subject to protonation reactions with water, which regulates ion dissociation and binding of organic molecules and polymers. Essentially, the individual surface chemistry determines the interactions with solvents, polymers, and biological molecules so that it appears difficult to formulate universal rules for the design of binding biopolymers that apply to all materials types.

Simulations can provide quantitative trends in interactions and help design binding molecules for each class of materials, allowing the formulation of materials-specific concepts with predictive character. These concepts are (1) epitaxial matching of molecules to given metal surfaces (under consideration of the role of induced charges if applicable), (2) the determination of the area density of dissociable ions on silica, apatite, and clay mineral surfaces as a function of pH to anticipate the role of ion pairing and cation exchange *versus* hydrogen bonds and hydrophobic effects, (3) consideration of protonation states on pH responsive surfaces such as apatite and calcite, *e.g.*, based on *pK* values, to control specific adsorption of charged molecules, (4) elucidation of the packing density and prediction of tilt angles and thermal behavior of surfactant chains on substrates where grafting can be controlled, and (5) specific consideration of surface reactions on nanocatalysts, especially rate-determining steps, based on chemical knowledge/first principles calculation and including the impact of interfacial assembly on reaction kinetics.

Application of such concepts can provide guidance even without numerical simulations, and semi-quantitative or quantitative predictions are feasible using the simulation techniques described. Laboratory synthesis and characterization is ultimately required to test properties of new materials, empirically found or aided by simulation. The feedback loop with computation accelerates traditional trial-and error approaches in materials discovery and performance enhancement.

## Acknowledgements

The authors acknowledge support from the National Science Foundation (DMR-0955071, DMR-1437355, CBET-1530790), AFOSR (FA9550-14-1-0194), ONR-MURI (N00014-14-1-0675), ACS-PRF (54135-ND10), Procter and Gamble, UES, Inc., AFRL, the Ohio Supercomputing Center, Research Computing at the University of Colorado-Boulder, the Biofrontiers Compute Cluster at CU, and the University of Colorado-Boulder.

## References

- C. Sanchez, P. Belleville, M. Popall and L. Nicole, *Chem. Soc. Rev.*, 2011, **40**, 696–753.
- M. Osada and T. Sasaki, *Adv. Mater.*, 2012, **24**, 210–228.
- K. L. Scrivener and A. Nonat, *Cem. Concr. Res.*, 2011, **41**, 651–665.
- A. Hagfeldt, G. Boschloo, L. C. Sun, L. Kloo and H. Pettersson, *Chem. Rev.*, 2010, **110**, 6595–6663.
- L. A. Utracki, M. Seppehr and E. Boccaleri, *Polym. Adv. Technol.*, 2007, **18**, 1–37.
- S. V. Dorozhkin, *Acta Biomater.*, 2010, **6**, 715–734.
- S. A. Mackowiak, A. Schmidt, V. Weiss, C. Argyo, C. von Schirnding, T. Bein and C. Bräuchle, *Nano Lett.*, 2013, **13**, 2576–2583.
- C. Tamerler and M. Sarikaya, *Acta Biomater.*, 2007, **3**, 289–299.
- R. J. Macfarlane, B. Lee, M. R. Jones, N. Harris, G. C. Schatz and C. A. Mirkin, *Science*, 2011, **334**, 204–208.
- J. H. Harding, D. M. Duffy, M. L. Sushko, P. M. Rodger, D. Quigley and J. A. Elliott, *Chem. Rev.*, 2008, **108**, 4823–4854.
- H. Heinz, T.-J. Lin, R. K. Mishra and F. S. Emami, *Langmuir*, 2013, **29**, 1754–1765.
- J. Kirkpatrick, V. Marcon, J. Nelson, K. Kremer and D. Andrienko, *Phys. Rev. Lett.*, 2007, **98**, 227402.
- M. Praprotnik, L. D. Site and K. Kremer, *Annu. Rev. Phys. Chem.*, 2008, **59**, 545–571.
- M. Huang, T. A. Pascal, H. Kim, W. A. Goddard III and J. R. Greer, *Nano Lett.*, 2011, **11**, 1241–1246.
- T. P. J. Knowles and M. J. Buehler, *Nat. Nanotechnol.*, 2011, **6**, 469–479.
- W. F. van Gunsteren, D. Bakowies, R. Baron, I. Chandrasekhar, M. Christen, X. Daura, P. Gee, D. P. Geerke, A. Glattli, P. H. Hunenberger, M. A. Kastenholz, C. Oostenbrink, M. Schenk, D. Trzesniak, N. F. van der Vegt and H. B. Yu, *Angew. Chem., Int. Ed.*, 2006, **45**, 4064–4092.
- B. J. Teppen, K. Rasmussen, P. M. Bertsch, D. M. Miller and L. Schafer, *J. Phys. Chem. B*, 1997, **101**, 1579–1587.
- H. Heinz, H. J. Castelijns and U. W. Suter, *J. Am. Chem. Soc.*, 2003, **125**, 9500–9510.
- H. Heinz and U. W. Suter, *J. Phys. Chem. B*, 2004, **108**, 18341–18352.
- A. G. Kalinichev and R. J. Kirkpatrick, *Chem. Mater.*, 2002, **14**, 3539–3549.
- F. Iori, R. Di Felice, E. Molinari and S. Corni, *J. Comput. Chem.*, 2009, **30**, 1465–1476.
- G. K. Lockwood and S. H. Garofalini, *J. Chem. Phys.*, 2009, **131**, 074703.
- J. R. Hill and J. Sauer, *J. Phys. Chem.*, 1995, **99**, 9536–9550.
- P. W. Atkins and R. S. Friedman, *Molecular Quantum Mechanics*, Oxford University Press, Oxford, 3rd edn, 1997.
- D. A. McQuarrie and J. D. Simon, *Physical Chemistry – A Molecular Approach*, University Science Books, Sausalito, CA, 1997.
- Springer Handbook of Atomic, Molecular, and Optical Physics*, Springer, New York, 2006.
- Y. Zhao and D. G. Truhlar, *Acc. Chem. Res.*, 2008, **41**, 157–167.
- J. VandeVondele, M. Krack, F. Mohamed, M. Parrinello, T. Chassaing and J. Hutter, *Comput. Phys. Commun.*, 2005, **167**, 103–128.
- R. Valero, J. R. Gomes, D. G. Truhlar and F. Illas, *J. Chem. Phys.*, 2010, **132**, 104701.
- D. Jacquemin, E. A. Perpete, I. Ciofini, C. Adamo, R. Valero, Y. Zhao and D. G. Truhlar, *J. Chem. Theory Comput.*, 2010, **6**, 2071–2085.
- P. R. K. Westmoreland, P. A. Kollman, A. M. Chaka, P. T. Cummings, K. Morokuma, M. Neurock, E. B. Stechel and P. Vashishta, *Applying Molecular and Materials Modeling: An International Comparative Study*, Kluwer Academic, Amsterdam, 2002.
- A. Calzolari, G. Cicero, C. Cavazzoni, R. Di Felice, A. Catellani and S. Corni, *J. Am. Chem. Soc.*, 2010, **132**, 4790–4795.
- N. E. Singh-Miller and N. Marzari, *Phys. Rev. B: Condens. Matter Mater. Phys.*, 2009, **80**, 235407.
- D. A. Bardwell, C. S. Adjiman, Y. A. Arnautova, E. Bartashevich, S. X. M. Boerrigter, D. E. Braun, A. J. Cruz-Cabeza, G. M. Day, R. G. Della Valle, G. R. Desiraju, B. P. van Eijck, J. C. Facelli, M. B. Ferraro, D. Grillo, M. Habgood, D. W. M. Hofmann, F. Hofmann, K. V. J. Jose, P. G. Karamertzanis, A. V. Kazantsev, J. Kendrick, L. N. Kuleshova, F. J. J. Leusen, A. V. Maleev, A. J. Misquitta, S. Mohamed, R. J. Needs, M. A. Neumann, D. Nikylov, A. M. Orendt, R. Pal, C. C. Pantelides, C. J. Pickard, L. S. Price, S. L. Price, H. A. Scheraga, J. van de Streek, T. S. Thakur, S. Tiwari, E. Venuti and I. K. Zhitkov, *Acta Crystallogr., Sect. B: Struct. Sci.*, 2011, **67**, 535–551.
- S. L. Price, *Acc. Chem. Res.*, 2009, **42**, 117–126.
- S. V. Patwardhan, F. S. Emami, R. J. Berry, S. E. Jones, R. R. Naik, O. Deschaume, H. Heinz and C. C. Perry, *J. Am. Chem. Soc.*, 2012, **134**, 6244–6256.
- J. Feng, J. M. Slocik, M. Sarikaya, R. R. Naik, B. L. Farmer and H. Heinz, *Small*, 2012, **8**, 1049–1059.
- S. Corni, M. Hnilova, C. Tamerler and M. Sarikaya, *J. Phys. Chem. C*, 2013, **117**, 16990–17003.

- 39 L. B. Wright and T. R. Walsh, *Phys. Chem. Chem. Phys.*, 2013, **15**, 4715–4726.
- 40 C. L. Freeman, J. H. Harding, D. J. Cooke, J. A. Elliott, J. S. Lardge and D. M. Duffy, *J. Phys. Chem. C*, 2007, **111**, 11943–11951.
- 41 Q. Hu, M. H. Nielsen, C. L. Freeman, L. M. Hamm, J. Tao, J. R. I. Lee, T. Y. J. Han, U. Becker, J. H. Harding, P. M. Dove and J. J. De Yoreo, *Faraday Discuss.*, 2012, **159**, 509–523.
- 42 K. Lindorff-Larsen, S. Piana, R. O. Dror and D. E. Shaw, *Science*, 2011, **334**, 517–520.
- 43 H. Ramezani-Dakhel, L. Y. Ruan, Y. Huang and H. Heinz, *Adv. Funct. Mater.*, 2015, **25**, 1374–1384.
- 44 H. Heinz, R. A. Vaia, H. Koerner and B. L. Farmer, *Chem. Mater.*, 2008, **20**, 6444–6456.
- 45 J. Schneider and L. C. Ciacchi, *J. Am. Chem. Soc.*, 2012, **134**, 2407–2413.
- 46 G. D. Zartman, H. Liu, B. Akdim, R. Pachter and H. Heinz, *J. Phys. Chem. C*, 2010, **114**, 1763–1772.
- 47 Y. Yang, Q. Cui and N. Sahai, *Langmuir*, 2010, **26**, 9848–9859.
- 48 A. D. MacKerell, M. Feig and C. L. Brooks, *J. Comput. Chem.*, 2004, **25**, 1400–1415.
- 49 P. Virnau, M. Muller, L. G. MacDowell and K. Binder, *J. Chem. Phys.*, 2004, **121**, 2169–2179.
- 50 K. Chenoweth, A. C. T. van Duin and W. A. Goddard, *J. Phys. Chem. A*, 2008, **112**, 1040–1053.
- 51 D. W. Brenner, O. A. Shenderova, J. A. Harrison, S. J. Stuart, B. Ni and S. B. Sinnott, *J. Phys.: Condens. Matter*, 2002, **14**, 783–802.
- 52 T. Liang, T. R. Shan, Y. T. Cheng, B. D. Devine, M. Noordhoek, Y. Z. Li, Z. Z. Lu, S. R. Phillpot and S. B. Sinnott, *Mater. Sci. Eng., R*, 2013, **74**, 255–279.
- 53 J. C. Moller, S. A. Barr, E. J. Schultz, T. D. Breitzman and R. J. Berry, *JOM*, 2013, **65**, 147–167.
- 54 S. K. Nath, F. A. Escobedo and J. J. de Pablo, *J. Chem. Phys.*, 1998, **108**, 9905–9911.
- 55 V. A. Harmandaris, N. P. Adhikari, N. F. A. van der Vegt and K. Kremer, *Macromolecules*, 2006, **39**, 6708–6719.
- 56 S. O. Nielsen, C. F. Lopez, G. Srinivas and M. L. Klein, *J. Chem. Phys.*, 2003, **119**, 7043.
- 57 L. Monticelli, S. K. Kandasamy, X. Periole, R. G. Larson, D. P. Tieleman and S.-J. Marrink, *J. Chem. Theory Comput.*, 2008, **4**, 819–834.
- 58 H. Heinz, B. L. Farmer, R. B. Pandey, J. M. Slocik, S. S. Patnaik, R. Pachter and R. R. Naik, *J. Am. Chem. Soc.*, 2009, **131**, 9704–9714.
- 59 B. Hess, S. Leon, N. van der Vegt and K. Kremer, *Soft Matter*, 2006, **2**, 409–414.
- 60 C. Forrey and M. Muthukumar, *Biophys. J.*, 2006, **91**, 25–41.
- 61 C. T. Wong and M. Muthukumar, *J. Chem. Phys.*, 2010, **133**, 045101.
- 62 T. A. Knotts, N. Rathore, D. C. Schwartz and J. J. de Pablo, *J. Chem. Phys.*, 2007, **126**, 084901.
- 63 R. A. Riggelman, K. S. Schweizer and J. J. de Pablo, *Macromolecules*, 2008, **41**, 4969–4977.
- 64 F. A. Detcheverry, G. L. Liu, P. F. Nealey and J. J. de Pablo, *Macromolecules*, 2010, **43**, 3446–3454.
- 65 J. Feng, K. A. Cavicchi and H. Heinz, *ACS Nano*, 2011, **5**, 9413–9420.
- 66 R. D. Groot and P. B. Warren, *J. Chem. Phys.*, 1997, **107**, 4423–4435.
- 67 J. Fraaije, B. A. C. vanVlimmeren, N. M. Maurits, M. Postma, O. A. Evers, C. Hoffmann, P. Altevogt and G. GoldbeckWood, *J. Chem. Phys.*, 1997, **106**, 4260–4269.
- 68 H. Heinz, H. Koerner, K. L. Anderson, R. A. Vaia and B. L. Farmer, *Chem. Mater.*, 2005, **17**, 5658–5669.
- 69 H. Heinz, R. A. Vaia, B. L. Farmer and R. R. Naik, *J. Phys. Chem. C*, 2008, **112**, 17281–17290.
- 70 M. W. Mahoney and W. L. Jorgensen, *J. Chem. Phys.*, 2000, **112**, 8910–8922.
- 71 R. Xu, C.-C. Chen, L. Wu, M. C. Scott, W. Theis, C. Ophus, M. Bartels, Y. Yang, H. Ramezani-Dakhel, M. R. Sawaya, H. Heinz, L. D. Marks, P. Ercius and J. Miao, *Nat. Mater.*, 2015, **14**, 1099–1103.
- 72 P. Dauber-Osguthorpe, V. A. Roberts, D. J. Osguthorpe, J. Wolff, M. Genest and A. T. Hagler, *Proteins: Struct., Funct., Genet.*, 1988, **4**, 31–47.
- 73 A. D. MacKerell Jr., D. Bashford, M. Bellott, R. L. Dunbrack Jr., J. D. Evanseck, M. J. Fields, S. Fischer, J. Gao, H. Guo, S. Ha, D. Joseph-McCarthy, L. Kuchnir, K. Kuczera, F. T. K. Lau, C. Mattos, S. Michnick, T. Ngo, D. T. Nguyen, B. Prodhom, W. E. Reiher III, B. Roux, M. Schlenkrich, J. C. Smith, R. Stote, J. Straub, D. Watanabe, J. Wiórkiewicz-Kuczera, D. Yin and M. Karplus, *J. Phys. Chem. B*, 1998, **102**, 3586–3616.
- 74 W. L. Jorgensen, D. S. Maxwell and J. TiradoRives, *J. Am. Chem. Soc.*, 1996, **118**, 11225–11236.
- 75 D. A. Pearlman, D. A. Case, J. W. Caldwell, W. S. Ross, T. E. Cheatham, S. Debolt, D. Ferguson, G. Seibel and P. Kollman, *Comput. Phys. Commun.*, 1995, **91**, 1–41.
- 76 H. Sun, S. J. Mumby, J. R. Maple and A. T. Hagler, *J. Am. Chem. Soc.*, 1994, **116**, 2978–2987.
- 77 H. Sun, *J. Phys. Chem. B*, 1998, **102**, 7338–7364.
- 78 F. S. Emami, V. Puddu, R. J. Berry, V. Varshney, S. V. Patwardhan, C. C. Perry and H. Heinz, *Chem. Mater.*, 2014, **26**, 2647–2658.
- 79 R. K. Mishra, L. Fernández-Carrasco, R. J. Flatt and H. Heinz, *Dalton Trans.*, 2014, **43**, 10602–10616.
- 80 R. K. Mishra, R. J. Flatt and H. Heinz, *J. Phys. Chem. C*, 2013, **117**, 10417–10432.
- 81 N. M. Bedford, H. Ramezani-Dakhel, J. M. Slocik, B. D. Briggs, Y. Ren, A. I. Frenkel, V. Petkov, H. Heinz, R. R. Naik and M. R. Knecht, *ACS Nano*, 2015, **9**, 5082–5092.
- 82 F. S. Emami, V. Puddu, R. J. Berry, V. Varshney, S. V. Patwardhan, C. C. Perry and H. Heinz, *Chem. Mater.*, 2014, **26**, 5725–5734.
- 83 J. Feng, R. B. Pandey, R. J. Berry, B. L. Farmer, R. R. Naik and H. Heinz, *Soft Matter*, 2011, **7**, 2113–2120.
- 84 H. Heinz, R. A. Vaia and B. L. Farmer, *J. Chem. Phys.*, 2006, **124**, 224713.
- 85 L. Ruan, H. Ramezani-Dakhel, C.-Y. Chiu, E. Zhu, Y. Li, H. Heinz and Y. Huang, *Nano Lett.*, 2013, **13**, 840–846.
- 86 S. K. Meena and M. Sulpizi, *Langmuir*, 2013, **29**, 14954–14961.

- 87 H. Heinz, K. C. Jha, J. Luettmer-Strathmann, B. L. Farmer and R. R. Naik, *J. R. Soc., Interface*, 2011, **8**, 220–232.
- 88 Y. T. Fu and H. Heinz, *Chem. Mater.*, 2010, **22**, 1595–1605.
- 89 J. R. Hill and J. Sauer, *J. Phys. Chem.*, 1994, **98**, 1238–1244.
- 90 R. T. Cygan, J.-J. Liang and A. G. Kalinichev, *J. Phys. Chem. B*, 2004, **108**, 1255–1266.
- 91 T. K. Kundu, K. Hanumantha Rao and S. C. Parker, *J. Phys. Chem. B*, 2005, **109**, 11286–11295.
- 92 C. M. Fang, S. C. Parker and G. de With, *J. Am. Ceram. Soc.*, 2000, **83**, 2082–2084.
- 93 E. R. Cruz-Chu, A. Aksimentiev and K. Schulten, *J. Phys. Chem. B*, 2006, **110**, 21497–21508.
- 94 P. E. M. Lopes, V. Murashov, M. Tazi, E. Demchuk and A. D. MacKerell, *J. Phys. Chem. B*, 2006, **110**, 2782–2792.
- 95 L. Delle Site, C. Abrams, A. Alavi and K. Kremer, *Phys. Rev. Lett.*, 2002, **89**, 156103.
- 96 P. Schravendijk, N. van der Vegt, L. Delle Site and K. Kremer, *ChemPhysChem*, 2005, **6**, 1866–1871.
- 97 L. B. Wright, P. M. Rodger, T. R. Walsh and S. Corni, *J. Phys. Chem. C*, 2013, **117**, 24292–24306.
- 98 L. L. Atanasoska, J. C. Buchholz and G. A. Somorjai, *Surf. Sci.*, 1978, **72**, 189–207.
- 99 L. E. Firment and G. A. Somorjai, *J. Chem. Phys.*, 1977, **66**, 2901–2913.
- 100 G. A. Somorjai and Y. M. Li, *Proc. Natl. Acad. Sci. U. S. A.*, 2011, **108**, 917–924.
- 101 L. B. Wright, P. M. Rodger, S. Corni and T. R. Walsh, *J. Chem. Theory Comput.*, 2013, **9**, 1616–1630.
- 102 K. Makrodimitris, D. L. Masica, E. T. Kim and J. J. Gray, *J. Am. Chem. Soc.*, 2007, **129**, 13713–13722.
- 103 Y.-C. Chien, D. L. Masica, J. J. Gray, S. Nguyen, H. Vali and M. D. McKee, *J. Biol. Chem.*, 2009, **284**, 23491–23501.
- 104 S. B. Schrier, M. K. Sayeg and J. J. Gray, *Langmuir*, 2011, **27**, 11520–11527.
- 105 A. Leaver-Fay, M. Tyka, S. M. Lewis, O. F. Lange, J. Thompson, R. Jacak, K. Kaufman, P. D. Renfrew, C. A. Smith, W. Sheffler, I. W. Davis, S. Cooper, A. Treuille, D. J. Mandell, F. Richter, Y.-E. A. Ban, S. J. Fleishman, J. E. Corn, D. E. Kim, S. Lyskov, M. Berrondo, S. Mentzer, Z. Popovic, J. J. Havranek, J. Karanicolas, R. Das, J. Meiler, T. Kortemme, J. J. Gray, B. Kuhlman, D. Baker and P. Bradley, in *Methods in Enzymology, Vol 487: Computer Methods, Pt C*, ed. M. L. Johnson and L. Brand, 2011, pp. 545–574.
- 106 M. S. Pacella, D. C. E. Koo, R. A. Thottungal and J. J. Gray, in *Research Methods in Biomineralization Science*, ed. J. J. D. Yoreo, 2013, vol. 532, pp. 343–366.
- 107 S. H. Sun, C. B. Murray, D. Weller, L. Folks and A. Moser, *Science*, 2000, **287**, 1989–1992.
- 108 R. R. Naik, S. E. Jones, C. J. Murray, J. C. McAuliffe, R. A. Vaia and M. O. Stone, *Adv. Funct. Mater.*, 2004, **14**, 25–30.
- 109 C. Y. Chiu, Y. J. Li, L. Y. Ruan, X. C. Ye, C. B. Murray and Y. Huang, *Nat. Chem.*, 2011, **3**, 393–399.
- 110 L. Y. Ruan, H. Ramezani-Dakheel, C. Lee, Y. J. Li, X. F. Duan, H. Heinz and Y. Huang, *ACS Nano*, 2014, **8**, 6934–6944.
- 111 R. Coppage, J. M. Slocik, B. D. Briggs, A. I. Frenkel, H. Heinz, R. R. Naik and M. R. Knecht, *J. Am. Chem. Soc.*, 2011, **133**, 12346–12349.
- 112 N. Kröger, S. Lorenz, E. Brunner and M. Sumper, *Science*, 2002, **298**, 584–586.
- 113 V. Puddu and C. C. Perry, *Langmuir*, 2014, **30**, 227–233.
- 114 S. V. Patwardhan, S. J. Clarson and C. C. Perry, *Chem. Commun.*, 2005, 1113–1121.
- 115 M. B. Dickerson, S. E. Jones, Y. Cai, G. Ahmad, R. R. Naik, N. Kroeger and K. H. Sandhage, *Chem. Mater.*, 2008, **20**, 1578–1584.
- 116 W. R. Tyson and W. A. Miller, *Surf. Sci.*, 1977, **62**, 267–276.
- 117 S. M. Wiederhorn, R. L. Moses and B. L. Bean, *J. Am. Ceram. Soc.*, 1970, **53**, 18–23.
- 118 S. Ramaseshan, *Proc. Indiana Acad. Sci.*, 1946, **24**, 114–121.
- 119 G. Vigil, Z. H. Xu, S. Steinberg and J. Israelachvili, *J. Colloid Interface Sci.*, 1994, **165**, 367–385.
- 120 L. T. Zhuravlev, *Colloids Surf., A*, 1993, **74**, 71–90.
- 121 M. Lewin, A. Mey-Marom and R. Frank, *Polym. Adv. Technol.*, 2005, **16**, 429–441.
- 122 S. Brunauer, D. L. Kantro and C. H. Weise, *Can. J. Chem.*, 1956, **34**, 729–742.
- 123 S. Wu, in *Polymer Handbook*, ed. J. Brandrup and E. H. Immergut, Wiley & Sons, New York, 3rd edn, 1989, pp. 521–541.
- 124 M. S. Daw, S. M. Foiles and M. I. Baskes, *Mater. Sci. Rep.*, 1993, **9**, 251–310.
- 125 *CRC Handbook of Chemistry and Physics*, CRC Press, Boca Raton, FL, 89th edn, 2008.
- 126 M. J. Sanders, M. Leslie and C. R. A. Catlow, *J. Chem. Soc., Chem. Commun.*, 1984, 1271–1273.
- 127 B. W. H. van Beest and G. J. Kramer, *Phys. Rev. Lett.*, 1990, **64**, 1955–1958.
- 128 M. I. Haftel, N. Bernstein, M. J. Mehl and D. A. Papaconstantopoulos, *Phys. Rev. B: Condens. Matter Mater. Phys.*, 2004, **70**, 125419.
- 129 A. S. Barnard and M. Sternberg, *J. Mater. Chem.*, 2007, **17**, 4811–4819.
- 130 V. N. Mochalin, O. Shenderova, D. Ho and Y. Gogotsi, *Nat. Nanotechnol.*, 2012, **7**, 11–23.
- 131 L. Y. Ruan, C. Y. Chiu, Y. J. Li and Y. Huang, *Nano Lett.*, 2011, **11**, 3040–3046.
- 132 J. M. Slocik, M. O. Stone and R. R. Naik, *Small*, 2005, **1**, 1048–1052.
- 133 C. C. Lee, J. A. MacKay, J. M. J. Frechet and F. C. Szoka, *Nat. Biotechnol.*, 2005, **23**, 1517–1526.
- 134 Z. Liu, J. Z. Liu, Y. Cheng, Z. Li, L. Wang and Q. Zheng, *Phys. Rev. B: Condens. Matter Mater. Phys.*, 2012, **85**, 205418.
- 135 C. J. Shih, M. S. Strano and D. Blankschtein, *Nat. Mater.*, 2013, **12**, 866–869.
- 136 L. H. Dubois, B. R. Zegarski and R. G. Nuzzo, *J. Am. Chem. Soc.*, 1990, **112**, 570–579.
- 137 H. Heinz, R. A. Vaia and B. L. Farmer, *Langmuir*, 2008, **24**, 3727–3733.
- 138 M. A. Van Hove, R. J. Koestner, P. C. Stair, J. P. Biberian, L. L. Kesmodel, I. Bartos and G. A. Somorjai, *Surf. Sci.*, 1981, **103**, 189–217.

- 139 M. A. Van Hove, R. J. Koestner, P. C. Stair, J. P. Biberian, L. L. Kesmodel, I. Bartos and G. A. Somorjai, *Surf. Sci.*, 1981, **103**, 218–238.
- 140 H. Ramezani-Dakhel, P. A. Mirau, R. R. Naik, M. R. Knecht and H. Heinz, *Phys. Chem. Chem. Phys.*, 2013, **15**, 5488–5492.
- 141 Y. Xia, Y. Xiong, B. Lim and S. E. Skrabalak, *Angew. Chem., Int. Ed.*, 2009, **48**, 60–103.
- 142 Y. Xiong, J. M. McLellan, Y. Yin and Y. Xia, *Angew. Chem., Int. Ed.*, 2007, **46**, 790–794.
- 143 H. Witte and E. Wölfel, *Rev. Mod. Phys.*, 1958, **30**, 51–55.
- 144 K. P. Aref'ev and S. A. Vorob'ev, *Izv. Vuz. Fiz.*, 1972, **15**, 34–38.
- 145 N. Thong and D. Schwarzenbach, *Acta Crystallogr., Sect. A: Cryst. Phys., Diffr., Theor. Gen. Crystallogr.*, 1979, **35**, 658–664.
- 146 J. Lewis, D. Schwarzenbach and H. D. Flack, *Acta Crystallogr., Sect. A: Cryst. Phys., Diffr., Theor. Gen. Crystallogr.*, 1982, **38**, 733–739.
- 147 E. L. Belokoneva, Y. K. Gubina, J. B. Forsyth and P. J. Brown, *Phys. Chem. Miner.*, 2002, **29**, 430–438.
- 148 H. Heinz, *J. Phys.: Condens. Matter*, 2014, **26**, 244105.
- 149 S. Y. Sheu, D. Y. Yang, H. L. Selzle and E. W. Schlag, *Proc. Natl. Acad. Sci. U. S. A.*, 2003, **100**, 12683–12687.
- 150 T. A. Halgren, *J. Am. Chem. Soc.*, 1992, **114**, 7827–7843.
- 151 D. A. Giljohann, D. S. Seferos, W. L. Daniel, M. D. Massich, P. C. Patel and C. A. Mirkin, *Angew. Chem., Int. Ed.*, 2010, **49**, 3280–3294.
- 152 E. Auyeung, T. Li, A. J. Senesi, A. L. Schmucker, B. C. Pals, M. O. de la Cruz and C. A. Mirkin, *Nature*, 2014, **505**, 73–77.
- 153 N. L. Rosi, D. A. Giljohann, C. S. Thaxton, A. K. Lytton-Jean, M. S. Han and C. A. Mirkin, *Science*, 2006, **312**, 1027–1030.
- 154 J. M. Slocik, J. S. Zabinski, D. M. Phillips and R. R. Naik, *Small*, 2008, **4**, 548–551.
- 155 A. Abbas, A. Brimer, J. M. Slocik, L. M. Tian, R. R. Naik and S. Singamaneni, *Anal. Chem.*, 2013, **85**, 3977–3983.
- 156 Y. Xia, P. D. Yang, Y. G. Sun, Y. Y. Wu, B. Mayers, B. Gates, Y. D. Yin, F. Kim and Y. Q. Yan, *Adv. Mater.*, 2003, **15**, 353–389.
- 157 R. Coppage, J. M. Slocik, H. Ramezani-Dakhel, N. M. Bedford, H. Heinz, R. R. Naik and M. R. Knecht, *J. Am. Chem. Soc.*, 2013, **135**, 11048–11054.
- 158 O. Cohavi, S. Corni, F. De Rienzo, R. Di Felice, K. E. Gottschalk, M. Hoefling, D. Kokh, E. Molinari, G. Schreiber, A. Vaskevich and R. C. Wade, *J. Mol. Recognit.*, 2010, **23**, 259–262.
- 159 M. Hoefling, F. Iori, S. Corni and K. E. Gottschalk, *Langmuir*, 2010, **26**, 8347–8351.
- 160 R. B. Pandey, H. Heinz, J. Feng, B. L. Farmer, J. M. Slocik, L. F. Drummy and R. R. Naik, *Phys. Chem. Chem. Phys.*, 2009, **11**, 1989–2001.
- 161 S. H. D. Lacerda, J. J. Park, C. Meuse, D. Pristiniski, M. L. Becker, A. Karim and J. F. Douglas, *ACS Nano*, 2010, **4**, 365–379.
- 162 J. M. Slocik and R. R. Naik, *Adv. Mater.*, 2006, **18**, 1988–1992.
- 163 M. Hnilova, E. E. Oren, U. O. Seker, B. R. Wilson, S. Collino, J. S. Evans, C. Tamerler and M. Sarikaya, *Langmuir*, 2008, **24**, 12440–12445.
- 164 K. C. Jha, H. Liu, M. R. Bockstaller and H. Heinz, *J. Phys. Chem. C*, 2013, **117**, 25969–25981.
- 165 W. Jiang, B. Y. Kim, J. T. Rutka and W. C. Chan, *Nat. Nanotechnol.*, 2008, **3**, 145–150.
- 166 M. Sarikaya, C. Tamerler, A. K. Y. Jen, K. Schulten and F. Baneux, *Nat. Mater.*, 2003, **2**, 577–585.
- 167 X. Fu, Y. Wang, L. Huang, Y. Sha, L. Gui, L. Lai and Y. Tang, *Adv. Mater.*, 2003, **15**, 902–906.
- 168 J. M. Slocik and D. W. Wright, *Biomacromolecules*, 2003, **4**, 1135–1141.
- 169 Y. Shao, Y. Jin and S. Dong, *Chem. Commun.*, 2004, 1104–1105.
- 170 M. Sethi and M. R. Knecht, *Langmuir*, 2010, **26**, 9860–9874.
- 171 F. Iori and S. Corni, *J. Comput. Chem.*, 2008, **29**, 1656–1666.
- 172 G. Cicero, A. Calzolari, S. Corni and A. Catellani, *J. Phys. Chem. Lett.*, 2011, **2**, 2582–2586.
- 173 F. Iori, S. Corni and R. Di Felice, *J. Phys. Chem. C*, 2008, **112**, 13540–13545.
- 174 M. Rosa, S. Corni and R. Di Felice, *J. Phys. Chem. C*, 2012, **116**, 21366–21373.
- 175 G. Y. Hong, H. Heinz, R. R. Naik, B. L. Farmer and R. Pachter, *ACS Appl. Mater. Interfaces*, 2009, **1**, 388–392.
- 176 L. M. Ghiringhelli and L. Delle Site, *J. Am. Chem. Soc.*, 2008, **130**, 2634–2638.
- 177 S. K. Ramakrishnan, M. Martin, T. Cloitre, L. Firlej and C. Gergely, *J. Chem. Inf. Model.*, 2014, **54**, 2117–2126.
- 178 S. M. Tomasio and T. R. Walsh, *J. Phys. Chem. C*, 2009, **113**, 8778–8785.
- 179 S. N. Kim, Z. Kuang, J. M. Slocik, S. E. Jones, Y. Cui, B. L. Farmer, M. C. McAlpine and R. R. Naik, *J. Am. Chem. Soc.*, 2011, **133**, 14480–14483.
- 180 Z. X. Yang, Z. G. Wang, X. L. Tian, P. Xiu and R. H. Zhou, *J. Chem. Phys.*, 2012, **136**, 025103.
- 181 C. M. Welch, A. N. Camden, S. A. Barr, G. M. Leuty, G. S. Kedziora and R. J. Berry, *J. Chem. Phys.*, 2015, **143**, 045104.
- 182 S. K. Rhee, *J. Am. Ceram. Soc.*, 1972, **55**, 300–303.
- 183 J. Abrahamson, *Carbon*, 1973, **11**, 337–362.
- 184 R. Zacharia, H. Ulbricht and T. Hertel, *Phys. Rev. B: Condens. Matter Mater. Phys.*, 2004, **69**, 155406.
- 185 S. S. Kim, Z. F. Kuang, Y. H. Ngo, B. L. Farmer and R. R. Naik, *ACS Appl. Mater. Interfaces*, 2015, **7**, 20447–20453.
- 186 C. Tamerler, E. E. Oren, M. Duman, E. Venkatasubramanian and M. Sarikaya, *Langmuir*, 2006, **22**, 7712–7718.
- 187 T. K. Sau and C. J. Murphy, *Langmuir*, 2004, **20**, 6414–6420.
- 188 V. Khare, Z. Li, A. Manton, A. A. Ayi, S. Sonkaria, A. Voelkl, A. F. Thünemann and A. Taubert, *J. Mater. Chem.*, 2010, **20**, 1332–1339.
- 189 H. J. Ryu, L. Sanchez, H. A. Keul, A. Raj and M. R. Bockstaller, *Angew. Chem., Int. Ed.*, 2008, **47**, 7639–7643.
- 190 D. Li, M. H. Nielsen, J. R. I. Lee, C. Frandsen, J. F. Banfield and J. J. De Yoreo, *Science*, 2012, **336**, 1014–1018.
- 191 V. Stamenkovic, B. S. Mun, K. J. J. Mayrhofer, P. N. Ross, N. M. Markovic, J. Rossmeisl, J. Greeley and J. K. Nørskov, *Angew. Chem., Int. Ed.*, 2006, **45**, 2897–2901.
- 192 F. Tournus, K. Sato, T. Epicier, T. J. Konno and V. Dupuis, *Phys. Rev. Lett.*, 2013, **110**, 055501.
- 193 S. Siahrostami, A. Verdager-Casadevall, M. Karamad, D. Deiana, P. Malacrida, B. Wickman, M. Escudero-Escribano, E. A. Paoli, R. Frydendal, T. W. Hansen, I. Chorkendorff, I. E. L. Stephens and J. Rossmeisl, *Nat. Mater.*, 2013, **12**, 1137–1143.

- 194 D. L. Wang, H. L. L. Xin, R. Hovden, H. S. Wang, Y. C. Yu, D. A. Muller, F. J. DiSalvo and H. D. Abruna, *Nat. Mater.*, 2013, **12**, 81–87.
- 195 D. B. Pacardo, M. Sethi, S. E. Jones, R. R. Naik and M. R. Knecht, *ACS Nano*, 2009, **3**, 1288–1296.
- 196 B. Goris, S. Bals, W. Van den Broek, E. Carbo-Argibay, S. Gomez-Grana, L. M. Liz-Marzan and G. Van Tendeloo, *Nat. Mater.*, 2012, **11**, 930–935.
- 197 C. C. Chen, C. Zhu, E. R. White, C. Y. Chiu, M. C. Scott, B. C. Regan, L. D. Marks, Y. Huang and J. W. Miao, *Nature*, 2013, **496**, 74–77.
- 198 M. C. Scott, C. C. Chen, M. Mecklenburg, C. Zhu, R. Xu, P. Ercius, U. Dahmen, B. C. Regan and J. W. Miao, *Nature*, 2012, **483**, 444–447.
- 199 C. L. Farrow, P. Juhas, J. W. Liu, D. Bryndin, E. S. Bozin, J. Bloch, T. Proffen and S. J. L. Billinge, *J. Phys.: Condens. Matter*, 2007, **19**, 335219.
- 200 N. T. S. Phan, M. Van Der Sluys and C. W. Jones, *Adv. Synth. Catal.*, 2006, **348**, 609–679.
- 201 J. K. Stille, *Angew. Chem., Int. Ed.*, 1986, **25**, 508–523.
- 202 B. Briggs, N. Bedford, S. Seifert, H. Koerner, H. Ramezani-Dakheel, H. Heinz, R. R. Naik, A. Frenkel and M. R. Knecht, *Chem. Sci.*, 2015, **6**, 6413–6419.
- 203 L. Xue and Z. Lin, *Chem. Soc. Rev.*, 2010, **39**, 1692–1705.
- 204 D. B. Pacardo and M. R. Knecht, *Catal. Sci. Technol.*, 2013, **3**, 745–753.
- 205 Z. F. Kuang, S. N. Kim, W. J. Crookes-Goodson, B. L. Farmer and R. R. Naik, *ACS Nano*, 2010, **4**, 452–458.
- 206 T. Kuila, S. Bose, P. Khanra, A. K. Mishra, N. H. Kim and J. H. Lee, *Biosens. Bioelectron.*, 2011, **26**, 4637–4648.
- 207 B. Akdim, R. Pachter, S. S. Kim, R. R. Naik, T. R. Walsh, S. Trohalaki, G. Hong, Z. Kuang and B. L. Farmer, *ACS Appl. Mater. Interfaces*, 2013, **5**, 7470–7477.
- 208 J. N. Anker, W. P. Hall, O. Lyandres, N. C. Shah, J. Zhao and R. P. Van Duyne, *Nat. Mater.*, 2008, **7**, 442–453.
- 209 C. Walkey, E. A. Sykes and W. C. W. Chan, *Am. Soc. Hematol. Education Program Book*, 2009, **2009**, 701–707.
- 210 E. C. Dreaden, A. M. Alkilany, X. Huang, C. J. Murphy and M. A. El-Sayed, *Chem. Soc. Rev.*, 2012, **41**, 2740–2779.
- 211 P. K. Jain, X. Huang, I. H. El-Sayed and M. A. El-Sayed, *Acc. Chem. Res.*, 2008, **41**, 1578–1586.
- 212 X. Jiang, B. Tian, J. Xiang, F. Qian, G. Zheng, H. Wang, L. Mai and C. M. Lieber, *Proc. Natl. Acad. Sci. U. S. A.*, 2011, **108**, 12212–12216.
- 213 H. A. Lowenstam and S. Weiner, *On Biomineralization*, Oxford University Press, New York, 1989.
- 214 S. Mann, *Biomineralization Principles and Concepts in Bioinorganic Materials Chemistry*, Oxford University Press, New York, 2001.
- 215 L. M. Gordon and D. Joester, *Nature*, 2011, **469**, 194–197.
- 216 M. Hildebrand, *Chem. Rev.*, 2008, **108**, 4855–4874.
- 217 C. C. Perry, S. V. Patwardhan and O. Deschaume, *Biochem. Soc. Trans.*, 2009, **37**, 687–691.
- 218 J. P. Simmer and A. G. Fincham, *Crit. Rev. Oral Biol. Med.*, 1995, **6**, 84–108.
- 219 C. Sanchez, B. Julian, P. Belleville and M. Popall, *J. Mater. Chem.*, 2005, **15**, 3559–3592.
- 220 K. Ariga, A. Vinu, Y. Yamauchi, Q. Ji and J. P. Hill, *Bull. Chem. Soc. Jpn.*, 2012, **85**, 1–32.
- 221 M. W. Ambrogio, C. R. Thomas, Y. L. Zhao, J. I. Zink and J. F. Stoddart, *Acc. Chem. Res.*, 2011, **44**, 903–913.
- 222 Y. Deng, Y. Cai, Z. Sun, J. Liu, C. Liu, J. Wei, W. Li, C. Liu, Y. Wang and D. Zhao, *J. Am. Chem. Soc.*, 2010, **132**, 8466–8473.
- 223 S. H. Joo, J. Y. Park, C.-K. Tsung, Y. Yamada, P. Yang and G. A. Somorjai, *Nat. Mater.*, 2009, **8**, 126–131.
- 224 R. G. Chaudhuri and S. Paria, *Chem. Rev.*, 2012, **112**, 2373–2433.
- 225 J.-R. Li, R. J. Kuppler and H.-C. Zhou, *Chem. Soc. Rev.*, 2009, **38**, 1477–1504.
- 226 A. Markovic, D. Stoltenberg, D. Enke, E. U. Schlunder and A. Seidel-Morgenstern, *J. Membr. Sci.*, 2009, **336**, 17–31.
- 227 D. K. Chattopadhyay and D. C. Webster, *Prog. Polym. Sci.*, 2009, **34**, 1068–1133.
- 228 D. R. Paul and L. M. Robeson, *Polymer*, 2008, **49**, 3187–3204.
- 229 N. Jouault, P. Vallat, F. Dalmas, S. Said, J. Jestin and F. Boue, *Macromolecules*, 2009, **42**, 2031–2040.
- 230 E. S. Thian, T. Konishi, Y. Kawanobe, P. N. Lim, C. Choong, B. Ho and M. Aizawa, *J. Mater. Sci.: Mater. Med.*, 2013, **24**, 437–445.
- 231 S. V. Dorozhkin, *Am. J. Biomed. Eng.*, 2012, **2**, 48–97.
- 232 M. C. Weiger, J. J. Park, M. D. Roy, C. M. Stafford, A. Karim and M. L. Becker, *Biomaterials*, 2010, **31**, 2955–2963.
- 233 F. Nudelman, K. Pieterse, A. George, P. H. H. Bomans, H. Friedrich, L. J. Brylka, P. A. J. Hilbers, G. de With and N. Sommerdijk, *Nat. Mater.*, 2010, **9**, 1004–1009.
- 234 A. Dey, P. H. H. Bomans, F. A. Muller, J. Will, P. M. Frederik, G. de With and N. Sommerdijk, *Nat. Mater.*, 2010, **9**, 1010–1014.
- 235 S. Bertazzo, W. F. Zambuzzi, D. D. P. Campos, T. L. Ogeda, C. V. Ferreira and C. A. Bertran, *Colloids Surf., B*, 2010, **78**, 177–184.
- 236 P. J. M. Smeets, K. R. Cho, R. G. E. Kempen, N. Sommerdijk and J. J. De Yoreo, *Nat. Mater.*, 2015, **14**, 394–399.
- 237 J. W. Shen, C. L. Li, N. F. A. van der Vegt and C. Peter, *J. Phys. Chem. C*, 2013, **117**, 6904–6913.
- 238 D. Quigley, P. M. Rodger, C. L. Freeman, J. H. Harding and D. M. Duffy, *J. Chem. Phys.*, 2009, **131**, 094703.
- 239 S. Elhadji, J. J. De Yoreo, J. R. Hoyer and P. M. Dove, *Proc. Natl. Acad. Sci. U. S. A.*, 2006, **103**, 19237–19242.
- 240 G. Fu, S. R. Qiu, C. A. Orme, D. E. Morse and J. J. De Yoreo, *Adv. Mater.*, 2005, **17**, 2678–2683.
- 241 S. W. Lee, C. B. Mao, C. E. Flynn and A. M. Belcher, *Science*, 2002, **296**, 892–895.
- 242 H. Liu, M. Espe, D. A. Modarelli, E. Arias, I. Moggio, R. F. Ziolo and H. Heinz, *J. Mater. Chem. A*, 2014, **2**, 8705–8711.
- 243 X.-Y. Yu, B.-X. Lei, D.-B. Kuang and C.-Y. Su, *Chem. Sci.*, 2011, **2**, 1396–1400.
- 244 H. Lee, H. C. Leventis, S.-J. Moon, P. Chen, S. Ito, S. A. Haque, T. Torres, F. Nueesch, T. Geiger, S. M. Zakeeruddin, M. Graetzel and M. K. Nazeeruddin, *Adv. Funct. Mater.*, 2009, **19**, 2735–2742.
- 245 Y. Yin and A. P. Alivisatos, *Nature*, 2005, **437**, 664–670.

- 246 E. E. Oren, R. Notman, I. W. Kim, E. J. Spencer, T. R. Walsh, R. Samudrala, C. Tamerler and M. Sarikaya, *Langmuir*, 2010, **26**, 11003–11009.
- 247 R. K. Iler, *The Chemistry of Silica: Solubility, Polymerization, Colloid and Surface Properties, and Biochemistry*, John Wiley & Sons, New York, 1979.
- 248 V. Puddu and C. C. Perry, *ACS Nano*, 2012, **6**, 6356–6363.
- 249 S. K. Milonjić, *Colloids Surf.*, 1987, **23**, 301–312.
- 250 T. F. Tadros and J. Lyklema, *J. Electroanal. Chem. Interfacial Electrochem.*, 1968, **17**, 267–275.
- 251 D. E. Yates and T. W. Healy, *J. Colloid Interface Sci.*, 1976, **55**, 9–19.
- 252 G. H. Bolt, *J. Phys. Chem.*, 1957, **61**, 1166–1169.
- 253 M. D. Piane, M. Corno and P. Ugliengo, *J. Chem. Theory Comput.*, 2013, **9**, 2404–2415.
- 254 P. Ugliengo, M. Sodupe, F. Musso, I. J. Bush, R. Orlando and R. Dovesi, *Adv. Mater.*, 2008, **20**, 4579–4583.
- 255 A. Pedone, G. Malavasi, M. C. Menziani, U. Segre, F. Musso, M. Corno, B. Civalleri and P. Ugliengo, *Chem. Mater.*, 2008, **20**, 2522–2531.
- 256 T. P. M. Goumans, A. Wander, W. A. Brown and C. R. A. Catlow, *Phys. Chem. Chem. Phys.*, 2007, **9**, 2146–2152.
- 257 G. L. Gambino, G. M. Lombardo, A. Grassi and G. Marletta, *J. Phys. Chem. B*, 2004, **108**, 2600–2607.
- 258 J. Du and A. N. Cormack, *J. Am. Ceram. Soc.*, 2005, **88**, 2532–2539.
- 259 E. Flikkema and S. T. Bromley, *Chem. Phys. Lett.*, 2003, **378**, 622–629.
- 260 B. P. Feuston and S. H. Garofalini, *J. Chem. Phys.*, 1988, **89**, 5818–5824.
- 261 S. H. Garofalini, *J. Chem. Phys.*, 1982, **76**, 3189–3192.
- 262 A. Méndez, E. Bosch, M. Rosés and U. D. Neue, *J. Chromatogr. A*, 2003, **986**, 33–44.
- 263 T. H. Muster, C. A. Prestidge and R. A. Hayes, *Colloids Surf., A*, 2001, **176**, 253–266.
- 264 L. T. Zhuravlev, *Colloids Surf., A*, 2000, **173**, 1–38.
- 265 W. A. House and D. R. Orr, *J. Chem. Soc., Faraday Trans.*, 1992, **88**, 233–241.
- 266 R. Zerrouk, A. Foissy, R. Mercier, Y. Chevallier and J.-C. Morawski, *J. Colloid Interface Sci.*, 1990, **139**, 20–29.
- 267 R. P. Abendroth, *J. Colloid Interface Sci.*, 1970, **34**, 591–596.
- 268 J. A. G. Taylor and J. A. Hockey, *J. Phys. Chem.*, 1966, **70**, 2169–2172.
- 269 M. Corno, M. D. Piane, S. Monti, M. Moreno-Couranjou, P. Choquet and P. Ugliengo, *Langmuir*, 2015, **31**, 6321–6331.
- 270 M. Predota, M. L. Machesky, D. J. Wesolowski and P. T. Cummings, *J. Phys. Chem. C*, 2013, **117**, 22852–22866.
- 271 M. L. Machesky, M. Predota, D. J. Wesolowski, L. Vlcek, P. T. Cummings, J. Rosenqvist, M. K. Ridley, J. D. Kubicki, A. V. Bandura, N. Kumar and J. O. Sofo, *Langmuir*, 2008, **24**, 12331–12339.
- 272 H. Chen, X. Su, K.-G. Neoh and W.-S. Choe, *Langmuir*, 2008, **24**, 6852–6857.
- 273 T. Mori, R. J. Hamers, J. A. Pedersen and Q. Cui, *J. Chem. Theory Comput.*, 2013, **9**, 5059–5069.
- 274 K. I. Sano, H. Sasaki and K. Shiba, *Langmuir*, 2005, **21**, 3090–3095.
- 275 K. I. Sano and K. Shiba, *J. Am. Chem. Soc.*, 2003, **125**, 14234–14235.
- 276 A. George and A. Veis, *Chem. Rev.*, 2008, **108**, 4670–4693.
- 277 T. Z. Lin, *Force Field Parameters and Atomistic Surface Models for Hydroxyapatite and Analysis of Biomolecular Adsorption at Aqueous Interfaces*, PhD thesis, University of Akron, 2013, retrieved from <https://etd.ohiolink.edu>.
- 278 N. H. de Leeuw, *J. Mater. Chem.*, 2010, **20**, 5376–5389.
- 279 M. Corno, A. Rimola, V. Bolis and P. Ugliengo, *Phys. Chem. Chem. Phys.*, 2010, **12**, 6309–6329.
- 280 A. Rimola, M. Aschi, R. Orlando and P. Ugliengo, *J. Am. Chem. Soc.*, 2012, **134**, 10899–10910.
- 281 C. Jäger, T. Welzel, W. Meyer-Zaika and M. Eppele, *Magn. Reson. Chem.*, 2006, **44**, 573–580.
- 282 H. M. Rootare, V. R. Deitz and F. G. Carpenter, *J. Colloid Sci.*, 1962, **17**, 179–206.
- 283 P. W. Brown and R. I. Martin, *J. Phys. Chem. B*, 1999, **103**, 1671–1675.
- 284 S. V. Dorozhkin, *J. Colloid Interface Sci.*, 1997, **191**, 489–497.
- 285 S. V. Dorozhkin, *Comments Inorg. Chem.*, 1999, **20**, 285–299.
- 286 H. Tanaka, M. Chikazawa, K. Kandori and T. Ishikawa, *Phys. Chem. Chem. Phys.*, 2000, **2**, 2647–2650.
- 287 S. S. Barton and B. H. Harrison, *J. Colloid Interface Sci.*, 1976, **55**, 409–414.
- 288 B. Grohe, J. O'Young, D. A. Ionescu, G. Lajoie, K. A. Rogers, M. Karttunen, H. A. Goldberg and G. K. Hunter, *J. Am. Chem. Soc.*, 2007, **129**, 14946–14951.
- 289 D. Spagnoli, D. J. Cooke, S. Kerisit and S. C. Parker, *J. Mater. Chem.*, 2006, **16**, 1997–2006.
- 290 D. J. Cooke and J. A. Elliott, *J. Chem. Phys.*, 2007, **127**, 104706.
- 291 C. L. Freeman, I. Asteriadis, M. Yang and J. H. Harding, *J. Phys. Chem. C*, 2009, **113**, 3666–3673.
- 292 C. L. Freeman, J. H. Harding and D. M. Duffy, *Langmuir*, 2008, **24**, 9607–9615.
- 293 P. Somasundaran and G. E. Agar, *J. Colloid Interface Sci.*, 1967, **24**, 433–440.
- 294 A. M. Bano, P. M. Rodger and D. Quigley, *Langmuir*, 2014, **30**, 7513–7521.
- 295 P. Raiteri, J. D. Gale, D. Quigley and P. M. Rodger, *J. Phys. Chem. C*, 2010, **114**, 5997–6010.
- 296 H. H. Teng, *Science*, 1998, **282**, 724–727.
- 297 S. Weiner and L. Hood, *Science*, 1975, **190**, 987–988.
- 298 A. L. Rachlin, G. S. Henderson and M. C. Goh, *Am. Mineral.*, 1992, **77**, 904–910.
- 299 A. Calzolari, A. Ruini and A. Catellani, *J. Phys. Chem. C*, 2012, **116**, 17158–17163.
- 300 J. Wang, M. Yang, Y. Zhu, L. Wang, A. P. Tomsia and C. Mao, *Adv. Mater.*, 2014, **26**, 4961–4966.
- 301 U. G. K. Wegst, H. Bai, E. Saiz, A. P. Tomsia and R. O. Ritchie, *Nat. Mater.*, 2015, **14**, 23–36.
- 302 G. S. Attard, J. C. Glyde and C. G. Goltner, *Nature*, 1995, **378**, 366–368.
- 303 S. Che, Z. Liu, T. Ohsuna, K. Sakamoto, O. Terasaki and T. Tatsumi, *Nature*, 2004, **429**, 281–284.
- 304 F. Hoffmann, M. Cornelius, J. Morell and M. Froba, *Angew. Chem., Int. Ed.*, 2006, **45**, 3216–3251.

- 305 D. Y. Zhao, J. L. Feng, Q. S. Huo, N. Melosh, G. H. Fredrickson, B. F. Chmelka and G. D. Stucky, *Science*, 1998, **279**, 548–552.
- 306 M. A. Lawson, Z. Xia, B. L. Barnett, J. T. Triffitt, R. J. Phipps, J. E. Dunford, R. M. Locklin, F. H. Ebetino and R. G. G. Russell, *J. Biomed. Mater. Res., Part B*, 2010, **92**, 149–155.
- 307 G. H. Nancollas, R. Tang, R. J. Phipps, Z. Henneman, S. Gulde, W. Wu, A. Mangood, R. G. G. Russell and F. H. Ebetino, *Bone*, 2006, **38**, 617–627.
- 308 R. G. G. Russell, N. B. Watts, F. H. Ebetino and M. J. Rogers, *Osteoporosis Int.*, 2008, **19**, 733–759.
- 309 C. Chen, M. Xia, L. Wu, C. Zhou and F. Wang, *J. Mol. Model.*, 2012, **18**, 4007–4012.
- 310 J. Robinson, I. Cukrowski and H. M. Marques, *THEOCHEM*, 2006, **825**, 134–142.
- 311 C. Aguzzi, P. Cerezo, C. Viseras and C. Caramella, *Appl. Clay Sci.*, 2007, **36**, 22–36.
- 312 S. E. Habas, H. A. S. Platt, M. F. A. M. van Hest and D. S. Ginley, *Chem. Rev.*, 2010, **110**, 6571–6594.
- 313 H. C. Leventis, F. O'Mahony, J. Akhtar, M. Afzaal, P. O'Brien and S. A. Haque, *J. Am. Chem. Soc.*, 2010, **132**, 2743–2750.
- 314 H. Li, P. Winget and J.-L. Brédas, *Chem. Mater.*, 2014, **26**, 631–646.
- 315 Z. Li, X. Zhang and G. Lu, *J. Phys. Chem. C*, 2012, **116**, 9845–9851.
- 316 K. E. Roelofs, T. P. Brennan and S. F. Bent, *J. Phys. Chem. Lett.*, 2014, **5**, 348–360.
- 317 V. Renugopalakrishnan, B. Barbiellini, C. King, M. Molinari, K. Mochalov, A. Sukhanova, I. Nabiev, P. Fojan, H. L. Tuller, M. Chin, P. Somasundaran, E. Padros and S. Ramakrishna, *J. Phys. Chem. C*, 2014, **118**, 16710–16717.
- 318 G. Wu, Z. Li, X. Zhang and G. Lu, *J. Phys. Chem. Lett.*, 2014, **5**, 2649–2656.
- 319 F. Delpech, A. C. Gagneux, C. Nayral, A. Cornejo, Y. Coppel and B. Chaudret, *J. Am. Chem. Soc.*, 2010, **132**, 18147–18157.
- 320 A. V. Akimov, A. J. Neukirch and O. V. Prezhdo, *Chem. Rev.*, 2013, **113**, 4496–4565.
- 321 F. Piersimoni, R. Schlesinger, J. Benduhn, D. Spoltore, S. Reiter, I. Lange, N. Koch, K. Vandewal and D. Neher, *J. Phys. Chem. Lett.*, 2015, **6**, 500–504.
- 322 I.-C. Yeh, J. L. Lenhart and B. C. Rinderspacher, *J. Phys. Chem. C*, 2015, **119**, 7721–7731.
- 323 S. V. Ahir and E. M. Terentjev, *Nat. Mater.*, 2005, **4**, 491–495.
- 324 S. Biswas, Y. Li, M. A. Strosio and M. Dutta, *J. Appl. Phys.*, 2012, **111**, 044303.
- 325 Q. H. Zeng, A. B. Yu and G. Q. Lu, *Prog. Polym. Sci.*, 2008, **33**, 191–269.
- 326 H. F. W. Taylor, *Cement Chemistry*, Academic Press, London, 1997.
- 327 J. W. Bullard, H. M. Jennings, R. A. Livingston, A. Nonat, G. W. Scherer, J. S. Schweitzer, K. L. Scrivener and J. J. Thomas, *Cem. Concr. Res.*, 2011, **41**, 1208–1223.
- 328 B. Kang and G. Ceder, *Nature*, 2009, **458**, 190–193.
- 329 F. Geng, R. Ma, A. Nakamura, K. Akatsuka, Y. Ebina, Y. Yamauchi, N. Miyamoto, Y. Tateyama and T. Sasaki, *Nat. Commun.*, 2013, **4**, 1632.
- 330 R. Z. Ma and T. Sasaki, *Adv. Mater.*, 2010, **22**, 5082–5104.
- 331 H. Heinz, *Clay Miner.*, 2012, **47**, 205–230.
- 332 H. Heinz and U. W. Suter, *Angew. Chem., Int. Ed.*, 2004, **43**, 2239–2243.
- 333 A. Kaushik, R. Kumar, S. K. Arya, M. Nair, B. D. Malhotra and S. Bhansali, *Chem. Rev.*, 2015, **115**, 4571–4606.
- 334 J. L. Suter, D. Groen and P. V. Coveney, *Adv. Mater.*, 2015, **27**, 966–984.
- 335 D. Papkov, Y. Zou, M. N. Andalib, A. Goponenko, S. Z. D. Cheng and Y. A. Dzenis, *ACS Nano*, 2013, **7**, 3324–3331.
- 336 S. Kango, S. Kalia, A. Celli, J. Njuguna, Y. Habibi and R. Kumar, *Prog. Polym. Sci.*, 2013, **38**, 1232–1261.
- 337 R. Dohrmann, D. Genske, O. Karland, S. Kaufhold, L. Kiviranta, S. Olsson, M. Ploetze, T. Sanden, P. Sellin, D. Svensson and M. Valter, *Clays Clay Miner.*, 2012, **60**, 162–175.
- 338 H. C. Greenwell, M. J. Harvey, P. Boulet, A. A. Bowden, P. V. Coveney and A. Whiting, *Macromolecules*, 2005, **38**, 6189–6200.
- 339 R. A. Vaia, R. K. Teukolsky and E. P. Giannelis, *Chem. Mater.*, 1994, **6**, 1017–1022.
- 340 H. Heinz, W. Paul, U. W. Suter and K. Binder, *J. Chem. Phys.*, 2004, **120**, 3847–3854.
- 341 M. A. Osman, G. Seyfang and U. W. Suter, *J. Phys. Chem. B*, 2000, **104**, 4433–4439.
- 342 M. A. Osman, *J. Colloid Interface Sci.*, 1999, **214**, 400–406.
- 343 M. A. Osman, M. Ploetze and P. Skrabal, *J. Phys. Chem. B*, 2004, **108**, 2580–2588.
- 344 Y. T. Fu and H. Heinz, *Philos. Mag.*, 2010, **90**, 2415–2424.
- 345 H. Heinz, R. A. Vaia, R. Krishnamoorti and B. L. Farmer, *Chem. Mater.*, 2007, **19**, 59–68.
- 346 L. F. Drummy, H. Koerner, K. Farmer, A. Tan, B. L. Farmer and R. A. Vaia, *J. Phys. Chem. B*, 2005, **109**, 17868–17878.
- 347 D. L. Kantro, S. Brunauer and C. H. Weise, *J. Colloid Sci.*, 1959, **14**, 363–376.
- 348 A. J. Allen, J. J. Thomas and H. M. Jennings, *Nat. Mater.*, 2007, **6**, 311–316.
- 349 A. Nonat, *Cem. Concr. Res.*, 2004, **34**, 1521–1528.
- 350 H. Minard, S. Garrault, L. Regnaud and A. Nonat, *Cem. Concr. Res.*, 2007, **37**, 1418–1426.
- 351 K. L. Scrivener and A. Nonat, *Cem. Concr. Res.*, 2011, **41**, 651–665.
- 352 H. M. Jennings, *Cem. Concr. Res.*, 2008, **38**, 275–289.
- 353 C. Jolicoeur and M. A. Simard, *Cem. Concr. Compos.*, 1998, **20**, 87–101.
- 354 R. N. Costa Filho, G. Alencar, B. S. Skagerstam and J. S. Andrade, *EPL*, 2013, **101**, 10009.
- 355 P. M. Morse, *Phys. Rev.*, 1929, **34**, 57.
- 356 O. Acevedo and W. L. Jorgensen, *Acc. Chem. Res.*, 2010, **43**, 142–151.
- 357 D. Friebel, V. Viswanathan, D. J. Miller, T. Anniyev, H. Ogasawara, A. H. Larsen, C. P. O'Grady, J. K. Nørskov and A. Nilsson, *J. Am. Chem. Soc.*, 2012, **134**, 9664–9671.
- 358 D. Golze, M. Iannuzzi, N. Manh-Thuong, D. Passerone and J. Hutter, *J. Chem. Theory Comput.*, 2013, **9**, 5086–5097.
- 359 K. Vanommeslaeghe, E. Hatcher, C. Acharya, S. Kundu, S. Zhong, J. Shim, E. Darian, O. Guvench, P. Lopes, I. Vorobyov and A. D. Mackerell, *J. Comput. Chem.*, 2010, **31**, 671–690.